

Reactivity and Interplay of Critical Components in Sodium-Ion Batteries

Zur Erlangung des akademischen Grades einer
DOKTORIN DER NATURWISSENSCHAFTEN

(Dr. rer. nat.)

von der KIT-Fakultät für Chemie und Biowissenschaften

des Karlsruher Instituts für Technologie (KIT)

genehmigte

DISSERTATION

von

M. Sc. Kristina Pfeifer

1. Referent: Prof. Dr. Helmut Ehrenberg

2. Referent: Prof. Dr. Rolf Schuster

Tag der mündlichen Prüfung: 07.12.2020

Selbständigkeitserklärung

Hiermit versichere ich, dass ich die vorliegende Arbeit selbstständig verfasst habe, dass ich keine anderen als die angegebenen Quellen und Hilfsmittel benutzt habe, dass ich die wörtlich oder inhaltlich übernommenen Stellen als solche gekennzeichnet habe und dass ich die Satzung des KIT zur Sicherung guter wissenschaftlicher Praxis in der jeweils gültigen Fassung beachtet habe.

Karlsruhe, den 09.12.2020

Kristina Pfeifer

Danksagung

An dieser Stelle möchte ich all jenen danken, die mich im Laufe der Promotion begleitet und unterstützt haben:

Besonders herzlicher Dank geht zunächst an Professor Dr. Helmut Ehrenberg für die Ermöglichung dieser Arbeit am IAM-ESS und seine stetige Unterstützung. Weiterhin möchte ich Prof. Dr. Rolf Schuster für das Erstellen des Zweitgutachtens dieser Arbeit danken. Zudem danke ich der Deutschen Forschungsgemeinschaft (DFG) für die Finanzierung in Rahmen des POLiS Cluster of Excellence (Projekt-ID 390874152).

Großer Dank geht vor allem an meine Betreuerin Dr. Sonia Dsoke für die Hilfe und alle Anregungen, welche zum Gelingen dieser Arbeit beigetragen haben. Selbstverständlich möchte ich mich auch bei allen bedanken, die mich durch Messungen, Auswertungen und wissenschaftliche Diskussionen im Laufe dieser Arbeit unterstützt haben. Für die Hilfe bei Rietveld-Verfeinerungen geht großer Dank an Dr. Angelina Sarapulova, Chengping Li und Prof. Dr. Helmut Ehrenberg. Für die Charakterisierung der Messproben mit XPS bedanke ich mich herzlich bei Xianlin Luo, Dr. Chittaranjan Das und Dr. Julia Maibach. Weiterer Dank geht an Julian Becherer für die Ausführung der optischen Mikroskopie. Für die Raman, TEM und GSA Messungen bedanke ich mich herzlich bei Öznil Budak und dem Leibniz Institut INM in Saarbrücken und für das Durchführen von ICP-MS Messungen bei Dr. Thomas Bergfeldt und dem IAM-AWP. Ein besonders riesiger Dank geht an meine Studenten Stefanie Arnold, Eugen Zemlyanushin, Jens Anhalt und Daniel Bier für ihren ausgeprägten Fleiß und die stetige Bereitschaft mich experimentell bei dieser Arbeit zu unterstützen.

Außerordentlicher Dank geht auch an Prof. Doron Aurbach und Miryam Greenstein, welche mich herzlich für einen Aufenthalt an ihrem Institut an der Bar-Ilan Universität in Israel aufgenommen haben und mir bei der Erstellung der gemeinsamen Publikation stets zur Seite standen. Zudem danke ich Prof. Magdalena Titirici und Heather Au für die Möglichkeit eines Aufenthalts in ihrer Gruppe am Imperial College in London. Ein großes Dankeschön geht auch an Prof. Dr. Volker Presser für die erfolgreiche Kooperation und die Unterstützung bei der gemeinsamen Publikation.

Für die Hilfe bei allen anfallenden administrativen und organisatorischen Fragen bedanke ich mich sehr bei Almut Kriese.

Für effektive fachliche Diskussionen, persönliche Unterstützung und sehr viel Spaß bedanke ich mich in erster Linie bei Marina Bauer, Chengping Li und Xianlin Luo! Ein großer Dank geht auch an alle Mitglieder des IAM-ESS für eine angenehme Arbeitsatmosphäre, die fachliche Hilfe und

das Einbringen von Ideen. Für eine produktive Atmosphäre, tolle Zusammenarbeit und eine spaßige Zeit im POLiS Projekt bedanke ich mich insbesondere bei meinen Kollegen Tolga Akcay und Marcel Häringer sowie bei Dr. Johannes Schnaidt und Dr. Christian Punckt für die Hilfe bei administrativen und organisatorischen Projektfragen.

Nicht zuletzt geht ein riesiges Dankeschön auch an meine Freunde außerhalb des IAM-ESS für ihre persönliche Unterstützung und Motivation.

Den größten Dank richte ich an meine Eltern, ohne die meine gesamte Ausbildung nicht möglich gewesen wäre und an meine Familie und meinen Freund Dr. Mathias Widmaier. Vielen Dank für euren motivierenden Beistand, dass ihr mir alles zutraut was ich machen möchte und mich dabei immer unterstützt.

Table of contents

Abbreviations	IV
Symbols and constants	VI
Figures	VII
Tables	XI
Zusammenfassung	XIII
Abstract	XIV
1 Introduction	1
2 Theoretical background	5
2.1 Key parameters for batteries	5
2.1.1 Battery potential	5
2.1.2 Battery capacity and rate capability	8
2.1.3 Coulombic efficiency and solid electrolyte interphase	9
2.1.4 Cycling stability	9
2.1.5 Specific energy and specific power	9
2.1.6 Electrochemical signature	10
2.1.7 IR-drop	11
2.2 Sodium-ion-batteries	12
2.2.1 Components and working principle	12
2.2.2 Charge storage mechanisms of active materials in sodium-ion batteries	15
2.2.3 Carbonaceous additives	19
2.2.4 Liquid organic electrolytes	21
3 State-of-the-art literature and classification of this thesis	23
4 Experimental	29
4.1 Preparation of materials and electrolytes	29
4.1.1 Chemicals	29
4.1.2 Synthesis routes	29

4.1.3	Electrolytes.....	30
4.2	Optical methods.....	31
4.2.1	Visual analysis.....	31
4.2.2	Time-resolved light microscopy.....	31
4.3	Electrochemical analysis	32
4.3.1	Electrode preparation	32
4.3.2	Cell preparation	34
4.3.3	Electrochemical characterization	34
4.4	Electrodes and materials characterization techniques	36
4.4.1	X-ray diffraction.....	36
4.4.2	X-ray photoelectron spectroscopy.....	36
4.4.3	Scanning electron microscopy and energy-dispersive spectroscopy	37
4.4.4	Other techniques.....	38
5	The interplay of electrolyte and electrode: reactivity issues and perspectives.....	39
5.1	Sodium reactivity	39
5.1.1	Reactivity of sodium towards organic electrolytes	39
5.1.2	The influence of metallic sodium in electrochemical cells	42
5.1.3	Impact of sodium metal reactivity on the bulk material after electrochemical cycling	45
5.1.4	Surface analysis after electrochemical cycling	46
5.1.5	Conclusive aspects: influence of sodium metal on carbonate-based electrolytes	48
5.2	Perspective approaches for the sodium metal stabilization in organic electrolytes .	49
5.3	Exemplary model – the interaction between electrolytes and Sb ₂ O ₃ -based electrodes in NIBs: uncovering detrimental effects of diglyme.....	51
5.3.1	Sb ₂ O ₃ characterization.....	51
5.3.2	Influence of the electrolyte solution on the electrochemical performance	52
5.3.3	<i>Ex-situ</i> characterization of Sb ₂ O ₃ electrodes.....	55
5.3.4	<i>Ex-situ</i> characterization of the electrolyte and sodium-metal counter electrode..	59

5.3.5	A proposed mechanism that explains the behavior of Sb ₂ O ₃ electrodes cycled in diglyme-based electrolyte solutions.	61
5.3.6	Conclusive aspects: reactivity of the electrolyte solvent	62
6	Antimony-based electrodes: structure, morphology and percolation.....	63
6.1	Normalization: significance for carbon-containing negative electrodes.....	64
6.1.1	Sb synthesis and characterization.....	64
6.1.2	Influence of the carbon amount and normalization.....	65
6.2	Carbon additives: the vital importance for high-performance Sb-based NIBs	67
6.2.1	Properties of the conductive carbon materials	67
6.2.2	Influence of carbon characteristics on Sb/C electrodes.....	71
6.3	Influence of morphology and particle size of Sb on the electrochemical performance	77
6.3.1	Characterization of commercial Sb powder-based samples.....	77
6.3.2	Influence of the Sb particle size on Sb/C electrodes based on commercial antimony powder.....	79
6.4	Conclusive aspects: the interplay of antimony and carbon	83
7	Conclusion.....	84
8	Outlook.....	87
9	References	89
10	Appendix	101
11	Scientific contributions	109
11.1	Publications	109
11.2	Conference contributions	110
12	Contributions of co-authors and other researchers.....	111

Abbreviations

AB	Acetylene Black
AC	Activated Carbon
AM	Active material
Arb.	Arbitrary
At%	Atomic percent
B	Binder
BET	Brunauer-Emmett-Teller
CA	Conductive additive
CCD	Charge-coupled device
CE	Coulombic efficiency
CMC	Carboxymethyl cellulose
CPS	Counts per second
CV	Cyclic voltammetry
DEC	Diethyl carbonate
Diglyme	Diglycol methyl ether/ bis(2-methoxyethyl) ether
DMC	Dimethyl carbonate
DMSO	Dimethyl sulfoxide
EC	Ethylene carbonate
EDS	Energy dispersive X-ray spectroscopy
ESR	Equivalent series resistance
<i>Et al.</i>	<i>et alii / et aliae / et alia</i>
EtOH	Ethanol
FEC	Fluoroethylene carbonate
FWHM	Full-width at half-maximum
GCPL	Galvanostatic cycling with potential limitation
GSA	Gas sorption analysis
ICSD	Inorganic crystal structure database
ICP-MS	Inductively coupled plasma mass spectrometry
LIB	Lithium-ion battery
LTO	Lithium titanate, $\text{Li}_4\text{Ti}_5\text{O}_{12}$
M	Metal
MWCNT	Multi-walled carbon nanotubes

n.a.	Not available
NFMO	Sodium iron manganese oxide, $\text{Na}_{2/3} \text{Fe}_{1/3} \text{Mn}_{2/3} \text{O}_2$
NIB	Sodium-ion battery
OCV	Open-circuit voltage
OLC	Onion-like carbons
PAN	Polyacrylonitrile
PC	Propylene carbonate
PE	Polyethylene
PEEK	Polyether ether ketone
PTFE	Polytetrafluoroethylene
PVdF	Polyvinylidene fluoride
QRE	Quasi-reference electrode
QSDFT	Quenched solid density functional theory
RE	Reference electrode
S	Solvent
SEI	Solid electrolyte interphase
SEM	Scanning electron microscopy
SHE	Standard hydrogen electrode
SSA	Specific surface area
STEM	Scanning transmission electron microscopy
TEM	Transmission electron microscopy
VGCF	Vapor-grown carbon fibers
WE	Working electrode
w/w	Weight by weight
XPS	X-ray photoelectron spectroscopy
XRD	X-ray diffraction

Symbols and constants

$[C]$	C-rate
$c_{ox/red}$	concentration of the oxidized/ reduced species / mol L ⁻¹
E	Electromotive force / V
E^0	Standard electrode potential / V
ε	Specific energy / Wh kg ⁻¹
F	Faraday constant (96485 C mol ⁻¹)
ΔG	Difference of the Gibbs energies / J
ΔG^0	Difference of the Gibbs energies under standard ambient conditions / J
I	Current / A
m	Mass / g
M	Molecular mass / g mol ⁻¹
n	Number of transferred charge carriers
p^0	Standard pressure (100 kPa)
P	Specific power / W kg ⁻¹
φ	Galvani potential / V
$\Delta\varphi_{+/-}$	Galvani potential difference for the positive/ negative electrode / V
$\Delta\Delta\varphi$	Open circuit voltage / V
Q	Electrical charge / mAh
Q_{th}	Theoretical capacity of an active material / mAh g ⁻¹
R	Gas constant (8.314 J mol ⁻¹ K ⁻¹)
R	Ohmic resistance / Ω
R_p	Profile residual (reliability factor)
R_{wp}	Weighted profile residual
t	Time / s
T	Temperature / K or °C
T^0	Standard ambient temperature (298.15 K)
θ	Bragg angle
U	Voltage / V
v	Voltage ramp
z	Valence number

Figures

Figure 1. Schematic three-electrode cell setup.	7
Figure 2. Electrochemical signature of a negative electrode showing a) galvanostatic charge and discharge profiles recorded at constant current and b) cyclic voltammogram collected by applying a constant voltage ramp.	11
Figure 3. Operating principle of a NIB during charging (A) and discharging (B). The electrons “e ⁻ ” and Na-ions movement direction is described by arrows (adapted and modified from Ref. [50]).	12
Figure 4. Different charge storage mechanisms of electrode materials for sodium-ion batteries. Circles are representative of different atoms in a crystal lattice (adapted and modified from Ref. [51]).	15
Figure 5. Chemical structures of depicted electrolyte solvents: a) ethylene carbonate (EC), b) dimethyl carbonate (DMC), c) propylene carbonate (PC), d) fluoroethylene carbonate (FEC), e) bis(2-methoxyethyl) ether (diglyme).	21
Figure 6. a) Na metal in E-NaClO ₄ right after Na addition (representative for all electrolytes), b) Na metal in E-NaClO ₄ , c) in P-NaClO ₄ and d) in E-NaPF ₆ after three days.	39
Figure 7. Optical microscopy images of Na metal on a polyethylene film, filled with E-NaClO ₄ in a sealed cell. Pictures were recorded after a) 1 min, b) 15 min, c) 1 hour, d) 1 day, e) 3 days and f) 10 days. The yellow highlighted area optically shows a time-resolved reaction on the Na surface.	40
Figure 8. Comparison of L/Na and L/AC cell performance with different organic electrolytes at charging/discharging currents of 50 mA g ⁻¹ : a) electrochemical cycling stability of L/Na cells, b) electrochemical cycling stability of L/AC cells, c) Coulombic efficiencies of L/Na cells and d) coulombic efficiencies of L/AC cells.	43
Figure 9. Galvanostatic charge and discharge profiles of the 2 nd and 50 th cycle for a) L/Na-E-NaClO ₄ and b) L/AC-E-NaClO ₄ ; c) XRD patterns of cycled L/AC-E-NaClO ₄ and L/Na-E-NaClO ₄ electrodes and the respective pristine LTO electrode.	45
Figure 10. a) F1s and b) C1s spectra of the pristine LTO electrode and all samples after 20 cycles in the sodiated state with proposed assignments.	46
Figure 11. a) Na metal in E-NaClO ₄ right after Na addition (representative for all electrolytes), b) Na metal in E-NaClO ₄ + 5 % FEC and c) in 1M NaClO ₄ in diglyme after three days.	50

Figure 12.	a) Rietveld-refined diffractogram, including peak positions and b) scanning electron micrograph of Sb_2O_3 powder.	51
Figure 13.	Sb_2O_3 based electrode cycled at 0.2 A g^{-1} in D, E and F solutions: a) electrochemical cycling stability, b) Coulombic efficiency, c) galvanostatic charge/discharge profiles of the 1 st cycle, d) galvanostatic charge/discharge profiles of the 3 rd cycle.....	52
Figure 14.	Scanning electron micrographs with high magnification insets of Sb_2O_3 electrodes: a) pristine, b) after 50 cycles in solution E, c) after 50 cycles in solution D, d) after 50 cycles in solution F.....	55
Figure 15.	Scanning electron micrographs and EDS maps of Sb_2O_3 electrodes: a) pristine, b) after 50 cycles in solution E, c) after 50 cycles in solution D, d) after 50 cycles in solution F. EDS signals of antimony are highlighted in green and signals of carbon in magenta.	56
Figure 16.	C 1s, O 1s and Sb 3d XPS spectra of Sb_2O_3 electrodes: a) + b) pristine, c) + d) after 50 cycles in solution E, e) + f) after 50 cycles in solution F, g) + h) after 50 cycles in solution D.	58
Figure 17.	Cell components removed after 50 cycles: a) electrolyte solution D, b) electrolyte solution F, c) separator cycled in solution D, d) separator cycled in solution F, e) sodium-metal counter electrode cycled in solution D, f) sodium-metal counter electrode cycled in solution F.	59
Figure 18.	Scanning electron micrographs and the corresponding EDS maps of the sodium counter electrode after 50 cycles in a) + c) electrolyte solution F, b) + d) electrolyte solution D. EDS signals of antimony are highlighted in green and signals of sodium are highlighted in orange. f) Comparison of EDS spectra of the sodium counter electrodes cycled in electrolyte solutions F and D, respectively.	60
Figure 19.	a) Rietveld-refined diffractogram and b) SEM image of the Sb powder; c) O 1s and Sb 3d XPS spectrum of a pristine electrode with 90 % (w/w) synthesized Sb and 10 % (w/w) CMC composition; d) Electrochemical cycling stability of this electrode at 0.2 A g^{-1}	64
Figure 20.	Electrochemical cycling stability at 0.2 A g^{-1} for different Sb/C65 ratios normalized to a) the Sb active mass and b) the Sb/C65 active mass; c) corresponding Coulombic efficiencies of all composites; d) magnification of Coulombic efficiencies for the Sb/C65 ratios of 75/15, 70/20, and 40/50.	65
Figure 21.	Overview of parameters obtained from GSA, TEM, Raman, and electrochemical analysis (galvanostatic charge/discharge cycling with potential limitation). The carbons are	

arranged depending on their properties towards the related characteristic with the corresponding value below.	67
Figure 22. Transmission electron micrographs of a) C65, b) SuperP, c) KS6L, d) Nanostars, e) OLC1300V, and f) OLC1700A.....	68
Figure 23. a) Raman spectra of the carbon samples, b) electrochemical cycling stability at 0.2 A g ⁻¹ for electrodes composed of 90 % (w/w) of the respective carbon and 10 % (w/w) CMC; c) and d) the related Coulombic efficiencies.....	69
Figure 24. Galvanostatic charge/discharge profiles at 0.2 A g ⁻¹ for a) Sb/C65, b) Sb/SuperP, c) Sb/OLC1300V, d) Sb/OLC1700A, e) Sb/Nanostars, and f) Sb/KS6L.	71
Figure 25. a) Electrochemical stability at 0.2 A g ⁻¹ and b) rate performance of the respective Sb/C electrodes; c) and d) Coulombic efficiencies.	72
Figure 26. Scanning electron micrographs of a) pristine Sb/C65, b) Sb/C65 after 50 cycles, c) pristine Sb/OLC1300V and d) Sb/OLC1300V after 50 cycles.....	73
Figure 27. Amounts of metallic Sb in Sb/C electrodes obtained from X-ray photoelectron emission spectroscopy.....	75
Figure 28. Rietveld-refined diffractograms of a) commercial Sb powder, b) ball milled commercial Sb powder, c) commercial Sb powder milled with 10 % (w/w) C65 and d) synthesized Sb nanopowder.	78
Figure 29. SEM images with high magnification insets of a) commercial Sb powder, b) ball milled commercial Sb powder, c) commercial Sb powder milled with 10 % (w/w) C65 and d) synthesized Sb nanopowder.	79
Figure 30. a) Electrochemical cycling stability at 0.2 A g ⁻¹ and b) Coulombic efficiencies of Sb/C electrodes with different Sb powders and C65.	80
Figure 31. Scanning electron micrographs of pristine electrodes: a) synthesized Sb + 20 % C65, b) commercial Sb + 20 % C65, c) milled commercial Sb + 20 % C65 and d) commercial Sb milled with 10 % C65 and subsequent addition of 12 % C65.....	81
Figure 32. a) Ragone diagram and b) cycling performance of an NMFO//Sb-com/C65 mill + 10 %C65 full-cell cycled between 1.5 V and 4 V. The cell in b) was cycled at a specific current of 0.1 A, which is referred to the negative electrode mass (binder mass excluded). Schematic values of LIBs are adapted from Ref. [183] and indicated by the grey dashed line in a).	87

Figure A1.	a) Cyclic voltammogram recorded at a scan rate of 0.25 mV s^{-1} with the redox couple chosen for the determination of the half-wave potential (indicated by the dashed grey line), and b) shifted potential of the AC-QRE in E- NaClO_4 .	101
Figure A2.	Gas sorption isotherms and pore volume distributions of a) C65, b) SuperP, c) KS6L, d) Nanostars, e) OLC1300V, and f) OLC1700A.	103
Figure A3.	Measured and fitted Raman spectra of a) C65, b) SuperP, c) OLC1700A, d) OLC1300V, e) Nanostars, and f) KS6L.	104
Figure A4.	Scanning electron micrographs of a) pristine Sb/SuperP, b) Sb/SuperP after 50 cycles, c) pristine Sb/OLC1700A, d) Sb/OLC1700A after 50 cycles, e) pristine Sb/Nanostars, f) Sb/Nanostars after 50 cycles, g) pristine Sb/KS6L, and h) Sb/KS6L after 50 cycles.	105
Figure A5.	Scanning electron micrographs of a) Sb/C65, b) Sb/SuperP, c) Sb/OLC1300V, d) Sb/OLC1700A, e) Sb/Nanostars, and f) Sb/KS6L after 50 cycles.	106
Figure A6.	C 1s, O 1s and Sb 3d XPS spectra of a) Sb/C65, b) Sb/SuperP, c) Sb/KS6L, d) Sb/Nanostars, e) Sb/OLC1300V, and f) Sb/OLC1700A after 50 cycles.	107
Figure A7.	Electrochemical cycling stability at 0.2 A g^{-1} and corresponding Coulombic efficiency of Sb-com/30C65 mill + 10 % C65.	108
Figure A8.	Potential curve of the NMFO//Sb/C full cell and the respective measured profiles of the anode and cathode over time. The arrow indicates the potential-shift of the electrodes. ...	108

Tables

Table 1. Summary of different parameters of Sb/C composites in the state-of-the-art literature. Not available data from the literature references are donated as “n.a.”. AB: Acetylene black; MWCNTs: Multi-walled carbon nanotubes; PAN: Polyacrylonitrile. *not mentioned if the conductive additive is included to the normalization.	28
Table 2. Overview of all applied electrolytes with the labelling corresponding to the respective section.	30
Table 3. Ingredients and compositions of all applied electrodes and the corresponding sections. The compositions are referred to the dry electrode mass.	33
Table 4. Results from elemental analysis of the carbon samples (no H or S detected).....	68
Table 5. Resistances of Sb/C electrodes calculated from the IR drop at 4 A g^{-1} . Sb/C electrodes were prepared in a ratio of 70 % (w/w) Sb nanopowder, 20 % (w/w) C of the respective carbon, and 10 % (w/w) CMC (dry mass).	71
Table A1. Values obtained from gas sorption analysis of the different carbon samples (corresponding graphs are shown in Figure A2).	101
Table A2. Values obtained from Raman analysis of the different carbons (corresponding graphs are given in Figure A3).	102

Zusammenfassung

Diese Arbeit beleuchtet den Einfluss entscheidender Komponenten in Natrium-Ionen Batterien. Na-Metall wird häufig als Gegen- und/oder Referenzelektrode in der Literatur eingesetzt, um die Eigenschaften eines Aktivmaterials in Na-Ionen Batterien elektrochemisch zu untersuchen. Diese Thesis zeigt, dass Na spontan mit den häufig verwendeten, auf organischen Carbonaten basierten Elektrolyten reagiert. Solche Nebenreaktionen zwischen den Na-Gegen- und/oder Referenzelektroden führen zu veränderten Eigenschaften des Elektrolyten und wirken sich negativ auf die Oberflächenchemie der Arbeitselektrode aus. Eine Stabilisierung des Na-Metalls kann durch Zugabe von Fluorethylencarbonat zu Carbonat-basierten Lösungsmitteln oder durch Ersetzen solcher Lösungsmittel durch Diglyme erfolgen. Der Einfluss dieser Lösungsmittel kann durch elektrochemische Messungen von Sb_2O_3 -basierten Halbzellen bewertet werden. Die Zugabe von Fluorethylencarbonat führt zu einer geeigneten Dicke der Fest-Elektrolyt Interphase und verhindert, dass die Elektrode stark reißt. Diglyme dagegen löst Sb-Ionen während des Zyklierens, was zu Verunreinigungen, einem starken Kapazitätsverlust und einer unregelmäßigen elektrochemischen Signatur führt. Daher ist der Fluorethylencarbonat-haltige Elektrolyt für die Untersuchung von Materialien mit hoher Kapazität wie Sb am besten geeignet. Die Energiespeicherung von Sb durch Legierungsreaktionen mit Na erfordert ein spezielles Elektroden-design für eine hohe Leistungsstabilität. In dieser Arbeit wird systematisch der Einfluss der Kohlenstoffeigenschaften auf Sb/C-Verbundelektroden untersucht. Anstelle einer komplexen Hybridisierung von Sb und C werden die Komponenten mechanisch gemischt, um stabile Sb/C Elektroden zu erhalten. Dies ist nur unter Berücksichtigung der physikalischen, chemischen und strukturellen Merkmale der Kohlenstoffe möglich. Die beste Leistung wird nicht nur durch die hohe Oberfläche oder den Heteroatomgehalt ausgelöst, sondern insbesondere durch die beste Fähigkeit, sich homogen zwischen den Sb Partikeln zu verteilen. Dies ist am besten für synthetisiertes Sb-Nanopulver mit Hilfe von Kohlenstoffzwiebeln möglich, die bei 1300 °C unter Vakuum hergestellt werden. Durch Volumenänderungen verursachte Elektrodenrisse werden so verhindert und die Homogenität der Fest-Elektrolyt Interphase wird verbessert, was zu einer bemerkenswerten Ratenfähigkeit und einer hohen Zyklenstabilität führt. Um den Einfluss der Sb-Partikelgröße zu untersuchen, wird das synthetisierte Pulver durch kommerzielles Sb ersetzt, das vor der Elektrodenherstellung kugelmahlen wird. Zusätzlich wird ein Sb/C Komposit aus kommerziellen Materialien durch Kugelmahlen hergestellt. Ein Vergleich aller Sb/C Elektroden zeigt, dass die Partikelgröße von Sb ein wesentlicher Faktor ist: Je kleiner die Partikel, desto höher die Zyklenstabilität und desto weniger Kohlenstoff wird zum Dämpfen von Volumenänderungen benötigt. Eine gründliche Anpassung der Sb- und C-Mengen und ihrer Merkmale ist erforderlich, um das bestmögliche elektrochemische Verhalten zu erzielen.

Abstract

This thesis focuses on the impact of critical components in sodium-ion battery cells. Sodium-metal is commonly applied as a counter and/or reference electrode to electrochemically characterize the properties of an active material in sodium-ion batteries. The occurrence of spontaneous reactions between Na metal and most commonly applied organic carbonate-based electrolytes is revealed in this thesis. Such side reactions between Na counter and/or reference electrodes lead to altered properties of the electrolyte and negatively affect the surface chemistry of the working electrode, which emphasizes the importance of critical interpretation of electrochemical experiments. Stabilization of the sodium metal can be achieved by fluoroethylene carbonate addition to carbonate solvents or the replacement of such solvents by diglyme. The influence of these solvents on several cell components is exemplarily elaborated by electrochemical measurements of Sb_2O_3 -based half cells. The addition of fluoroethylene carbonate entails an appropriate thickness of the solid electrolyte interphase and thus prevents the electrode from severe cracking. This work also proves that diglyme removes Sb-ions from Sb_2O_3 during electrochemical cycling, which leads to contaminations, an irregular electrochemical signature caused by side reactions and a strong capacity loss. Therefore, the fluoroethylene carbonate-containing electrolyte is found to be appropriate for the study of high capacity materials like antimony. Sb stores energy based on alloying reactions and requires a bespoke electrode design to enable high-performance stability. This work systematically explores the impact of carbon properties on Sb/C composite electrodes for sodium-ion batteries. Instead of complex hybridization of Sb and C, the ability of mechanical mixing to yield stable high-performance Sb/C negative electrodes is shown. This is only possible by considering the physical, chemical, and structural features of the carbon phase. The best performance is not only triggered by a high surface area or heteroatom content but especially by the best ability to homogeneously distribute within the Sb matrix. The latter is best enabled for synthesized Sb nanopowder by onion-like carbons, which were synthesized at 1300 °C under vacuum. Electrode cracking caused by volume changes is successfully prevented, and the homogeneity of the solid/electrolyte interphase is significantly improved. This leads to a remarkable rate capability and high cycling stability. To examine the impact of the Sb particle size, the synthesized Sb powder was replaced by commercial bulk Sb powder, which was ball milled previous to the electrode preparation. Additionally, an Sb/C composite of commercial Sb and commercial conductive additive C65 was prepared by ball milling. A comparison of all Sb/C composite electrodes demonstrates that the particle size of Sb is an essential factor: the smaller the particles, the higher the cycling stability and the less carbon is needed to buffer volume changes. A thorough adjustment of the Sb and C amounts and their features is necessary to obtain the best possible electrochemical behavior.

1 Introduction

Sodium-ion batteries (NIBs) were initially investigated in parallel to lithium-ion batteries (LIBs) in the 1970s and 1980s.^[1] Nevertheless, LIBs have become the major power source for electric vehicles and portable electronic devices due to the rapid development and its commercialization by Sony in 1991.^[2,3] This has led to an enormous demand for available lithium resources.^[4] By exploiting the lithium sources, the price of the metal will dramatically rise as a consequence of the growing electrification.^[5] This issue is amplified by geopolitical and environmental concerns, as the raw materials are often extracted in politically and environmentally sensitive areas.^[6,7] Therefore, enormous interest in energy storage systems beyond lithium aroused throughout the past years.^[8] Especially NIBs have revived since 2011 encouraged by the natural abundance of sodium, which is the fourth most abundant element in the earth's crust.^[1,9] NIBs are highly promising low-cost large scale stationary electrochemical storage systems as the lower energy and power density compared to LIBs plays a tangential role.

The transferability of LIB research results to NIB research raised high expectations to a time-saving NIB development due to the similar chemistry of lithium and sodium. It is estimated that the knowledge and experience gained from LIB research will accelerate NIB research, and reduce investment costs. Nevertheless, this background often leads to negligence of the altered features of sodium in the state-of-the-art literature. The electrochemical behavior of sodium and lithium commonly differs in the respective battery application.^[9] The main causes are the higher reactivity of the sodium metal and the larger size of the sodium-ions that influence the phase stability, the transport properties, and the solid electrolyte interphase (SEI).^[9] The step from lithium to sodium is still an effective strategy to reduce the dependence on lithium if the following differences are considered:^[9]

- Sodium has a lower melting point and an enhanced reactivity when compared to lithium. This causes safety issues, especially when applying sodium metal electrodes.
- The larger size of the sodium-ion compared to the lithium-ion causes higher volume changes of the material during cycling, which leads to enhanced mechanical stress inside the electrodes. In contrast, the larger ion-size is accompanied by less charge density, leading to less polarization of the chemical environment of sodium-ions than lithium-ions. This can affect the chemical bonding and ion mobility.

- Sodium has a higher reduction potential than lithium, meaning that some substances are expected to be thermodynamically more stable in direct contact with the metal. Nevertheless, the enhanced chemical reactivity of sodium can, in turn, lead to instabilities when the metal comes in contact with certain substances.
- In contrast to Li^+ , Na^+ cannot be inserted in aluminum at low potential. This has the advantage that aluminum can be used as a current collector for both electrodes in NIBs, avoiding the utilization of expensive copper foil.
- Sodium and lithium salts have different properties, especially when being dissolved in solvents. This leads to different characteristics of the electrolytes in LIBs and NIBs.

The contemplation of these aspects requires systematic research approaches to adjust the components in NIBs with similar success as achieved for LIBs. Several achievements in NIB research are presented in the state-of-the-art literature. The development of positive electrode materials derived from LIB research provided some promising candidates. For example, layered sodium transition-metal oxides,^[10,11] polyanion materials^[12] or Prussian blue analogues^[13] can deliver capacities up to 180 mAh g^{-1} with redox potentials between 2.5 and 3.8 V.^[8,14] Furthermore, various combinations of organic electrolytes established for the LIB technology were transferred to NIB systems.^[15-21] However, the increased reactivity of sodium metal, which is used as a counter and reference electrode for electrochemical half-cell tests, usually remains neglected. Half-cell measurements are inevitable to precisely characterize the electrochemical behavior of active electrode materials. A study by Iermakova *et al.*^[22] reveals a reduced electrochemical stability of symmetric Na/Na cells in conventional organic electrolytes when compared to the Li/Li cells. The authors assumed that this instability is caused by effects like electrolyte decomposition and electrical contact loss between metallic Na and the current collector.^[22] These effects can lead to incorrect conclusions obtained from Na metal-containing half-cell measurements. Their work is one of the numerous examples, that demonstrate a different behavior when comparing lithium and sodium-based systems. Such surveys pave the way for this thesis.

A methodical study of the interactions between sodium metal and the most established carbonate-based electrolytes is provided in this work. On the one hand, this study uncovers detrimental interactions of sodium metal with the electrolyte. On the other hand, successful perspectives to stabilize the sodium metal inside carbonate-based electrolytes are presented by addition of fluoroethylene carbonate (FEC) or the replacement of carbonate-based solvents by ethers like diglyme. Furthermore, the interplay of electrolyte solvents with several cell components is

investigated by applying a Sb_2O_3 based working electrode. Sb_2O_3 acts as a model material with a multi-step conversion and alloy type charge storage. This offers a basis for the analysis of the complex interplay between the electrolyte and the active material, providing the most stable electrolyte composition towards different cell components. It is found that ethers, like diglyme, can dissolve Sb^{3+} , which then migrate to the counter electrode and can be deposited on the Na metal during cycling. Different from the adverse behavior of diglyme, FEC containing carbonate-based electrolytes protect the sodium metal from side reactions and form a high-quality, unique polymeric SEI on the Sb_2O_3 based working electrode. Therefore, the addition of FEC is found to positively foster the interactions between the cell components.

When taking the step from lithium to sodium, a great obstacle emerges on the negative electrode side. In 1982, Yazami and Touzain firstly demonstrated that Li^+ can reversibly intercalate in graphite.^[23,24] This pioneering finding makes graphite the most successfully applied negative electrode material for commercial LIBs. However, graphite cannot intercalate Na^+ -ions due to energetic aspects like the weaker Na-C interactions when compared to other alkali metal ions.^[25,26] Therefore, hard carbons are applied as an alternative, but they have limited de-sodiation capacities of 100 – 300 mAh g^{-1} .^[27]

This makes the choice of high capacity materials, which can form Na-rich intermetallic compounds through an alloying reaction extremely attractive.^[16,28-31] Nevertheless, the commercialization of such anodes is hindered by a severe capacity fading caused by large volume change and electrode cracking during sodiation and de-sodiation.^[28,32] Besides the adjustments of binders and electrolytes, two main approaches are presented in state-of-the-art literature to counteract these problems: designing suitable nanostructures to improve the kinetics and developing carbon matrices to buffer the volume changes and offer additional diffusion paths.^[30,33-39]

Antimony (Sb) is a promising alloy material, which reacts with sodium to Na_3Sb delivering a high theoretical capacity of 660 mAh g^{-1} .^[40] Still, this material suffers from high volume changes (~300 %).^[29,35,40] An appropriate carbon matrix can counteract such a drawback. Consequently, various carbons combined with Sb in different ratios have been proposed in the literature (section 3, Table 1). A tremendous issue in such studies is the comparability of electrode design operated in various electrochemical systems. It is not possible to extract consistently valid information about the interaction of carbon and antimony from the current state-of-the-art literature due to highly inconsistent parameters and materials.

After proposing a suitable cell setup with an aligned electrolyte system for the characterization of working electrodes, the interaction between carbon and such alloy-type materials is systematically studied in this work. It is presented, that each carbon additive can be able to store charge, meaning that the carbon mass has definitely to be included into normalization. Furthermore, this work offers a guideline for the effective choice of a conductive carbon additive.

The analysis of numerous carbon features like morphology, size, purity, surface area, etc. allows the identification of the beneficial characteristics for the electrochemical NIB performance. By choosing the right carbon, an optimum distribution was achieved between synthesized Sb nanopowder and a unique onion-like carbon (OLC) obtained at 1300 °C under vacuum by nanodiamond deposition. This electrode exhibits an excellent percolation allowing homogeneous current flow around active material particles, which results in high conductivity and superior rate performance. By precise alignment of the Sb and C interplay, electrode cracking was successfully prevented and even tailoring of the SEI was possible. Accordingly, this thesis presents an outstanding electrochemical performance of Sb/C composite negative electrodes based on a facile mechanical mixing electrode preparation.

Since initially only the properties of the carbon were examined, it is particularly important to also evaluate the influence of the properties of the active material. Therefore, the Sb/C electrodes based on synthesized Sb powder were compared to electrodes fabricated with commercially obtained Sb powder, which was ball milled previous to the electrode preparation. By comparing different Sb/C compositions, some of which were also obtained through mechanical ball milling treatment, important conclusions are drawn:

- (I) The electrochemical behavior of Sb-based electrodes is influenced by the individual interactions of the carbons with the respective Sb powder. The properties of both materials are crucial.
- (II) The Sb particle size plays a decisive role: volume changes of nanosized Sb particles can be buffered better by the respective carbon than the volume variations of large bulk Sb particles.

In summary, essential interactions between cell components, electrode ingredients and their interplay during electrochemical cycling in NIB systems are uncovered. This thesis provides a successful strategy of how to locate weaknesses of an electrochemical system, analyze and evaluate these deficiencies and finally improve the performance of a sodium-ion battery.

2 Theoretical background

2.1 Key parameters for batteries

Electrochemical cells like batteries are constructed most generally by two electron-conducting electrodes which are separated from each other and connected by at least one solely ion-conductive electrolyte phase. In a closed circuit, batteries convert the energy of chemical redox reactions, also called Faradaic reactions, into electrical energy providing an electric current between the electrodes. There are two main types of batteries:

- (I) Primary batteries, which are not rechargeable, as the electrodes are irreversibly changed during discharge.
- (II) Secondary batteries, which are rechargeable due to the reversibility of the electrochemical reactions when applying an external load to the cell.

The charge storage mechanism of batteries is based on redox reactions. According to the general electrochemistry nomenclature, the electrode at which oxidation occurs is referred to as anode. In the case of a reduction process, the electrode is labelled cathode. As this work focuses on rechargeable sodium-ion-batteries, it is important to mention that in state-of-the-art alkali-metal-ion battery nomenclature “anode” and “cathode” have become synonyms for “negative electrode” and “positive electrode”. This definition is only in line with the general electrochemistry nomenclature when considering the discharge process. To not confuse the definitions, the general terms “negative electrode” and “positive electrode” will be utilized throughout this work. The key parameters for the understanding of alkali-metal-ion batteries are described in the following section.

2.1.1 Battery potential

The current flow in a battery is caused by a potential difference of the electrodes. One of the most fundamental properties of an electrochemical storage device is the material reduction potential, so-called inner electric potential or Galvani potential φ . If two chemically different phases come in contact, an electric potential difference will form. In a battery, this potential difference occurs between the inner electrochemical potentials of the electrode and electrolyte. An electrochemical cell possesses a Galvani potential difference $\Delta\varphi_+$ for the positive and $\Delta\varphi_-$ for the negative electrode. If both electrodes are in electrolytic contact, an open-circuit voltage (OCV) $\Delta\Delta\varphi$ in the electrochemical equilibrium can be measured as a potential difference of both Galvani potentials:

$$\Delta\Delta\varphi = \Delta\varphi_+ - \Delta\varphi_- \quad (1)$$

The larger $\Delta\Delta\varphi$ the more energy is provided by the battery. A direct determination of the individual Galvani potential differences, meaning the potential difference between one electrode and the electrolyte, is not possible, since the measuring system, which responds to potential differences, must come into contact with both phases. Therefore, only potential differences between an individual electrode and a reference electrode (RE) can be measured. The RE needs to guarantee a constant potential and it is not embedded in the current flow to remain unaffected by current-induced potentials.^[41] Internationally, the standard hydrogen electrode (SHE) is the primary recognized reference electrode. The SHE cannot be applied as a reference electrode in all electrochemical setups, as hydrogen gas is needed. Therefore, potentials can be determined with respect to different reference electrodes. Most commonly, the saturated calomel electrode or the silver-silver chloride electrode are applied in aqueous systems. Electrode materials for metal-ion-batteries in organic electrolytes are commonly characterized with reference to the corresponding metal potential, which is then 0.00 V. For sodium-ion batteries, for example, the RE is usually sodium metal. Nevertheless, alkali metals are often too reactive and therefore contaminate the electrolyte solution.^[22,42] To avoid such contaminations, a quasi-reference electrode (QRE) is often used.^[42,43] QREs are for example metal wires of Ag or Pt^[43], but they can also consist of activated carbon (AC).^[42,44] The potential of a QRE is expected to be constant during an electrochemical measurement.^[43] Yet, the QRE potential is not known and, thus, before reporting values versus the QRE, its potential has to be calibrated versus a true reference electrode.

The examination of processes occurring at exclusively one electrode is realized by a three-electrode cell setup. If the potential is controlled between RE and working electrode (WE), it is usually referred to as half-cell measurement. In an alkali-metal-ion battery, the counter electrode is most commonly the corresponding alkali metal. Nevertheless, this setup can also be applied to examine processes between two working electrodes in a so-called full cell, where the potential is controlled between the positive and negative electrode. Figure 1 shows a schematic three-electrode setup.

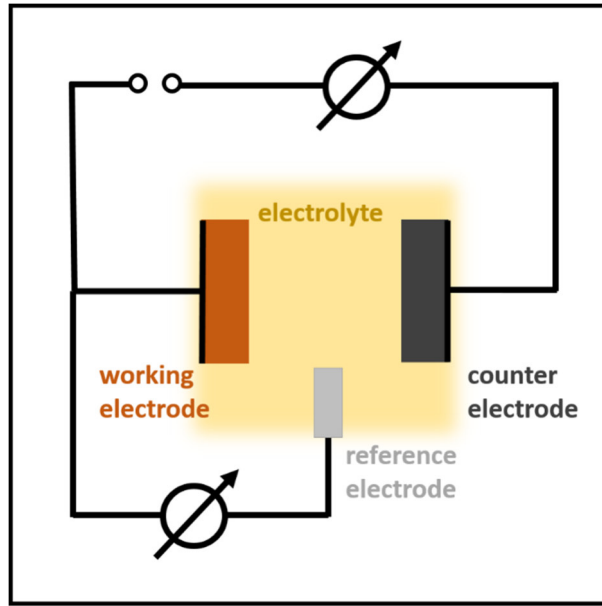


Figure 1. Schematic three-electrode cell setup.

Considering redox reactions, the OCV is conventionally called “electromotive force” E and can be described by the difference of the Gibbs energies ΔG of all reactants and all reaction products of the current producing reaction. If the reduction direction is considered under standard ambient conditions (standard ambient temperature $T^0 = 298.15$ K, standard pressure $p^0 = 100$ kPa) and reactant and product have unit activity:

$$\Delta G^0 = -nFE^0 \quad (2)$$

ΔG^0 is the standard Gibbs energy, E^0 is the standard electrode potential, n is the number of transferred electrons, and $F = 96485$ C mol⁻¹ is the Faraday constant.

ΔG depends on the temperature T and the concentration of the oxidized (c_{ox}) and reduced (c_{red}) species:

$$\Delta G = \Delta G^0 + RT \ln \left(\frac{c_{ox}}{c_{red}} \right) \quad (3)$$

Where ΔG^0 is the Gibbs energy difference under standard ambient conditions (standard ambient temperature $T^0 = 298.15$ K, standard pressure $p^0 = 100$ kPa) and $R = 8.314$ J mol⁻¹ K⁻¹ is the gas constant.

These relations offer a correlation between electrode potential and concentration of a redox couple for electrochemical reactions in a cell given by the *Nernst equation*:

$$E = E^0 + \frac{RT}{nF} \ln \left(\frac{c_{ox}}{c_{red}} \right) \quad (4)$$

Conventionally, E^0 is determined for half-cell reactions versus a SHE with a potential of 0.00 V. These standard reduction potentials are listed in conventional tables and can be found elsewhere.^[45]

2.1.2 Battery capacity and rate capability

The battery capacity indicates the amount of electrical charge Q that a battery can deliver or store. The charge Q is proportional to the time t when applying a constant current I over time:

$$Q = I \cdot t \quad (5)$$

In the following, this charge will be referred to as capacity with the unit mAh g⁻¹ as defined in the common battery nomenclature. According to equation (5), it is necessary to indicate the charge/ discharge current when stating a capacity. The limit of electrochemical charge storage is the theoretical capacity of a material, which is given by Faraday's law of electrolysis.^[46] The theoretical capacity Q_{th} of an active material with molecular mass M can be calculated by:

$$Q_{th} = \frac{z \cdot n \cdot F}{M} \quad (6)$$

Where n is the maximum amount of insertable or extractable charge carriers with the valence number z . In practical application, the theoretical capacity is not reached by reason of polarization effects or losses due to side reactions or material defects. The reachable capacity at different specific charge/ discharge current gives information about the rate capability of the cell. A capacity approaching the theoretical capacity at high charging/discharging current rates displays an optimal rate performance. To have a specification for the capacity-dependent current of an energy storage device, the C-rate [C] is defined as:

$$[C] = \frac{I}{Q} = \frac{1}{t} \quad (7)$$

The C-rate is usually calculated with respect to the theoretical capacity of the material. A C-rate of one can thus be adjusted by applying a current which charges the cell in one hour to its full theoretical capacity.

2.1.3 Coulombic efficiency and solid electrolyte interphase

The Coulombic efficiency (CE) is the ratio of the total charge Q_{out} extracted from the battery to the total inserted charge Q_{in} into the battery throughout a full cycle. It describes the charge efficiency of the electron transfer in %:

$$CE = \frac{Q_{out}}{Q_{in}} \cdot 100\% \quad (8)$$

100 % CE would indicate fully reversible processes that are never performed by a battery. Commercially applied LIBs provide a CE, which is commonly > 99 %.

2.1.4 Cycling stability

Charging and discharging of a battery in a specified voltage range with a defined current is called galvanostatic cycling. The discharge capacity is plotted versus the number of cycles. Normally, this capacity value is reduced in the course of cycling depending on the cycling conditions (charge/discharge current, temperature, voltage range, electrode material and electrolyte stability, etc.). The cycle life of rechargeable batteries is the number of charge/discharge cycles, which is feasible until the discharge capacity value falls below a certain limit.^[47]

2.1.5 Specific energy and specific power

The potential difference and the material capacity influence the specific energy and the specific power of an energy storage device. The specific energy ε in Wh kg⁻¹ is the amount of energy stored in a given system per unit mass:

$$\varepsilon = \frac{1}{3600 \cdot m} \int_{t_i}^{t_f} I(t) \cdot U(t) dt \quad (9)$$

with m in kg as electrode active mass, current I in A, cell voltage U in V and t_i and t_f in s as initial time and final time of charge/discharge.^[48]

The specific power P in W kg⁻¹ is the amount of power (time rate of energy transfer) per unit mass:

$$P = \frac{1}{(t_f - t_i) \cdot m} \int_{t_i}^{t_f} I(t) \cdot U(t) dt \quad (10)$$

Thus the average specific power results by dividing the specific energy through the time which is needed for cell discharging/charging. Energy storage devices are generally aimed to possess

high specific energy and high specific power. To rate an energy storage device, the specific energy and specific power calculated via equations (9) and (10) for different discharging currents are plotted in a so-called Ragone diagram. Moreover, the energy density and power density are analogous values to characterize the amount of energy and power of an electrochemical device per unit volume.

2.1.6 Electrochemical signature

To distinguish and characterize energy storage devices, common electrochemical testing techniques are galvanostatic cycling with potential limitation (GCPL) and cyclic voltammetry (CV). These techniques give access to a variety of characteristics like capacitance, capacity, operating voltage, equivalent series resistance (ESR), cell kinetics or cyclability. For a GCPL experiment, a constant current I is applied and the resulting potential E is measured as a function of time in a specific voltage range. If the potential is plotted versus the insertion or extraction capacity, the occurrence of a voltage plateau will indicate a faradaic reaction (Figure 2a). To further determine the cycle life, the cell is repeatedly charged and discharged.

CV measurements are carried out by applying a voltage ramp $v = \frac{dU}{dt}$ on the cell. The required current to follow this ramp is measured and plotted versus the potential. After reaching a specific set-potential, the potential is ramped in the reverse direction to return to the initial state or a defined potential. Peaks, which appear in a cyclic voltammogram, signalize the proceeding of faradaic redox reactions at a certain potential (Figure 2b). In general, GCPL profiles and cyclic voltammograms display the electrochemical signature of a cell. Figure 2 schematically illustrates the typical electrochemical response of an alkali-metal ion battery negative electrode under a) constant current and b) at a constant voltage ramp.

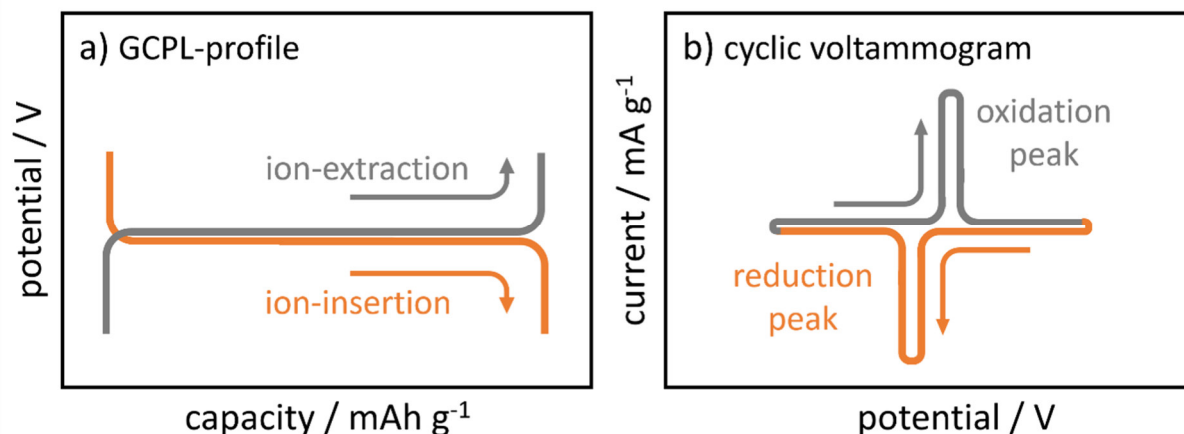


Figure 2. Electrochemical signature of a negative electrode showing a) galvanostatic charge and discharge profiles recorded at constant current and b) cyclic voltammogram collected by applying a constant voltage ramp.

2.1.7 IR-drop

If the potential is plotted against the time, additional information about the electrochemical system, like the cell conductivity can be obtained. The electrolytes' resistive properties follow the Ohmic law ($U = R \cdot I$, where R is the ohmic resistance). A voltage drop (IR drop) occurs by reason of the electrolyte and electrode resistance during current flow.^[49] The IR drop is more pronounced when higher currents are applied. With the difference between the maximum potential (starting point of the IR drop) and a potential after a defined time, the electrical resistance of the cell can be calculated via $R = \frac{U}{I}$. By varying the working electrodes but simultaneously keeping all other components and measurement parameters constant, a relation between the working electrodes' conductivity values can be elaborated.

2.2 Sodium-ion-batteries

2.2.1 Components and working principle

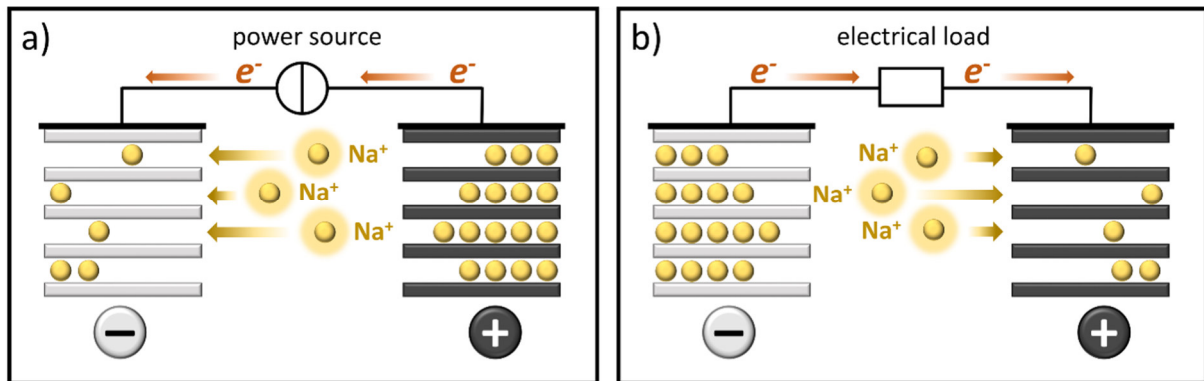


Figure 3. Operating principle of a NIB during charging (A) and discharging (B). The electrons “ e^- ” and Na-ions movement direction is described by arrows (adapted and modified from Ref. [50]).

The schematic setup of a sodium-ion battery is presented in Figure 3. A positive and a negative electrode material are applied on an aluminum current collector and contacted by an electric circuit that either acts as a power source (Figure 3a) or as an electrical load (Figure 3b). Most commonly, a porous membrane soaked in the solely ion-conducting electrolyte acts as a separator and electrolyte reservoir between the electrodes.

The term “insertion/extraction” is often applied as a synonym for intercalation/de-intercalation in the literature.^[51] In this thesis, insertion/extraction is used to describe the general incorporation/removal of alkali-metal-ions inside/from a material independent from the specific mechanism. The classical charge storage mechanism based on intercalation of ions in a host material is well known from LIB research and described with the term “rocking chair”.^[52] The description “rocking chair” is only valid if ion-intercalation happens on the positive and negative electrode. The active electrode materials can electrochemically store charge via different sodiation mechanisms: (I) intercalation, (II) alloy, and (III) conversion.^[51] A detailed comparison of the different electrochemical charge storage mechanisms with examples for positive and negative electrode materials is outlined in section 2.2.2.

The charge storage mechanism of NIBs is generally based on reversible redox reactions and associated insertion/extraction into host structures/materials.^[53] The current flow is caused by a Na^+ insertion potential difference between the electrodes. In the case of NIBs, Na-ions have to enter the bulk of the material to enable redox reactions. Such reactions in the bulk of electrode materials are diffusion-controlled and result in a relatively high charge storage capacity.^[54] By applying a current between the electrodes, the NIB can be charged (Figure 3a). This step leads

to the oxidation of the positive electrode and a simultaneous Na-ion extraction from the positive electrode material into the electrolyte. At the same time, the negative electrode material is reduced and Na-ions are inserted from the electrolyte into its lattice. In order to obtain charge neutrality, electrons have to migrate from the positive to the negative electrode to counterbalance the charge of Na-ion diffusion.^[53] These processes are reversed during discharge and lead to a flux of electrons and Na-ions from the negative to the positive electrode as demonstrated in Figure 3b (the positive electrode material is oxidized while the negative is reduced). In section 2.1.1 the potential difference in a battery was described as electromotive force. The electromotive force in NIBs is based on the sodiation/de-sodiation potentials of both electrodes. The sodiation potential, together with the Gibbs energy of the sodiation process, are the decisive factors whether a material acts as positive or negative electrode. Materials, which exhibit a high sodiation potential versus sodium metal (ideally > 2 V)^[55] will be applied in a positive electrode and referred to as positive electrode materials. Accordingly, materials with low potentials versus sodium metal (ideally < 2 V)^[55] are used as negative electrodes and labelled negative electrode materials.

Elemental sodium metal is usually avoided as a negative electrode. Although a Na-metal electrode provides an extremely high theoretical capacity of 1165 mAh g^{-1} ,^[55] safety concerns due to Na-reactivity and dendrite growth are not resolved.^[8,56] Therefore, the development of safe and efficient high-capacity positive and negative electrode materials is crucial in the research field of NIBs.

Electrodes, which are applied in alkali-metal-ion batteries, are composites consisting of the active material, a conductive carbon additive and a polymeric binder. Typical binders are, for example, polyvinylidene fluoride (PVdF), carboxymethyl cellulose (CMC), etc. The binder content should be as low as possible (generally 3 – 5 %) because most binders are electrical insulators. Typically, binders attain both cohesion between the different particles and between the electrode laminate and the current collector.^[57] An optimized design of polymer binders should be able to decrease electrode delamination/destruction during cycling and guarantee good interface properties.^[17,58] The addition of conductive carbonaceous materials can massively improve the electrochemical performance of the electrode in terms of conductivity, percolation, electrochemical and mechanical stability etc.^[33,59,60] Different conductive carbons are examined in the further course of this work. Therefore, a deeper insight into their properties is given in section 2.2.3.

Electrolytes based on organic liquids are applied in commercial alkali-metal-ion batteries to guarantee ionic conductivity between the electrodes. Nevertheless, such electrolytes are not

stable at low potentials. Therefore, the CE is generally low during the first cycles as a result of irreversible electrolyte decomposition at the electrode.^[61] These initial processes cause the formation of a protective cover layer at the electrode surface, the so-called solid electrolyte interphase (SEI).^[61–63] This additional phase has the properties of a solid electrolyte.^[61] The SEI concept was mainly developed in LIB research. Nevertheless, it is valid for NIBs, as well.^[17,64] The rate capability and cycle life of an alkali-metal-ion battery are highly dependent on the quality of the SEI.^[63] An ideal SEI should have a low electronic but high alkali-ion conductivity, an appropriate thickness, good flexibility and uniform morphology.^[59,63] As the reactivity of organic electrolytes plays a crucial role in this work, state-of-the-art organic electrolytes and their characteristics are presented in section 2.2.4.

After the selection of the components for a full-cell NIB, the effective capacity determination is crucial when applying composite electrodes as charge neutrality has to be guaranteed: the charge of both electrodes has to be equal. Accordingly, the capacities of positive and negative electrodes need to be precisely balanced. This is possible by adjustment of the electrode mass via electrode thickness. Therefore, the effective capacity of each electrode has to be determined in a three-electrode half-cell setup (Figure 1), where sodium metal is commonly used as a counter electrode. The metal can provide a large number of sodium-ions which are consumed during sodiation of the working electrode. This prevents depletion of Na^+ in the electrolyte and allows a precise determination of the effective electrode capacity.

This work aims to describe and evaluate the electrolyte reactivity towards sodium metal and antimony(III)oxide containing electrodes in NIBs as well as the influence of carbonaceous additives on alloy type antimony based electrodes. Therefore, special interest is paid to the basic properties of the respective components in the following.

2.2.2 Charge storage mechanisms of active materials in sodium-ion batteries

Active electrode materials can be subdivided into three groups based on their charge storage mechanisms. In the following, the processes are described with a focus on negative electrode materials. The same processes can be transferred to positive electrode materials in a reversed sequence. A schematic illustration of the described material-types and their respective storage mechanism is demonstrated in Figure 4.^[51]

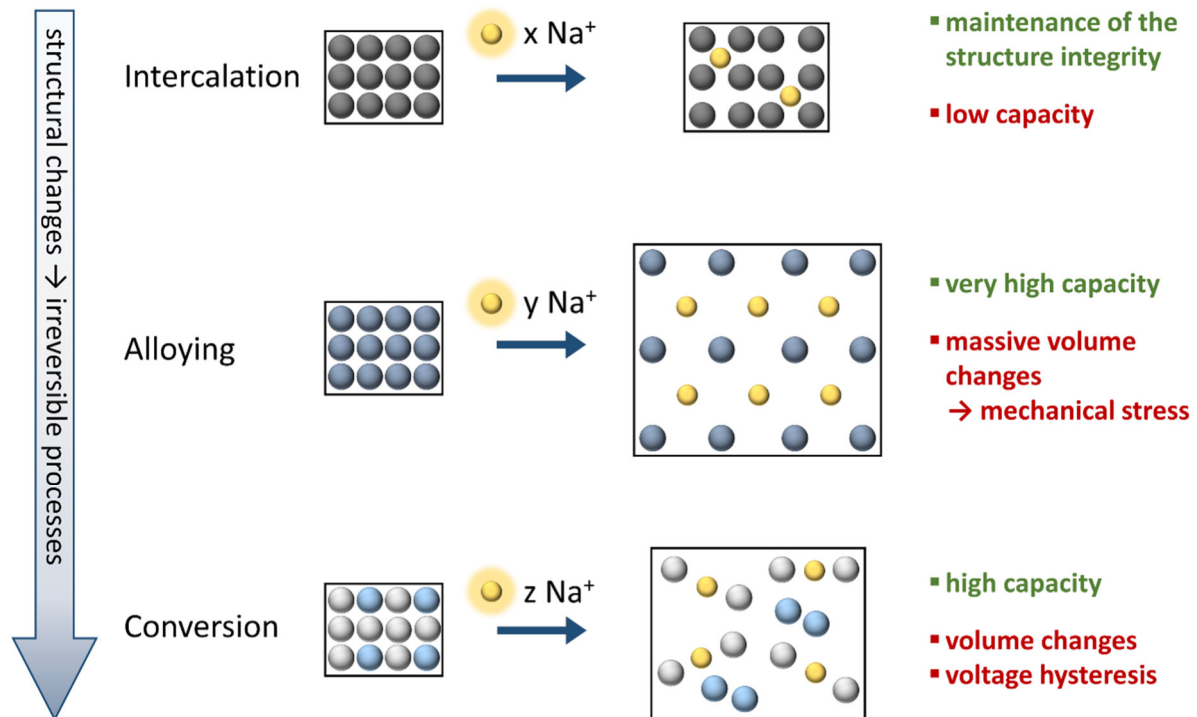
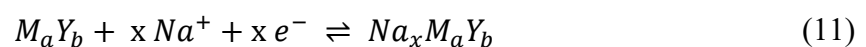


Figure 4. Different charge storage mechanisms of electrode materials for sodium-ion batteries. Circles are representative of different atoms in a crystal lattice (adapted and modified from Ref. [51]).

- (I) Intercalation-type materials are the most prominent compounds. Na-ions from the electrolyte are intercalated between the layers or in free lattice sites of the active material structure (M_aY_b). Simultaneously, the material can accept electrons, which leads to a reduction of the active material lattice (equation 11).^[8] Thus, the material combines both features: ion-conductivity and electron conductivity.^[65] The basic structural framework of the host is kept after ion-insertion.^[55,65] Such materials can be applied as negative or positive electrode materials depending on the redox potential of the active material.^[55,66]

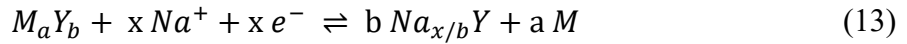


- (II) Alloy-type materials are metals (M), which can form Na-rich intermetallic compounds through alloying reaction mechanisms (equation 12).^[30] Such alloy reactions typically

take place at low potentials versus sodium. Therefore, these compounds are usually applied as negative electrode materials.^[30,51]



(III) Conversion-type materials are at least binary $M_a Y_b$ transition metal compounds (e.g. metal oxides, sulphides, phosphides or fluorides),^[51] which form metallic nanoparticles inside a matrix of $Na_x Y_b$ when becoming sodiated (equation 13).^[51] The redox potential increases with the ionicity of the M-Y bond.^[66] While oxides as conversion electrodes commonly demonstrate potentials near 2 V,^[66] sulphides and phosphates have even lower redox potentials. For this reason, such materials are commonly applied as negative electrodes.^[30,51,66] However, fluorides have shown a sodiation potential above 3 V due to the strong ionic character of M-F bonds^[66] and are therefore suitable as positive electrode materials.^[66,67]



Up to the present, intercalation materials provide the best choice for positive electrodes in NIBs, especially when offering an appropriate host structure for Na^+ .^[55] To provide high cycling stability, the volume changes of the host structure should be as negligible as possible during Na^+ insertion/extraction.^[55] The preferred coordination number of Na in a lattice is six and thus requires either an octahedral or prismatic arrangement.^[55] This characteristic inherently limits the range of potential positive electrode host structures. Three main types of positive electrode materials for NIBs are depicted in state-of-the-art literature:^[8,68] layered sodium transition-metal oxides like $NaFeO_2$ ^[10] or $P2-Na_{2/3}Mn_{2/3}Fe_{1/3}O_2$ ^[11], polyanion materials as $Na_3V_2(PO_4)_3$ ^[12] and Prussian blue analogues, for example, $NaMFe(CN)_6$ ^[13] ($M^{II} = Mn, Fe, Co, Ni, Zn$). There are several compositions of all three types which can deliver capacities up to 180 mAh g^{-1} with redox potentials between 2.5 and 3.8 V.^[8,14]

Intercalation based negative electrode materials for NIBs, like layered $Na_2Ti_3O_7$ ^[69] or spinel-structure $Li_4Ti_5O_{12}$,^[56,70] are well known for high reversibility as the structural integrity is predominantly kept during sodiation and de-sodiation.^[8,71] Nevertheless, one of the main differences between sodium and lithium-ion batteries is the intercalation behavior into graphite. Graphite is successfully used as anode material for commercial lithium-ion batteries but cannot simply intercalate Na^+ -ions.^[25] Due to the chemical potential of sodium electroplating of the metal on the surface of graphite is energetically favorable.^[26,72] Hard carbons have been found

as appropriate alternatives for NIBs due to an expanded interlayer distance compared to graphite.^[73] These non-graphitizing carbons are synthesized at high temperatures (ca. 1000 °C) and have a high fine-structured porosity.^[27,55] The structure is characterized by randomly oriented crystallites with only small graphitic areas^[74] and can be described in a simplified model as “house of cards” or “falling cards model”.^[72,75] Hard carbons show a two-step sodium insertion behavior: the intercalation of Na⁺ between the layers occurs first at about 0.2 V vs. Na/Na⁺, whereas the low potential region near 0.0 V vs. Na/Na⁺ is related to the adsorption of Na⁺-ions into the micropores.^[27,76] However, hard carbons have limited de-sodiation capacities of 100 – 300 mAh g⁻¹.^[27] In general, the low capacity originating from intercalation mechanisms is a huge drawback.^[55]

Therefore, the class of high capacity alloy-type materials like tin (Sn), phosphorus (P), or antimony (Sb) are considered as very promising in the state-of-the-art literature.^[16,28–31] Such materials can deliver exceptionally high capacity values up to 2000 mAh g⁻¹, which was attained by Gao *et al.*^[77] with a carbon/red phosphorous/graphene electrode. Yet, the application of red phosphorus can imply significant safety concerns due to its flammability and explosiveness when coming in contact with oxidizing agents.^[78] Antimony is a very common alloy material, which reacts with sodium to form Na₃Sb with a theoretical capacity of 660 mAh g⁻¹.^[40] Since micro-sized Sb powder was reported to sustain over 100 cycles vs. Na/Na⁺ preserving capacity values of ca. 600 mAh g⁻¹ at a rate of 2C,^[40] it can be considered as a very promising candidate. Still, a general key-issue of all materials with alloy mechanism is the severe capacity fading, which prevents the commercialization of such anodes.^[28,32] The main reason for this fading is the large volume change during sodiation and de-sodiation, which is schematically demonstrated in Figure 4. Volume changes can lead to electrode cracking and aggregations and therefore to slower kinetics.^[30] If the volume expansion is not properly buffered, a massive pulverization can take place, causing severe cracking of the electrode.^[30,32] As a result, new surface areas are exposed, and the SEI is continuously restructured. This is a crucial drawback as side reactions steadily proceed during cycling leading to low CE.^[8,29] Furthermore, an inhomogeneous thickness and composition of the SEI can partly block the charge transfer and cause a rapid capacity fading.^[62,79–82]

Besides the adjustments of binders and electrolytes, two main approaches are presented in the state-of-the-art literature to counteract these problems: designing suitable nanostructures to improve the kinetics, and developing carbon matrices to buffer the volume changes and offer additional diffusion paths.^[30,33–39] Hence, the relevance of carbonaceous additives is discussed in section 2.2.3 and investigated for Sb-based electrodes in section 6.

Conversion-type materials are also described in the state-of-the-art literature.^[55,67] A full reduction of the metal during discharge generally leads to higher capacities compared to intercalation compounds.^[39,67] Hu *et al.*^[83] reported promising features of Sb₂O₃ as anode material for NIBs. A high capacity of 550 mAh g⁻¹ at 0.05 A g⁻¹, together with an exceptional rate performance and long cycling stability, were obtained due to the conversion-alloy mechanism, which was uncovered in their work.^[83] When comparing the alloy and the conversion mechanism (Figure 4), only one sodiated phase occurs in the alloy reaction. Unlike that, several compounds and phases are formed during charging due to the conversion mechanism. This leads to a highly complex electrochemical system. Additionally, such phase transitions can also result in high volume changes and consequent electrode cracking.^[59,67,84,85] However, the most problematic issue of the conversion mechanism is a large voltage hysteresis between discharging and charging, leading to poor efficiency.^[51] This effect is most pronounced after the first cycle and can thus be associated with a crystallinity loss of the pristine material after the first re-oxidation.^[83,86] Additionally, the generation of various phases can enhance the reactivity of the active material towards other cell components such as the electrolyte, which is particularly examined in section 5.3 for Sb₂O₃-based negative electrodes.

All three material types are applied in this work for the examination of different reactivity aspects in sodium-ion batteries. Li₄Ti₅O₁₂, which exhibits an intercalation storage mechanism, is chosen as an electrode material to evaluate the electrolyte reactivity towards sodium metal. An antimony oxide-based negative electrode is depicted as an example of the enhanced reactivity of the active material towards the electrolyte triggered by the conversion mechanism. The influence of different carbon additives on Sb-based alloy-type negative electrodes is evaluated with a focus on the properties of the applied carbons.

2.2.3 Carbonaceous additives

Conductive carbon additives are highly relevant for the electrical percolation of the electrode as they form a conductive network and thus improve the electrical and thermal conductivity.^[60] A high conductivity, resulting from the ideal electrode percolation is crucial for high specific power and energy.^[33,60] Therefore, the interplay of the active material, binder and conductive additive has to be properly adjusted. Ideally, the carbon additive should fill the interspaces between the active material particles.^[60] In addition, a conductive carbon can absorb and retain the electrolyte and promote an improved contact between the electrolyte and the active material.^[87–89] These general advantages of conductive carbons are independent of the active material. Yet, alloy and conversion type materials require an advanced synergy between carbon and the active material. The carbon will additionally support the task of a buffering agent for the massive volume changes.^[28,30] Therefore, high efforts have been made to hybridize carbons with active materials.^[28,30,35–38,90,91] Even though this class of hybrid materials can show promising results, large-scale production is difficult. The altering of established and optimized synthesis processes of commercial materials is time-consuming and cost-intensive. From the industrial point of view, such aspects of enhanced costs should preferably be avoided. Therefore, the combination of carbon and active material should preferably take place by mechanical mixing.

A facile mixing process is applied in this work to merge and characterize six different carbon materials as conductive additives with Sb nanopowder in NIB electrodes, namely, two types of carbon blacks (SuperP and C65), graphite (KS6L), carbon nanohorns (Nanostars), and two types of onion-like carbons (OLCs). These specific carbon materials were selected to cover an array of properties, including different size, shape, surface area, degree of ordering (graphitization), and heteroatom concentration. Regarding these carbon materials, the following aspects should be noted.

SuperP and C65 are widely used commercial conductive additives for LIBs and NIBs.^[33,60] Both types are characterized by a network of round shaped particles with a size of ~20 nm.^[60] These carbons are reported to impact the electrical resistivity, ionic resistivity, and electrode density.^[60] SuperP was additionally reported as a suitable anode material for NIBs due to its ability to insert sodium-ions.^[92,93] Nevertheless, their effects as conductive additives were almost solely studied for LIBs.^[60,94–99]

The conductive additive should be highly conductive and electrochemically inactive, which exactly applies to graphite when applied in NIB electrodes. Graphite consists of crystalline, flat layers, which run parallel and are named "basal planes". One layer consists of covalently linked

hexagons with sp^2 -hybridized carbon atoms which form a σ -bond with each neighbor including three electrons. The fourth electron is located in a p-orbital with an axis perpendicular to the plane of the layer.^[100,101] The layers are kept together by weak van der Waals-interactions. Therefore, the binding energy between the carbon atoms within the plane is ~ 60 times higher as between the individual planes.^[100] This massive directional dependence of the binding forces results in a clear anisotropy of the mechanical, electrical and thermal properties of the graphite.^[100] The high, almost metallic conductivity along the planes of graphite results from the delocalization of π -electrons.^[100,101] Such a high electrical conductivity and the ability to intercalate Li^+ makes graphite the pioneer negative electrode material for LIBs.^[102,103] Although the inability of sodium-ion insertion into graphite is mostly described as a huge drawback in NIB research,^[8,30,73] there are promising properties of graphite to be utilized as a conductive agent. Nanosized KS6L graphite has been applied as active material^[97,98] as well as conductive additive^[99,104,105] in LIBs and supercapacitors.

Carbon nanohorns consist of graphene tubes with horn-shaped tips.^[106,107] Sp^2 -bonded carbon atoms build up a closed cage of 2 – 5 nm diameter and 40 – 50 nm length. Several thousand linked nanohorns form nanostructured spherical aggregates with a diameter of about 100 nm, so-called graphene nanostars.^[107] Different attempts have been successfully performed to design well-defined pore structures,^[108,109] which make this carbon type interesting for energy storage application. The main application fields are yet supercritical gas storage, catalyst support, and drug delivery.^[107,108,110] Nevertheless, this carbon type has also been used as a conductive component in LIBs or supercapacitors.^[111–116] For NIBs, carbon nanohorns have solely been applied in carbon/phosphorous composites.^[106]

Onion-like carbons are composed of multiple concentric fullerene-like carbon shells with a typical size between 5 – 10 nm.^[117] A large scale production via annealing of nanodiamonds as precursor was established by Vladimir Kuznetsov.^[118] Various structural properties can be obtained depending on the synthesis conditions.^[119] The choice of synthesis parameters like annealing temperature, pressure or synthesis atmosphere^[119] can generate OLCs with different sizes, surface areas, chemical compositions, phases and morphologies.^[117,119,120] These properties will in turn influence the ordering and defectiveness of the individual carbon shells and, therefore, the OLC reactivity and electric conductivity.^[117] This type of carbon was already applied in supercapacitors and batteries as both, active material and conductivity additive.^[119,121–123] The tunable characteristics of OLCs offer a suitable basis to study the interactions of carbon additive properties with active materials in NIBs.

2.2.4 Liquid organic electrolytes

The electrolyte closes the electric circuit between the electrodes by solely ionic conduction. The most important properties of an electrolyte are high ionic conductivity, a large electrochemical operating window, high stability towards the cell components and the ability to create a stable interphase with the electrodes.^[15] The ionic conductivity depends on the electrolyte viscosity, dielectric constant and concentration of charge carriers.^[8] In general, the electrolyte should be non-toxic, safe and low cost. Depending on the application different electrolytes are utilized, for example, solid, gel, organic and aqueous systems. For alkali-metal-ion batteries, the organic type is the most commonly applied electrolyte in both industry and research. A conducting inorganic salt is dissolved in organic carbonate-based solvents. Typically, organic carbonates such as ethylene carbonate (EC), dimethyl carbonate (DMC), diethyl carbonate (DEC), propylene carbonate (PC) etc. are the most frequently used solvents.^[15,124] These solvents are mixed in different ratios and combinations. For NIBs, a remarkable improvement of the cycling stability is observed when 2 – 5 % fluoroethylene carbonate (FEC) is added to the electrolyte solution.^[8,40,125] The major benefit of FEC is its high versatility as it is successfully combined with various electrode materials.^[40,90,125] This can be attributed to the superior polymeric SEI properties triggered by the FEC additive.^[93,126] For this reason, the reactivity of the electrolyte is crucial and determines the quality of the SEI layer.^[62,79,124] Still, the high cost of FEC is a drawback for industrial application. Therefore, the amount of FEC should be as low as possible. Apart from carbonate-based electrolytes, it was reported that different electrode materials show a superior Na⁺ storage performance in ether-based electrolytes like bis(2-methoxyethyl) ether (diglyme) when compared to carbonates.^[127] Therefore, diglyme is considered as a promising alternative to carbonate-based electrolytes in the state-of-the-art literature.^[83,127–129] The chemical structures of all solvent components which are relevant for the understanding of this thesis are presented in Figure 5.

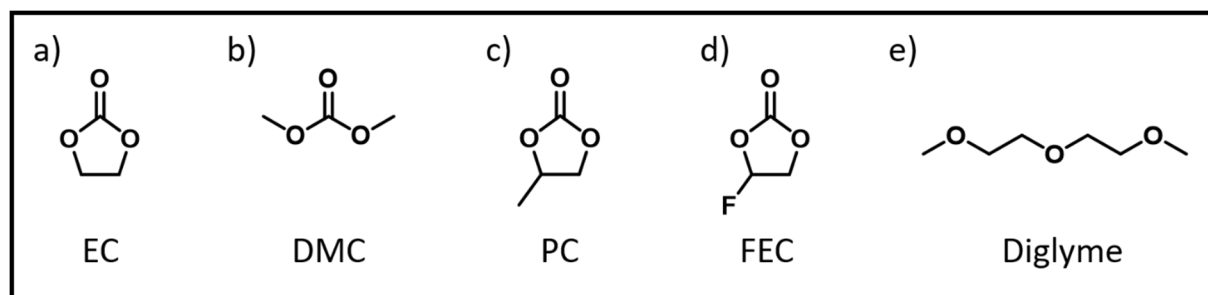


Figure 5. Chemical structures of depicted electrolyte solvents: a) ethylene carbonate (EC), b) dimethyl carbonate (DMC), c) propylene carbonate (PC), d) fluoroethylene carbonate (FEC), e) bis(2-methoxyethyl) ether (diglyme).

These solvents and their combinations can dissolve Na-salts like sodium perchlorate (NaClO_4) or sodium hexafluorophosphate (NaPF_6) to form the most widespread electrolytes for NIBs.^[15,17,70,124,130–132] Every electrolyte ingredient is a crucial component and decides, whether the electrolyte is stable in a specific voltage window and if a stable SEI layer is formed. Consequently, the choice of electrolyte impacts the cycle life of a cell but also affects the specific energy and power, especially depending on the electrode materials and electrode composition.^[133] Therefore, the electrolyte plays a key role in the electrochemical system.

3 State-of-the-art literature and classification of this thesis

Sodium-ion batteries are described as a promising alternative technology to lithium-ion batteries in the state-of-the-art literature.^[15,69,134,135] Justified by the similar chemistry of Li and Na, a wide range of experiments was transferred from LIB systems to NIB systems. One example is the electrolyte composition: solvents and respective sodium-salts were adapted from the LIB systems. However, the increased reactivity of sodium metal, which is used as a counter and reference electrode for electrochemical half-cell tests, usually remains neglected. Iermakova *et al.*^[22] discovered a reduced electrochemical stability of symmetric Na/Na cells in conventional carbonate-based organic electrolytes compared to their Li/Li counterparts. They presumed effects like electrolyte decomposition and electrical contact loss between metallic Na and the current collector as the main root cause for this behavior.^[22] Likewise, Zarrabeitia *et al.*^[136] observed an influence of the sodium metal when comparing Na₂Ti₃O₇/NaFePO₄ full-cells with Na₂Ti₃O₇/Na half-cells. Additionally, Conder and Villevieille^[137] showed, that a passivation of the sodium surface is difficult to achieve in electrochemical cells.

Section 5.1 gives novel insights into the reaction processes of sodium metal towards organic carbonate electrolytes. For this purpose, half-cells with sodium metal counter and reference electrode are compared with activated carbon (AC) counter and quasi-reference electrode (QRE) containing half-cells. Such QREs have been reported as suitable alternative reference electrodes in several electrochemical systems.^[42,44,138–141] Additionally, AC has been successfully used as a counter electrode showing a stable behavior, depending on the containing surface groups.^[142–144] The advantage of AC is the solely surface controlled charge storage mechanism. The charge is electrostatically stored in a double layer, which is formed at the AC surface.^[145,146] No electrochemical reactions are taking place to store charge, which leads to a decreased reactivity as compared to sodium metal. Li₄Ti₅O₁₂ (LTO) was selected as a suitable model material to evaluate the impact of Na metal on the electrolyte. LTO possesses a high intercalation potential at about 0.9 V vs. Na/Na⁺ and a high stability during cycling.^[20,70] Furthermore, the intercalation mechanism and the crystal structure transformation of Na-ion insertion into LTO are well investigated.^[18,33,70,147] In this thesis, it will be demonstrated that sodium metal spontaneously reacts with organic carbonate electrolytes forming detrimental decomposition products, which influence the electrochemical performance.

Intercalation materials like Li₄Ti₅O₁₂^[56,70] are well known for their high reversibility as the structural integrity is predominantly kept during sodiation and de-sodiation.^[8,71] Still, a huge drawback is the low capacity originating from the intercalation mechanism.^[55] Therefore, alloy

and conversion type materials are described as prominent alternatives in the state-of-the-art literature.^[55,67] These materials cannot be evaluated versus AC by reason of the limited capacity of AC and a lacking Na⁺ source: during sodiation of a Faradaic material versus AC, Na-ions from the electrolyte are consumed. Simultaneously, the counter-ions (e.g. ClO₄⁻) form a double-layer on the AC surface to provide a charge balance. In the case of low capacity materials like LTO, the electrolyte properties (e.g., ionic conductivity or viscosity of the electrolyte) are rarely affected. A minimum amount of charge is consumed from the electrolyte and the processes are relatively reversible. However, high capacity alloy or conversion-type materials consume much more charge, especially during the first sodiation. The high irreversibility of the first cycle can effectively change the electrolyte properties and distort the results as AC cannot provide Na⁺. Additionally, AC is not suitable for the characterization of high capacity materials due to its low capacity, which is limited by the surface of AC. Furthermore, the application of AC as reference electrode can lead to a reference electrode potential shift over time depending on the electrolyte.^[42,138] Mechanistic studies and long term cycling experiments require a stable reference electrode. Consequently, sodium metal best meets the requirements of a counter and reference electrode and has to be stabilized inside the electrolyte. Liu *et al.*^[129] reported that the use of ether-based electrolytes like bis(2-methoxyethyl) ether (diglyme) leads to low polarization of Na. Another research study of Han *et al.*^[148] uncovers a stabilization of Na deposition during cycling by addition of FEC to carbonate-based electrolytes. Nevertheless, these studies did not assess the reactivity of Na metal depending on the electrolyte solvent. Electrolyte examination in state-of-the-art literature is mainly focused on the analysis and the interplay between the electrolyte and different active materials.^[8,40,90,93,125,126,149] The interaction of the electrolyte with the sodium-metal counter or reference electrode usually remains neglected and no analysis of the sodium metal is given.^[149] This work evidences a stabilization of the sodium metal in diglyme-based electrolytes as well as by addition of FEC to carbonate-based electrolytes.

State-of-the-art literature does not give access to the interactions of electrolyte solvents with both, the working electrode and the sodium counter electrode. Yet, there are reports about the beneficial effects of diglyme and FEC in electrochemical cells. A study by Li *et al.*^[127] reveals that different anode materials, for example, anatase TiO₂ or Sn, show superior Na⁺ storage performance in ether-based electrolytes like diglyme when compared to carbonates. The authors demonstrate that diglyme can facilitate sodiation-induced structural transitions of the TiO₂ and Sn when cycled versus Na metal. Furthermore, it enhances the charge transfer across the electrolyte/electrode interface due to the unique chemistry of the SEI layer induced by diglyme.^[83]

Therefore, diglyme is considered as a promising alternative to carbonate-based electrolytes in the state-of-the-art literature.^[127–129]

On the contrary to the results of Li *et al.*^[127], Brehm *et al.*^[31] found that Antimony shows very poor stability in the diglyme-based electrolyte when compared to FEC containing carbonate-based electrolytes used in the literature.^[36,38,40,59] The underlying causes were not described by the authors and will thus be illuminated in this thesis (section 5.3). There are conflicting opinions on whether diglyme is advantageous or not. Especially the high toxicity of diglyme is an issue which always has to be considered.

In section 5.3, Sb₂O₃ was chosen, as a model to investigate the underlying impact relationships of diglyme and FEC additive with the active material. The conversion-alloy based charge storage mechanism of Sb₂O₃ was previously uncovered by Hu *et al.*^[83] The underlying mechanism is based on several phase transitions, which offers a complex system for the evaluation of the interaction between the electrolyte and the active material. This thesis delivers an explanation of the poor behavior of Sb₂O₃ in diglyme containing NIBs and gives insights into the interaction and stabilization effects of electrolytes with Sb-based electrodes triggered by FEC. Carbonate-based electrolytes with the addition of FEC best meet the requirements to characterize Sb-based electrodes.

The first part of this thesis creates a basis for the analysis of high capacity materials by comprehensive investigations of reactivity factors and further tailoring of the electrochemical system. The applied Sb₂O₃ conversion material delivers high capacities but the occurrence of several phases leads to complex electrochemical behavior and an obstruction for commercial application. Alternatively, a class of promising high capacity materials which can form Na-rich compounds through an alloying reaction was proposed in the literature.^[16,28–31]

Antimony is a very common alloy material, which reacts with sodium to Na₃Sb with a theoretical capacity of 660 mAh g⁻¹.^[40] Still, this material suffers from high volume change (~300 %)^[29,35,40] slow reaction kinetics during the Na⁺-ion insertion and extraction process, and the capacity is fading.^[35,150] Two approaches to counteract volume changes were addressed in this section 2.2.2: nano-structuring of the active material and the application of carbon as a buffering matrix. The latter is widely discussed for antimony-based electrodes in state-of-the-art literature where several different carbon materials in various concentrations have been proposed.^[35,36,38,40,93,151] Table 1 gives an overview of different NIB systems with Sb/C composite electrodes. A key issue is the low comparability of electrode design operated in various electrochemical systems utilized by the different authors. For example, a discrepancy in the work of Qian *et al.*^[93] was highlighted by Darwiche *et al.*^[40] for bulk Sb. Qian *et al.*^[93] reported that

bulk Sb (100 mesh = 149 μm) in an electrode composition of 80 % (w/w) Sb, 10 % (w/w) SuperP, and 10 % (w/w) carboxymethyl cellulose (CMC) do not show comparable stability to their corresponding Sb/C composite. The bulk Sb electrode degraded during the initial cycles, whereas a nanocomposite of Sb and acetylene black obtained from a mechanical ball milling process could reach a capacity of 610 mAh g^{-1} normalized to the Sb amount. The work of Darwiche *et al.*^[40] revealed that bulk Sb (325 mesh = 44 μm) could exhibit similar stability as nanosized Sb. They presented a bulk Sb electrode combined with a conductive additive of vapor-grown carbon fibers (VGCF) and carbon black. An electrode composition of 70 % (w/w) Sb, 15 % (w/w) carbon black/carbon fibers, and 15 % (w/w) CMC was able to deliver a stable capacity of about 550 mAh g^{-1} over 160 cycles. This example again emphasizes that incomparable systems are still compared in the literature. To complicate matters, it is often not stated if the added conductive additive is included in the normalization.^[36,40,152] Since the capacity of SuperP is reported to exceed 150 mAh g^{-1} for NIBs,^[37,93] one must include the carbon additive to the normalization. This does not only underline the differences between the electrodes and electrochemical systems but also the different ways of normalization and therefore the incomparability of the results. Therefore, ideal conditions for comparability are ensured in section 6.1 by first adjusting the electrode composition, electrolyte, and way of normalization.

A further study was performed by Ramireddy *et al.*,^[153] which focuses on the amount of carbon and Sb particle size. Different ratios of Sb and graphite were ball milled, and the resulting composites were combined in an electrode with SuperP and CMC with the overall composition of 80 % (w/w) Sb/C, 10 % (w/w) SuperP, and 10 % (w/w) CMC. The authors concluded that a high amount of carbon with a small particle size (ca. 1 nm) leads to the highest cycling stability. However, a loss of energy density needs to be tolerated when enhancing the amount of graphite.^[153] The authors identified important correlations between the electrochemical performance and the (initial) Sb size, but yet a systematic investigation focusing on the properties of the applied carbon is in high demand.

Especially the main properties of the carbon as a conductive additive, buffering matrix, or element with synergetic added-value cannot be evaluated by comparison of the current literature. Section 6.2 presents a guideline for choosing the right carbon additive for Sb/C composite electrodes in NIBs. The focus is on the examination of carbon characteristics and their influence on the electrochemical performance. By using six different carbons with a fixed amount of 20 % (w/w) C, 70 % (w/w) Sb and 10 % (w/w) CMC, it is demonstrated that the properties of

the carbon are of essential importance. By variation of different carbon additives, the electrochemical performance and the SEI of synthesized Sb nanopowder based electrodes were adjusted.

Moreover, section 6.3 addresses the question if the obtained results are comparable when varying the Sb powder. Therefore, commercial Sb powder was combined with commercial carbon C65 in various ways and compared to the obtained results with synthesized Sb nanopowder. The data indicates that a comparison of published literature, as presented in the work of Darwiche *et al.*^[40] disagreeing with the study of Qian *et al.*^[93], should not be given without particular caution to the applied Sb materials. In this thesis, it is revealed that electrodes consisting of different Sb powders are incomparable by reason of the particle size, which highly influences the electrochemical performance. An individual adjustment of the Sb morphology and particle size, carbon properties and carbon amount is crucial for the best possible electrochemical performance.

Table 1. Summary of different parameters of Sb/C composites in the state-of-the-art literature. Not available data from the literature references are donated as “n.a.”. AB: Acetylene black; MWCNTs: Multi-walled carbon nanotubes; PAN: Polyacrylonitrile. *not mentioned if the conductive additive is included to the normalization.

Reference	Potential vs. Na/Na ⁺ / V	C type	C amount in Sb/C / %	Preparation of Sb/C	Total electrode composition	Electrolyte	Normaliza-tion	Capacity/ mAh g ⁻¹ at 100 mA g ⁻¹
Cui <i>et al.</i> ^[36]	0 – 2.5	cross-linked C	56	wet synthesis of Sb/C (from Sb-acetate precursor)	35 % Sb, 45 % C, 10 % AB, 10 % PVDF	1 M NaPF ₆ in EC/DMC	Total mass of Sb and C*	~630
Darwiche <i>et al.</i> ^[40]	0 – 2	C fibers and carbon black	15	mixing in a ball mill (all electrode components)	70 % Sb, 15 % C, 15 % CMC	1 M NaClO ₄ in PC + 5 % FEC	n.a.	~580
Hou <i>et al.</i> ^[152]	0.01 – 2	AB	29	co-precipitation of Sb on C (SbCl ₃ and NaBH ₄)	49 % Sb, 21 % C, 15 % SuperP, 15 % CMC	1 M NaClO ₄ in PC + 5 % FEC	Total mass of Sb and C	~500
Qian <i>et al.</i> ^[93]	0 – 2	SuperP	30	dry ball milling of Sb and C under Ar	56 % Sb, 24 % C, 10 % SuperP, 10 % CMC	1 M NaPF ₆ in EC/DEC + 5 % FEC	Sb	~600
Wu <i>et al.</i> ^[37]	0.01 – 2	C-nanofibers	62	single-nozzle electrospinning (PAN and SbCl ₃)	27 % Sb, 43 % C, 20 % SuperP, 10 % PAA	1 M NaPF ₆ in EC/DEC + 5 % FEC	Sb/C + SuperP	~500
Zhou <i>et al.</i> ^[151]	0 – 2	MWCNTs	22	wet ball milling of Sb and C in acetone	62 % Sb, 18 % C, 10 SuperP, 10 % CMC	1 M NaClO ₄ in EC/PC + 5 % FEC	Sb/C without SuperP	~500
Zhu <i>et al.</i> ^[38]	0 – 2	C-fibers	46	electrospinning (PAN and SbCl ₃)	54 % Sb, 46 % C	1 M NaClO ₄ in EC/DMC	Sb	~400

4 Experimental

4.1 Preparation of materials and electrolytes

4.1.1 Chemicals

The following chemicals were obtained from Sigma Aldrich:

Propylene carbonate (PC, 99.7 %), ethylene carbonate (EC, ≥ 99 %) dimethyl carbonate (DMC, ≥ 99 %), fluoroethylene carbonate (FEC, 99 %), bis(2-methoxyethyl) ether (diglyme, anhydrous, 99.5 %), lithium titanate (LTO, type: lithium titanate, spinel, nanopowder), polytetrafluoroethylene (PTFE, 60 % (w/w) solution in water), dimethyl sulfoxide (DMSO, ≥ 99.5 %), sodium borohydride (NaBH_4), antimony chloride (SbCl_3 , Sigma Andrich), carboxymethyl cellulose (CMC, DS = 0.7, Mw = 250 000), Antimony oxide (Sb_2O_3 , nanopowder, < 250 nm particle size (TEM), ≥ 99.9 % trace metals basis).

The following chemicals were obtained from Alfa Aesar:

Na metal (99.95 %), sodium perchlorate (NaClO_4 , > 99 %), sodium hexafluorophosphate (NaPF_6 , > 99 %), Antimony powder (Sb-com, 200 mesh, 99.999 % metals basis)

The following carbons were obtained from Imerys Graphite & Carbon:

Carbon black C-ENERGY C65 (C65), SuperP carbon black (SuperP), KS6L graphite (KS6L).

Activated carbon (AC) powder was obtained from HayCarb PLC. Graphene nanostars (Nanostars) were received from Graphene Supermarket. A nanodiamond powder was purchased from NaBond.

4.1.2 Synthesis routes

The synthesis of Sb nanopowder was previously described elsewhere.^[152] For this work, the parameters given in literature were optimized by using an excess of sodium borohydride as a reducing agent. 1.216 g NaBH_4 was dissolved in 400 mL ethanol (EtOH) in a beaker. 2.244 g antimony chloride dissolved in 100 mL EtOH was added dropwise to the NaBH_4 solution under stirring at room temperature. The resultant black mixture was reacted for another hour and afterwards sonicated for ten minutes. The Sb particles were filtered under vacuum and washed with EtOH and water. Thereafter, the black powder was dried at 80 °C for 4 h. The synthesized Sb powder will be referred to as Sb in section 6.1 and 6.2 and Sb-syn in section 6.3.

The OLCs were synthesized by annealing high-purity detonation nanodiamond powder either in an inert atmosphere (argon) at 1700 °C (OLC1700A) or in vacuum at 1300 °C (OLC1300V).^[120]

Commercial antimony powder (Sb-com) was milled for 15 h in a pulverisette 7 by Fritsch (Germany) with five minutes break after every 15 minutes of milling. The obtained powder will be referred to as Sb-com mill. The same procedure was conducted with mixtures of 90 % (w/w) commercial Sb + 10 % (w/w) of C65 conductive carbon and 70 % (w/w) commercial Sb + 30 % (w/w) of C65, respectively. The Sb/C composites will be labelled Sb-com/10C65 mill and Sb-com/30C65 mill.

4.1.3 Electrolytes

The preparation and handling of the solvents and salts were conducted in an argon-filled glove-box (MBraun, O₂, H₂O < 0.5 ppm). The sodium salt was dried under vacuum at 80 °C for 48 h. 1 mol of sodium salt was dissolved in the respective solvents. The EC and DMC mixture was prepared in a ratio of EC:DMC = 50:50 (by weight). All prepared electrolyte solutions were examined via Karl-Fischer titration and were found to contain less than 25 ppm water. All details of the applied electrolyte solutions are specified in Table 2.

Table 2. Overview of all applied electrolytes with the labelling corresponding to the respective section.

Section	Salt	Solvent	Labelling
5.1.1 – 5.1.5	1 M NaPF ₆	EC:DMC (50:50)	E-NaPF ₆
5.1.1 – 5.1.5	1 M NaClO ₄	PC	P-NaClO ₄
5.1.1 – 5.1.5, 5.2, 5.3	1 M NaClO ₄	EC/DMC (50:50)	E-NaClO ₄ (5.1.1 – 5.1.5), E (5.2, 5.3)
5.2, 5.3	1 M NaClO ₄	Diglyme	D
5.2, 5.3, 6	1 M NaClO ₄	EC/DMC (50:50) + 5 % FEC	F

4.2 Optical methods

4.2.1 Visual analysis

For visual analysis of the Na reactivity, 0.25 g Na metal pieces were thoroughly cleaned by scraping the surface layer of the metal with a scalpel in an argon-filled glovebox to avoid any impurities of the metal. These shiny metal pieces were added to 5 mL of each of the electrolytes listed in Table 2 and kept in Al-bottles to avoid side reactions of NaPF_6 with glass. For a before and after comparison, 5 mL of E- NaClO_4 were filled in a glass bottle and pictures were recorded right after the addition of the Na metal. After three days, the components were transferred from Al-bottles into glass bottles and pictures were taken.

4.2.2 Time-resolved light microscopy

The microscopy cell consists of a polyethylene (PE) film, an O-ring, and borosilicate glass, which were clamped between two metal plates to seal the cell. The upper metal plate is perforated to enable optical microscopy through the underlying borosilicate window. The sodium metal was pressed onto the polyethylene film and the cell was filled with the electrolyte E- NaClO_4 inside of an argon-filled glove box. Bright-field imaging with an Olympus BXFM microscope at 10x magnification was performed. To increase the depth of field, focus stacks consisting of 25 single charge-coupled device (CCD) images with 8 μm distance between the focal planes were taken. During the experiment, images were recorded every 15 min.

4.3 Electrochemical analysis

4.3.1 Electrode preparation

When using sodium metal as a counter and a reference electrode, great importance was paid to the preparation as proposed in Ref. [137]. The oxide layer was removed thoroughly with particular care to obtain a smooth Na metal surface and to avoid inhomogeneity and impurities. The counter electrodes were pressed to a uniform thickness of 1 mm. 12 mm Na-metal discs were subsequently punched out.

For the preparation of the counter and QRE applied in sections 5.1.2 – 5.1.4, AC was mixed with isopropanol in a DAC150.1 FVZ speed mixer. For the transformation to a paste, 10 % (w/w) (dry mass) of dissolved PTFE was added to the mixture and speed-mixed at 800 rpm for 5 min. The utilization of PTFE binder has the advantage to obtain a highly oversized AC electrode avoiding electrode cracking. To obtain a viscous consistency, the paste was kneaded manually on a glass plate. It was then placed between two PE foils and manually rolled to a thickness of 1 ± 0.25 mm. Discs with 12 mm diameter were punched out after drying for 12 h in an ambient atmosphere. The mass of the CE was typically 100 ± 5 mg cm⁻². The remaining parts were kept and used as QRE. The electrodes were transferred to a vacuum oven inside an Ar-filled glovebox and dried at 120 °C for 24 h under vacuum. The initial potential difference between the used HayCarb AC QRE and metallic sodium was determined to be 2.6 V.

Working electrodes were prepared by mixing the respective components in a DAC150.1 FVZ speed-mixer from Hauschild. Specific information about the electrodes' ingredients, ratios, etc. are listed in Table 3. The active material and conductive carbon were first dry mixed at 1000 rpm for 5 min in the corresponding ratio. Then, the respective solvent was added to obtain a viscous paste. This paste was again mixed at 1500 rpm for 10 min following 2500 rpm for 10 min before adding the binder solution (either 10 % (w/w) PVdF dissolved in DMSO or 3 % (w/w) CMC dissolved in water and EtOH (50:50 weight ratio)). The last mixing step was conducted at 800 rpm for 10 min. Pure carbon (C) working electrodes applied in 6.2 were obtained with a ratio of 90 % (w/w) C and 10 % (w/w) CMC following the previously described mixing steps. The slurries were doctor bladed on an aluminum foil with a gap size of 150 μm and dried for three days at ambient conditions. Subsequently, the electrodes were punched out with 12 mm diameter and transferred into a vacuum oven inside an Ar-filled glovebox. Finally, a vacuum drying step at 120 °C for 12 h was conducted.

Table 3. Ingredients and compositions of all applied electrodes and the corresponding sections. The compositions are referred to the dry electrode mass.

Section	Active material (AM)	Binder (B)	Solvent (S)	Carbon additive (CA)	Composition (AM:CA:B)	mass loading/thickness
5.1.2 – 5.1.4	LTO	PVdF	DMSO	C65	80:10:10	$3\pm 1 \text{ mg cm}^{-2}$ / $25 \mu\text{m}$
5.3	Sb_2O_3	CMC	EtOH:H ₂ O (50:50)	C65	70:20:10	$3\pm 1 \text{ mg cm}^{-2}$ / $30 - 40 \mu\text{m}$
6.1	Sb	CMC	EtOH:H ₂ O (50:50)	C65	85:5:10/ 80:10:10/ 75:15:10/ 70:20:10/ 40:50:10	$4\pm 2 \text{ mg cm}^{-2}$ / $30 - 40 \mu\text{m}$
6.2 – 6.3	Sb = Sb-syn	CMC	EtOH:H ₂ O (50:50)	C65/ SuperP/ KS6L/ OLC1300V/ OLC1700A/ Nanostars	70:20:10	$3\pm 1 \text{ mg cm}^{-2}$ / $30 - 40 \mu\text{m}$
6.3	Sb-com	CMC	EtOH:H ₂ O (50:50)	C65	70:20:10	$4\pm 1 \text{ mg cm}^{-2}$ / $40 \mu\text{m}$
6.3	Sb-com mill	CMC	EtOH:H ₂ O (50:50)	C65	70:20:10	$3\pm 1 \text{ mg cm}^{-2}$ / $30 - 35 \mu\text{m}$
6.3	Sb-com/10C65 mill	CMC	EtOH:H ₂ O (50:50)	C65	78:12:10	$3\pm 1 \text{ mg cm}^{-2}$ / $30 - 35 \mu\text{m}$
6.3, 8	Sb-com/30C65 mill	CMC	EtOH:H ₂ O (50:50)	C65	80:10:10	$3\pm 1 \text{ mg cm}^{-2}$ / $30 - 35 \mu\text{m}$

4.3.2 Cell preparation

Custom-built polyether ether ketone (PEEK) cells with spring-loaded titanium pistons as a three-electrode system were used for electrochemical testing as described in Ref. [154]. After drying all cell parts at 120 °C, the cells were assembled inside an Ar-filled glovebox. 12 mm diameter sodium disc counter electrodes and the working electrodes were separated by a 13 mm diameter vacuum dried glass-fiber disc (Whatman GF/D). Cells that were cycled for X-ray photoelectron spectroscopy (XPS) and scanning electron microscopy (SEM) analysis were additionally separated by a cellulose separator (Nippon Kodoshi). This separator was placed on top of the working electrode to avoid the adhesion of glass fibers on the surface. A copper foil current collector was placed on the backside of each counter electrode. The Na-reference was placed on a compressed glass fiber separator (GF/D, from Whatman) in a cavity close to the working electrode/counter electrode stack and contacted by a titanium screw. The cells were vacuum filled with the respective electrolyte (Table 2).

Two different half-cell set-ups were used in section 5.1 to characterize the LTO working electrodes: I) sodium metal reference electrode and a 12 mm diameter sodium disc as counter electrode and II) AC as QRE and a 12 mm diameter AC disc as counter electrode. The cells are referred to as L/Na (I) and L/AC (II).

4.3.3 Electrochemical characterization

Electrochemical measurements were carried out in a climate chamber at 25 °C using a VMP3 multi-channel potentiostat/galvanostat (Bio-logic Science Instrument, France), equipped with the EC-Lab® software.

Galvanostatic charge/discharge cycling with potential limitation (GCPL) experiments in section 5.1 were performed in a voltage window of 0.1 – 2.2 V vs. Na/Na⁺ and -2.5 – -0.4 V vs. carbon with a charge/discharge current of 50 mA g⁻¹. Three different electrolytes were applied, respectively (Table 2). The cycling stability measurements were stopped after 100 cycles. Cells which were prepared for X-ray diffraction (XRD) analysis were stopped after 50 cycles in the de-sodiated state and for XPS analysis after 20 cycles in the sodiated state.

For the determination of the AC QRE stability, cyclic voltammetry (CV) was performed with a scan rate of 0.25 mV s⁻¹ from -0.2 to -2.5 V vs. carbon. CVs were recorded every 24 hours. The half-wave potential was determined from the obtained data and plotted versus time.

For GCPL experiments demonstrated in section 5.3, the Sb_2O_3 -based cells were cycled in three different electrolyte solutions (Table 2) in a voltage window of 0.1 – 2.0 V vs. Na/Na^+ with a charge/discharge current of 200 mA g^{-1} . The cycling stability measurements were stopped after 100 cycles. Cells that were prepared for XPS and SEM analysis were stopped after 50 cycles in the de-sodiated state.

All capacity values stated in section 5.1 and 5.3 are given with respect to the active material mass.

In section 6, GCPL experiments were performed in a voltage window of 0.1 – 2.0 V vs. Na/Na^+ using 1M NaClO_4 in EC/DMC + 5 % FEC (F) electrolyte (Table 2) with a charge/discharge current of 200 mA g^{-1} . The cycling stability measurements were stopped after 100 cycles. Cells that were prepared for XPS and SEM analysis were stopped after 50 cycles in the de-sodiated state. Half-cell rate capability measurements (section 6.2.2) were conducted with the same electrolyte at currents between 100 mA g^{-1} and 8 A g^{-1} (same rates for charge and discharge). A comparison between two ways of normalization is presented in section 6.1. Following that, all capacity values given in sections 6.2 and 6.3 were indicated with respect to the total mass of the active material + carbon additive.

4.4 Electrodes and materials characterization techniques

4.4.1 X-ray diffraction

X-ray diffraction (XRD) measurements of the Sb_2O_3 powder (section 5.3.1), synthesized Sb powder (section 6.1.1) and commercial Sb powder samples (section 6.3.1) were performed with a STOE STADI P diffractometer (Mo- $\text{K}\alpha$ -radiation, $\lambda = 0.7093 \text{ \AA}$) in rotating capillary transmission mode. For phase identification, the ICSD database was utilized.

Ex-situ X-ray diffraction (XRD) measurements of cycled LTO electrodes (section 5.1.3) were performed with a STOE STADI P diffractometer (Cu- $\text{K}\alpha 1$ -radiation, $\lambda = 1.5406 \text{ \AA}$) in flat-sample transmission mode. For phase identification, the ICSD database was utilized.

L/Na and L/AC cells, soaked in E- NaClO_4 , were polarized to 2.2 V vs. Na/Na^+ after 100 cycles. The potential was held for 2 h to obtain full de-sodiation. Afterwards, the cells were disassembled in air and the electrodes were washed with DMC to remove the remaining salt. The electrode coating was carefully removed from the aluminum foil of the cycled cells electrodes and from a pristine electrode, respectively. The obtained electrodes without current collector were characterized by XRD.

4.4.2 X-ray photoelectron spectroscopy

The samples for X-ray photoelectron spectroscopy (XPS) analysis in section 5.1.4 were prepared as follows: L/AC and L/Na cells filled with E- NaClO_4 , P- NaClO_4 and E- NaPF_6 were charged-discharged 20 times and stopped in the sodiated state at 0.1 V vs. Na/Na^+ and -2.5 V vs. carbon. The potential was held for 2 h. The cells were then transferred to an Ar-filled glovebox for disassembly. The LTO electrodes were removed and rinsed with DMC prior to XPS measurements.

For the *ex-situ* XPS analysis in section 5.3.3, the Sb_2O_3 -based electrodes were charged-discharged 50 times in each electrolyte solution and stopped in the de-sodiated state at 2.0 V vs. Na/Na^+ . The potential was held for 2 h. The cells were then transferred to an Ar-filled glovebox for disassembly. The working electrodes were removed and rinsed with DMC or diglyme prior to XPS measurements.

To perform an XPS analysis in section 6.2.2, the Sb/C composite electrodes were charged-discharged 50 times and stopped in the de-sodiated state at 2.0 V vs. Na/Na^+ . The potential was

held for 2 h. The cells were then transferred to an Ar-filled glovebox for disassembly. The electrodes were removed and rinsed with DMC prior to XPS measurements.

X-ray photoemission measurements were performed using a K-alpha XPS spectrometer from Thermo Fisher Scientific (East Grinstead). The samples were illuminated with monochromatic Al-K α X-rays with a spot size of about 400 μm . The photoelectrons were detected with a hemispherical 180 dual focus analyzer with 128 channel detectors. To prevent any localized charge buildup, the K-Alpha charge compensation system was employed during analysis, using electrons of 8 eV energy and low-energy argon ions. The Thermo Avantage software was used for data acquisition and processing.^[155] The spectra were fitted with one or more Voigt profiles (binding energy uncertainty: ± 0.2 eV). All spectra were referenced to the C 1s peak of hydrocarbon at 285.0 eV binding energy controlled by means of the well-known photoelectron peaks of metallic Cu, Ag, and Au.

4.4.3 Scanning electron microscopy and energy-dispersive spectroscopy

Scanning electron microscopy (SEM) and energy-dispersive X-ray spectroscopy (EDS) measurements were conducted by a thermal field emission scanning electron microscope (FESEM, Carl Zeiss SMT AG) equipped with energy-dispersive spectroscopy (EDS, Quantax 400 SDD, Bruker) at an acceleration voltage of 10 kV. The samples were fixed on a steel sample holder by using carbon sticky tape.

The Sb₂O₃ powder (section 5.3.1), the synthesized Sb powder (section 6.1.1) and the commercial Sb powder (section 6.3.1) samples were sputtered with a 5 nm thick gold/palladium layer.

For SEM and EDS analyzes performed in section 5.3.3, 5.3.4 and 6.2.2, the electrodes were charged-discharged 50 times and stopped in the de-sodiated state at 2.0 V vs. Na/Na⁺. The potential was held for 2 h. The cells were then transferred to an Ar-filled glovebox for disassembly. The working electrodes were removed and rinsed with DMC or diglyme prior to SEM/EDS measurements. The sodium metal counter electrode was characterized without subsequent rinsing to avoid the removal of soluble Sb-containing species. The samples were constantly kept in an inert gas atmosphere also while transferring.

4.4.4 Other techniques

To examine the Sb content in the cycled electrolyte applied in section 5.3.4, the electrolyte was first extracted from the cell. The Sb content was then determined by inductively coupled plasma mass spectrometry (ICP-MS).

The following techniques were solely applied for materials characterization in section 6.2:

Raman spectra of the carbons described in section 6.2.1 were recorded with a Renishaw in Via Raman Microscope equipped with a Nd-YAG laser with an excitation wavelength of 532 nm and a power of 0.05 mW at the surface of the sample, using an objective lens with a numeric aperture of 0.75. Ten different spots from each of the samples were recorded with 5 accumulations and 30 s acquisition time. All spectra were normalized to 100 %, and fitting of the carbon signal was achieved assuming Voigt peak profiles for the D-mode and G-mode.

Nitrogen gas sorption analysis (GSA) for the respective carbons was conducted to obtain a specific surface area (SSA), and pore volume of the samples (section 6.2.1). We carried out the measurements with a Quantachrome iQ system using nitrogen gas at -196 °C. Prior to the measurements, the powder samples were degassed at 250 °C and 102 Pa for 12 h. The SSA was calculated using the Brunauer-Emmett-Teller (BET) equation in the linear pressure range and the quenched solid density functional theory (QSDFT) by assuming slit-shaped pores with the ASiQwin-software. The values for the total pore volume were obtained at a relative pressure of $P/P_0=0.95$.

Transmission electron microscopy (TEM) of the carbons were carried out by using a JEOL JEM-2100F instrument operated at 200 kV (section 6.2.1). Scanning TEM (STEM) was performed on a probe-corrected FEI Titan Themis 60-300 X-FEG S/TEM instrument operated at 300 kV equipped with an FEI Super-X windowless EDS system with four synchronized silicon drift detectors from Bruker. For all these measurements, the samples were dispersed in isopropanol or ethanol through sonication for 2 min and drop-casted onto a copper grid with a lacey carbon film.

5 The interplay of electrolyte and electrode: reactivity issues and perspectives

In order to probe the electrochemical properties of NIBs, sodium metal is most frequently applied as a reference and/or counter electrode in the state-of-the-art literature. However, the high reactivity of the sodium metal and its impact on the electrochemical performance is usually neglected (section 3). The following study demonstrates the occurrence of spontaneous reactions between sodium metal and organic electrolytes and emphasizes the importance of critical interpretation of electrochemical experiments. To further establish a setup with appropriate components for the characterization of high-capacity materials in NIBs, the sodium metal was stabilized by variation of the electrolyte solvent. Nevertheless, the electrolyte can not only affect the Na metal but also detrimentally interact with the active material. An example of the tremendous influence of the electrolyte solvent on Sb_2O_3 electrodes is elaborated in this section.

5.1 Sodium reactivity

Section 5.1 is extracted from the scientific publication “Can Metallic Sodium Electrodes Affect the Electrochemistry of Sodium - Ion Batteries? Reactivity Issues and Perspectives”.^[56] All contributions are stated in section 12.

5.1.1 Reactivity of sodium towards organic electrolytes

Sodium metal was reported to have an influence on the electrochemical performance of half-cells during cycling.^[22,136] By placing Na metal inside carbonate-based electrolytes as shown in Figure 6 it was possible to visualize clearly that sodium reacts with the different electrolytes, even without electrochemical cycling. The electrolytes will be referred as E- NaClO_4 (1 M NaClO_4 in EC/DMC), E- NaPF_6 (1 M NaPF_6 in EC/DMC) and P- NaClO_4 (1 M NaClO_4 in PC). A more detailed description is given in the experimental section.

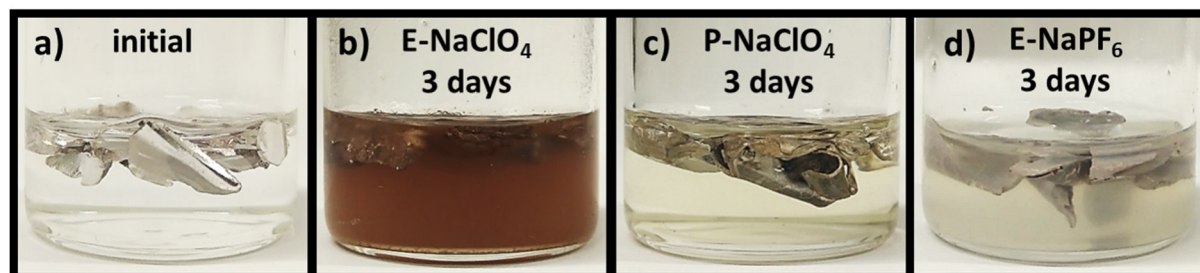


Figure 6. a) Na metal in E- NaClO_4 right after Na addition (representative for all electrolytes), b) Na metal in E- NaClO_4 , c) in P- NaClO_4 and d) in E- NaPF_6 after three days.

Immediately after Na addition, the metal exhibits a shiny metallic surface and the liquid electrolytes are colorless and clear in all cases (Figure 6a). After three days, a difference appears between the considered electrolytes. A massive color change can be observed for E-NaClO₄ in Figure 6b. The clear solution turns to dark-red and turbid after three days. Also in the case of E-NaPF₆ (Figure 6d), the solution turns cloudy but remains colorless. In the case of P-NaClO₄, shown in Figure 6c, the solution turns slightly yellow but remains clear. These changes are likely caused by side-reactions with the electrolyte. The surface of the Na metal has altered in all three samples. From this simple optical examination, it is possible to conclude that spontaneous reactions take place in all electrolytes and that sodium forms decomposition products with the electrolyte.

To obtain a deeper understanding of the processes occurring on the sodium surface, optical microscopy was conducted over time. A sealed microscopy cell with Na metal on a PE film filled with E-NaClO₄ was prepared. To monitor the changes on the metal surface, boundary and the PE film, an area at the edge of the Na metal was chosen for the observation (Figure 7).

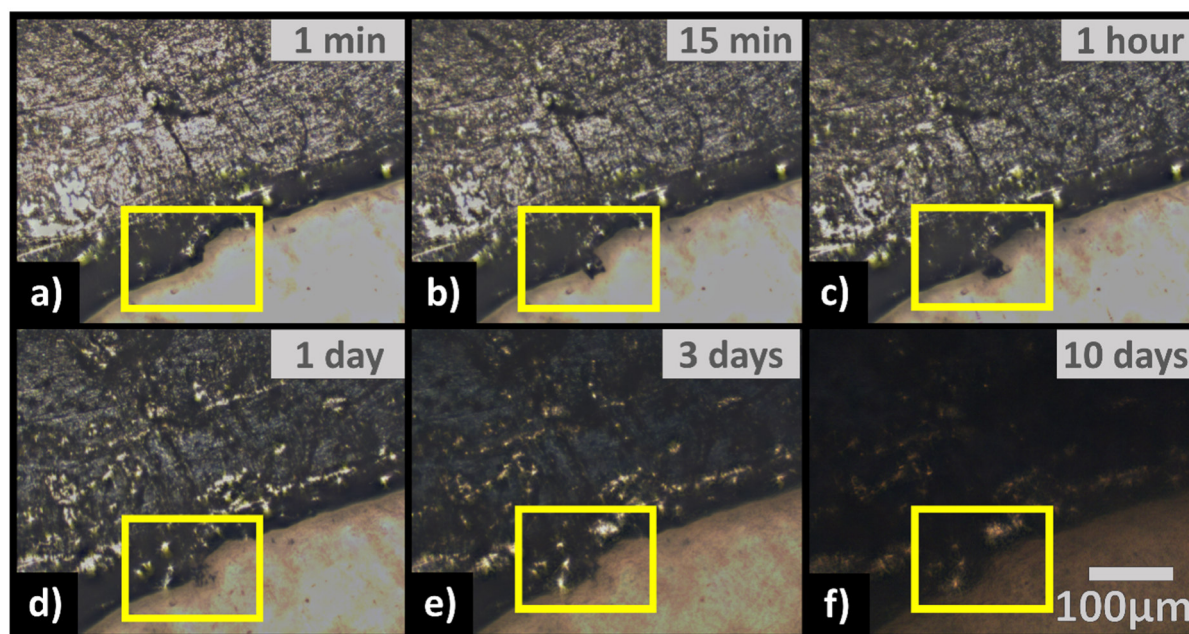


Figure 7. Optical microscopy images of Na metal on a polyethylene film, filled with E-NaClO₄ in a sealed cell. Pictures were recorded after a) 1 min, b) 15 min, c) 1 hour, d) 1 day, e) 3 days and f) 10 days. The yellow highlighted area optically shows a time-resolved reaction on the Na surface.

The transformation process over 10 days is visualized in Figure 7a – f. An outgrowth is formed after only 15 min as can be seen when comparing the highlighted area in Figure 7a and b. With increasing time, this particle shrinks again (highlighted section in Figure 7d). Finally, it entirely vanishes after three days (Figure 7e). According to this study, a conversion of the Na metal

surface over time becomes evident. The shiny and smooth Na-metal surface in Figure 7a turns dark and becomes rougher (Figure 7c – f). We relate these observations to the formation of a solid interphase consisting of degradation products of reactions between Na and the electrolyte. On the contrary, particles of this phase are continuously peeled off and diffuse into the electrolyte. Afterwards, the blank Na surface can further react with the electrolyte. This assumption is supported by the turbid appearance of E-NaClO₄ and E-NaPF₆ (Figure 6) and the decrease of the image intensity during optical microscopy (Figure 7c – f). Both effects are likely caused by the interaction of light with the particles in the electrolyte. As PE does not react with the electrolyte, the reduced intensity must be caused by a cloudier electrolyte because the image cannot just become darker due to rougher surface or color change.

These findings raise serious doubts on the use of Na metal for electrochemical investigations. Indeed, even without electrochemical cycling, the high reactivity of sodium metal is demonstrated (Figure 6 and Figure 7). Decomposed species can diffuse inside the electrolyte and can thus interact with the electrochemical system under investigation. Not only instabilities of the passivation layer but also dendrite like changes of the Na surface can lead to short circuits in the cell. Moreover, the side reactions taking place at the Na-electrolyte surface are possibly amplified during electrochemical cycling (i.e., when using the Na-metal as a counter electrode). Such effects likely result in distorted conclusions about the tested materials. However, the three-electrode set-up is still indispensable for the investigation of the single electrodes' behavior.^[43,156] Sensitive techniques like electrochemical impedance spectroscopy require a reliable reference electrode with a stable potential over time.^[157,158] A reactive Na metal RE cannot guarantee this as polarization effects cannot be excluded. Consequently, there is not only a lacking of reliability on the described half-cell measurements but also a transfer of the results to a full cell would not be consistent as already observed in Ref. [136].

5.1.2 The influence of metallic sodium in electrochemical cells

To study the impact of Na-metal in an electrochemical cell, the reactivity of Na-metal towards the electrolyte during cycling has to be considered. Comparing symmetric hard carbon cells with three-electrode cells consisting of a Na counter and reference electrode and a hard carbon working electrode, an unstable behavior of the solid electrolyte interphase (SEI) due to decomposition products was assumed by Imerakova *et al.*^[22] For such an analysis, materials like hard carbon are not optimal as they show a very low intercalation profile below 0.1 V vs. Na/Na⁺.^[72,73] This potential is below the stability window of organic electrolytes and may cause sodium plating and stripping on the electrode surface.^[72,73] Consequently, it cannot be distinguished between degradation products, which occur due to reactions with Na, and the ones that can form due to electrolyte decomposition at low potential. Additionally, sodium plating and stripping may change the surface and the SEI and can cause additional reactions between electrolyte and the plated sodium metal.

Li₄Ti₅O₁₂ was selected as reference material to evaluate the impact of Na metal on the electrolyte. LTO possesses a high intercalation potential at about 0.9 V vs. Na/Na⁺ and high stability during cycling.^[20,70] Furthermore, the intercalation mechanism of Na-ions in LTO is well investigated concerning the change of the crystal structure during cycling.^[18,33,70,147] For this reason, LTO was employed as an exemplary working electrode material. PVdF was used as a binder for the LTO working electrodes as it is one of the most frequently used binders in LIBs and NIBs.^[17,18,21] The LTO-based electrode with a composition described in Table 3 (section 4.3.1) was characterized in two different cell set-ups: one using Na metal as a counter and reference electrode, one using activated carbon as a counter and reference electrode. All electrochemical measurements were conducted using a three-electrode configuration. The cell-set-ups labelling will further be L/Na and L/AC, respectively.

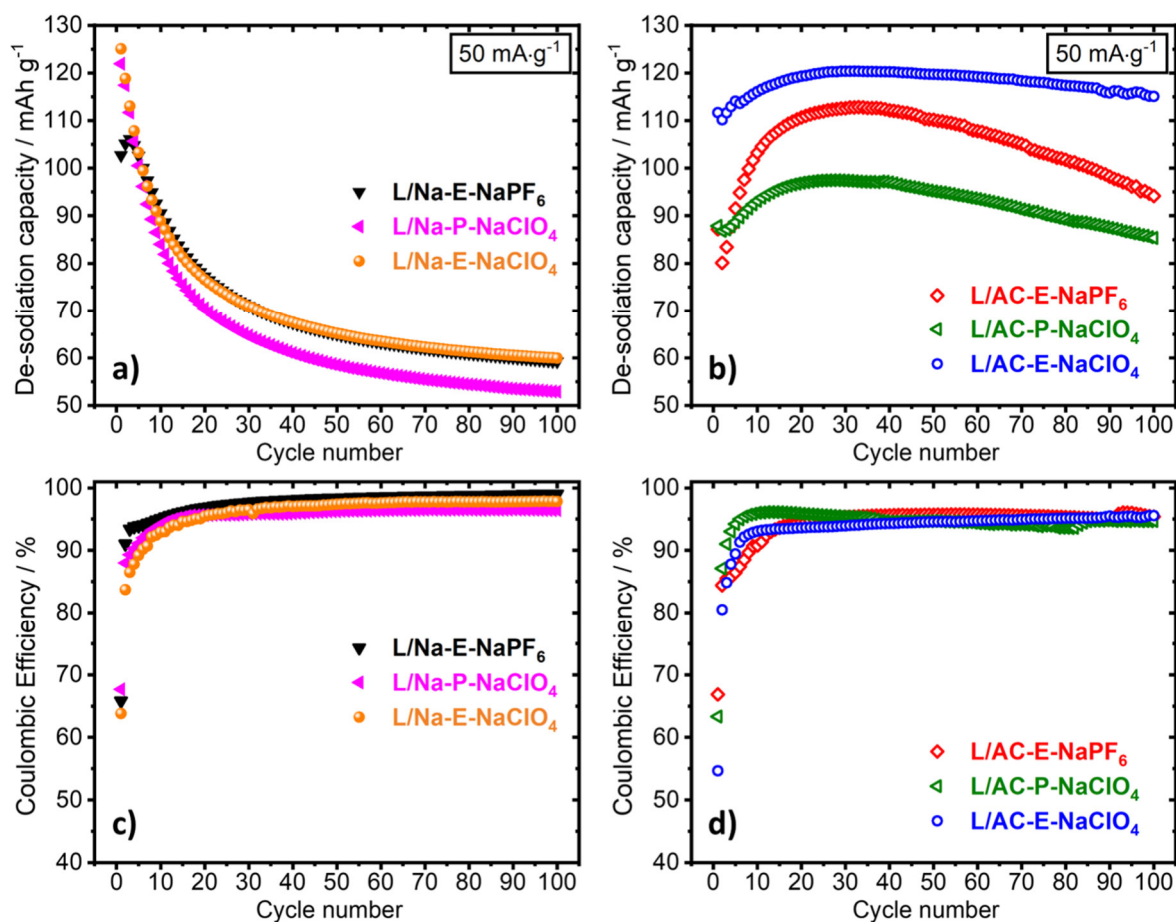


Figure 8. Comparison of L/Na and L/AC cell performance with different organic electrolytes at charging/discharging currents of 50 mA g⁻¹: a) electrochemical cycling stability of L/Na cells, b) electrochemical cycling stability of L/AC cells, c) Coulombic efficiencies of L/Na cells and d) coulombic efficiencies of L/AC cells.

Figure 8a and b demonstrate the difference in cycling stability, comparing both set-ups and using three different electrolytes. All L/Na cells show a rapid capacity loss of more than 35 % during the initial 20 cycles (Figure 8a). The capacity gradually stabilizes, but a continuous decrease can be observed during further cycling. Starting with initial capacities of 105 – 125 mAh g⁻¹, the L/Na cells end up below 60 mAh g⁻¹ after 100 cycles, which is a loss of about 40 – 55 %. On the contrary, the L/AC cells firstly show an increase in capacity during the initial 20 cycles, followed by a stabilization (Figure 8b). After 100 cycles, the capacity retention for these cells is more than 83 % of their maximum capacity. In fact, the L/AC-E-NaClO₄ shows the highest capacity during cycling, combined with the most stable behavior, exhibiting 96 % of its maximum capacity after 100 cycles. These results contradict the conclusions of Sun *et al.*^[70] and Zhao *et al.*^[159]; both solely referred to the rapid capacity loss of similarly composed LTO working electrodes to the reactivity of the used PVdF binder. Their measurements were conducted with the Na metal counter and reference electrodes. The results in this thesis can

confirm the unstable cycling behavior of LTO in a Na-half-cell set-up but clearly show more stable performance when no Na metal is present in the electrochemical set-up.

By further comparing L/Na with L/AC cells, additional insights can be gained. In general, the L/AC cells exhibit strong capacity differences, when comparing the different electrolytes. Thus, without Na metal contact, the different electrolyte properties become apparent. We refer the distinctions of L/AC cells to electrolyte properties like conductivity, viscosity, dielectric constants or differences in the formed SEI.^[15] For cells containing sodium metal, these small electrochemical nuances cannot be illuminated due to the impact caused by the electrolyte contaminations. Additionally, the properties of the electrolyte in Na containing half-cells could have changed due to degradation products. The initial capacity increase of the L/AC cells is related to the known conditioning during the first cycles, which facilitates further sodiation reactions.^[18,20] This effect is not visible for L/Na cells which could be related to the contaminated electrolyte. We cannot give an explicit functional mechanism in the current study, as this would require knowledge of detailed processes, taking place in narrow atomic dimensions close to the counter electrode-electrolyte interface.

The Coulombic efficiencies (CEs) are given in Figure 3c and d, to evaluate the disparities between both cell set-ups. All cells start with CEs below 70 %, reaching 90 % after 10 cycles. Such behavior is attributed to the rearrangement of the LTO crystal structure^[20,160] and side reactions of the cell components leading to SEI formation.^[161–164] In general, the CEs of all cells are relatively similar. L/Na cells reach CEs of more than 96 % (Figure 8c) while L/AC reach 93 – 95 % (Figure 8d). Considering the lower CE of the L/AC cells, the reactivity of the electrolytes towards the AC surface groups should be taken into account. Such surface characteristics of AC counter electrodes might lead to side reactions between the AC surface groups and the electrolyte or undesirable polarization effects.^[142,143,165,166] Therefore, we want to highlight that the chosen AC set-up is not the optimal alternative to the established Na metal set-up. Nonetheless, we observe explicit differences comparing the electrochemical performance of both set-ups. Hence, the reactivity of Na metal towards the electrolyte affects the electrochemical system to a greater extent than when using the AC set-up. Further work is required to uncover the underlying processes of the low CE in order to further improve the electrochemical properties.

In the following, we will demonstrate the impact of degraded species on the working electrode bulk material by *ex situ* XRD analysis and on the electrode surface chemistry by XPS analysis.

5.1.3 Impact of sodium metal reactivity on the bulk material after electrochemical cycling

The electrochemical properties of LTO have been well investigated for lithium-ion intercalation/de-intercalation^[18,33,34] as well as for sodium-ion intercalation/de-intercalation.^[18,20,70,147,167] In the case of Na-ions, Sun *et al.*^[70] predicted a three-phase storage mechanism, $2\text{Li}_4\text{Ti}_5\text{O}_{12} + 6\text{Na}^+ + 6\text{e}^- \rightleftharpoons \text{Li}_7\text{Ti}_5\text{O}_{12} + \text{Na}_6\text{LiTi}_5\text{O}_{12}$, and proved it by *in situ* X-ray diffraction measurements. Additionally, Yu *et al.*^[147] confirmed these findings.

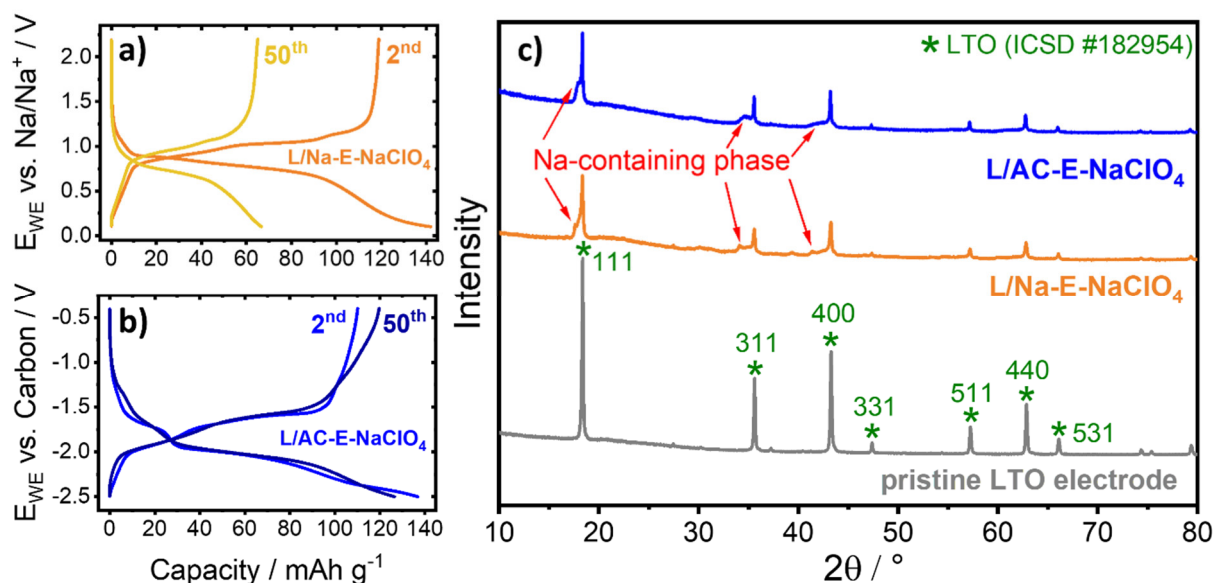


Figure 9. Galvanostatic charge and discharge profiles of the 2nd and 50th cycle for a) L/Na-E-NaClO₄ and b) L/AC-E-NaClO₄; c) XRD patterns of cycled L/AC-E-NaClO₄ and L/Na-E-NaClO₄ electrodes and the respective pristine LTO electrode.

Figure 9a and b illustrate the galvanostatic charge/discharge profiles of the 2nd and 50th cycle for L/Na-E-NaClO₄ and L/AC-E-NaClO₄, respectively. Comparing the sodiation curves of the 2nd and 50th cycle, a difference is evident between 1.2 and 0.9 V vs. Na/Na⁺ (Figure 9a) and between -1.3 and -1.6 V vs. carbon (Figure 4b). This can be attributed to structural rearrangements during initial cycling. Nevertheless, the first sodiation plateau of cycle 50 at -1.6 V vs. carbon is significantly pronounced (Figure 9b). At the same time, this plateau is not apparent for L/Na-E-NaClO₄ cell. As a three-phase mechanism can be indicated by multiple plateaus, we assume that decomposition products result in a hindered Na-ion insertion/extraction causing lower capacities.

To examine if decomposed species have an influence on the active bulk of LTO, we performed XRD measurements of the cycled electrodes. For this purpose, L/Na-E-NaClO₄ and respective L/AC-E-NaClO₄ electrode materials were measured by XRD in the de-sodiated state after 100

cycles and compared to pristine LTO (Figure 9c). Even though the cells were de-sodiated by a subsequent voltage hold after discharging, a small amount of a residual Na-containing phase remained. The diffractograms of cycled LTO both verify the formation of a sodiated structure, indicated by shoulders that are located below the 111, 311 and 400 reflections of LTO.^[70] Moreover, the reflexes of the $\text{Li}_4\text{Ti}_5\text{O}_{12}/\text{Li}_7\text{Ti}_5\text{O}_{12}$ phase can be identified (ICSD #182954). The identical shape of both cycled materials proves that contaminations, which originate from reactions between Na and the electrolyte, do not change the bulk material. Indeed, the structural properties of LTO after cycling are identical for both cell set-ups. Therefore, it seems that solely the surface of the working electrode is affected by side reactions with decomposed electrolyte species and will be analyzed in the following.

5.1.4 Surface analysis after electrochemical cycling

To understand the chemistry of the surface and its correlation to the performance and stability, XPS measurements were conducted on the LTO electrodes of both set-ups for three different electrolytes.

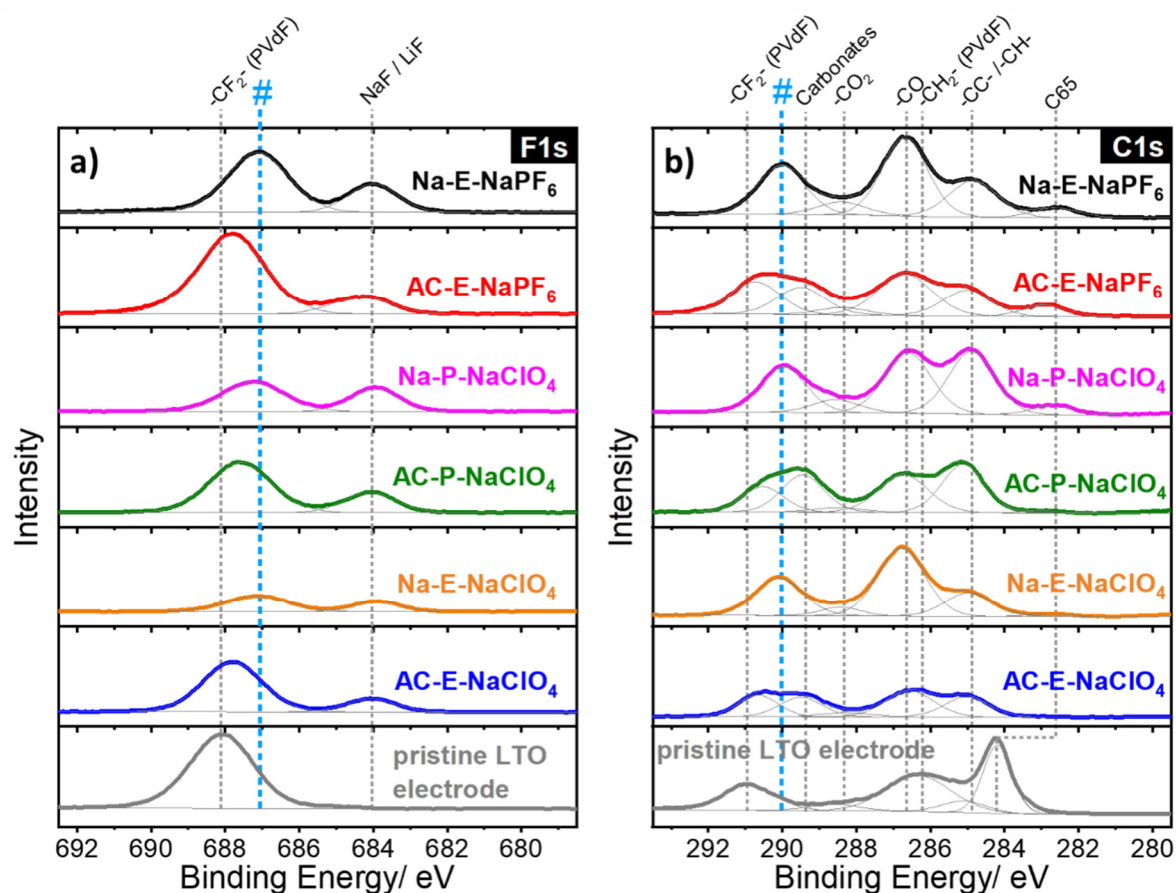


Figure 10. a) F1s and b) C1s spectra of the pristine LTO electrode and all samples after 20 cycles in the sodiated state with proposed assignments.

All spectra are corrected with respect to the peak position at 285.0 eV ($-\text{CH}_2-$)^[6,168] from the pristine LTO electrode sample. The F1s core level in Figure 10a shows that the pristine LTO electrode has a single peak at 688.0 eV that corresponds to the $-\text{CF}_2-$ groups from the PVdF binder.^[6,169] When the LTO electrodes are sodiated, two peaks appear. The signal at 684.0 eV can be assigned to LiF and NaF^[64,170] appearing for all samples at similar binding energies. In contrast, the second peak is shifted when comparing the spectra with regard to the different cell set-ups. In the case of the AC samples, the second signal appears at 687.8 eV whereas for the samples cycled versus Na it is shifted to 687.0 eV and indicated by '#' in Figure 10a. As previously reported by Dhabhi *et al.*^[170], this shift is assigned to a decomposition of the PVdF binder due to de-fluorination. Consequently, if Na metal is used as a counter and reference electrode the decomposition of PVdF is more severe and can affect the cycling stability of the working electrode.

Considering the C1s spectra (Figure 10b) the pristine LTO electrode shows an intense peak at 284.2 eV corresponding to the graphitic parts of the conductive additive. Additionally, there are other peaks at 285.0, 286.3, 288.7 and 291.0 eV which are assigned to $-\text{CH}_2-$, $-\text{CF}_2-\text{C}^*\text{H}_2-$, $\text{O}=\text{C}-\text{O}$ and $-\text{C}^*\text{F}_2-\text{CH}_2-\text{CO}_3-$, respectively.^[6,124,168,169] When comparing the spectra with regard to solely the set-up properties, the sodiated electrodes show very similar spectra for all AC set-ups. The same is observed for the Na set-up independently of the electrolyte. This indicates that the surface layers that form on the LTO electrodes depend more on the type of counter electrode than on the type of electrolyte used. Moreover, the C1s and F1s spectra for all AC samples have a lower intensity than that of the Na samples (Figure 10a and b). This indicates that the surface layer seems thicker for all AC-samples compared to the Na-samples. The most prominent difference in the C1s spectra appears in the region between 289 eV and 291 eV. Two signals are observed for the AC samples at 289.3 eV and 290.7 eV whereas only one is present for all Na samples at 290.0 eV and is marked with '#' in Figure 10b. For the AC samples, the peak at higher binding energy is assigned to the PVdF binder and possibly to organic carbonates. The new signal at around 289.3 eV is most likely present due to Na_2CO_3 or alkyl carbonates $\text{R}-\text{OCO}_2\text{Na}$.^[6,168] At 290.0 eV a signal appears only for the Na samples and cannot be identified. Still, it could be referred to PVdF decomposition as there is no clear signal in the CF_2 region anymore. This assumption fits well to the shifted F1s peak at 687.0 eV (Figure 10a). Therefore, in the case of the Na samples, the binder seems to get more affected by the decomposed electrolyte due to the presence of Na in the half-cell. In general, decomposition products do not only lead to altered electrolyte properties but also affect the working electrode surface that can impair the electrochemical stability.

5.1.5 Conclusive aspects: influence of sodium metal on carbonate-based electrolytes

Sodium metal is highly reactive towards carbonate-based electrolytes even without electrochemical cycling. A decomposition of the sodium surface and the electrolyte takes place very rapidly when placing the Na metal inside different carbonate based solutions. Additionally, significant differences in the electrochemical stability appear when comparing sodium-containing half-cells to sodium-free ones: the presence of sodium metal leads to a fast decrease of the LTO electrode capacity which otherwise remains stable if sodium metal is replaced by activated carbon electrodes. Decomposition products do not influence the crystal structure of the active material but impact the surface chemistry. Such distortions could lead to wrong conclusions of electrochemical experiments and problems in transferring half-cell results to full cells. For this reason, this issue will be further addressed in this study to allow reliable electrochemical characterization of NIB systems.

5.2 Perspective approaches for the sodium metal stabilization in organic electrolytes

In section 5.1, LTO was chosen as a model working electrode to highlight the effect of contaminations which originate from side reactions of Na metal with the electrolyte. Although activated carbon was found to fulfil the requirements as a counter and reference electrode in the applied setup, there will be problems when replacing LTO by high capacity working electrodes. Materials with alloy or conversion type mechanism cannot be evaluated versus AC because of its limited capacity and a missing Na^+ source. To maintain the geometry of the electrochemical cell setup, an excessive oversizing of the AC electrode should be avoided. Furthermore, the electrolyte should not undertake the role of a Na^+ source for high capacity materials. If a high amount of Na-ions is consumed due to irreversible reactions originating from alloy or conversion mechanisms, the electrolyte properties will be altered. Therefore, the counter electrode must provide Na^+ and should not affect the cell geometry. A further issue of AC is the shifting of the potential over time when implemented as a reference electrode.^[42] This potential shift was determined for the applied AC QRE in E- NaClO_4 by CV measurements of LTO//AC cells over time and is presented in Figure A1 (section 10 *Appendix*). The first recorded cyclic voltammogram is demonstrated in section 10 *Appendix*, Figure A1a to indicate the chosen redox couple for the analysis. Different from the application of LTO in LIBs,^[42] higher polarization effects are occurring in NIBs (section 10 *Appendix*, Figure A1a) due to the different properties of Li^+ and Na^+ . Nevertheless, a redox couple can be identified (dashed line, section 10 *Appendix*, Figure A1a) to study a possible change in potential of the AC QRE in NIBs. The potential shift was found to be 0.18 V after 275 h (section 10 *Appendix*, Figure A1b). Such potential shifts of AC QREs can impair mechanistic investigations and need to be stabilized before the evaluation of electrochemical mechanisms, especially during long-term cycling.^[42,138] Yet, a stabilization of the AC QRE in different electrolytes is not unconditionally possible and the AC QRE likely needs to be specifically modified for every electrolyte under consideration.^[42] Therefore, the determination of a stable and reliable reference electrode is crucial for further experiments. To achieve this aim, a stabilization of the sodium metal towards the electrolyte would be a desirable objective. Liu *et al.*^[129] observed a stabilization of the sodium metal in a bis(2-methoxyethyl) ether (diglyme) based electrolyte. The authors additionally described a low polarization of Na. Moreover, Han *et al.*^[148] elucidate the stabilization of Na deposition during cycling when FEC was added to carbonate-based electrolytes. Nevertheless, all authors examined the interplay between the electrolyte and different active materials when adding FEC or

substituting carbonates by ether-based solvents.^[8,40,90,93,125,126,149] The interaction of the electrolyte with the sodium-metal counter or reference electrode usually remains neglected.^[149] For this reason, sodium metal was placed inside two electrolyte solutions which were reported to stabilize sodium-containing cells: 1M NaClO₄ in EC/DMC + 5 % FEC and 1M NaClO₄ in diglyme. In analogy to Figure 6 (section 5.1.1), the result after three days are displayed in Figure 11.

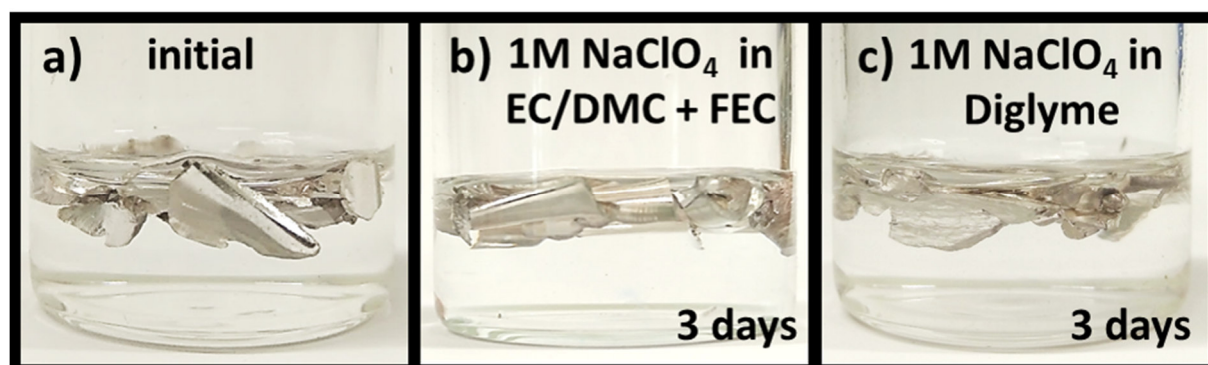


Figure 11. a) Na metal in E-NaClO₄ right after Na addition (representative for all electrolytes), b) Na metal in E-NaClO₄ + 5 % FEC and c) in 1M NaClO₄ in diglyme after three days.

Interestingly, no transformation neither of the sodium metal nor of both electrolyte solutions can be observed optically (Figure 11b, c). The addition of FEC and the replacement of carbonate-based solvents by diglyme, lead to a stabilization of the sodium metal. This outcome will be further underpinned by the application of these electrolyte solutions in a NIB half-cell with a high capacity negative electrode.

5.3 Exemplary model – the interaction between electrolytes and Sb₂O₃-based electrodes in NIBs: uncovering detrimental effects of diglyme

Section 5.3 is extracted from the scientific publication “The Interaction Between Electrolytes and Sb₂O₃-based Electrodes in Sodium Batteries: Uncovering Detrimental Effects of Diglyme”.^[171] All contributions are stated in section 12.

As presented in Figure 11a and b, sodium metal can be stabilized towards the electrolyte by altering the solvent components. Still, such effects need to be studied in an electrochemical system to probe whether sodium metal can be applied as a counter and reference electrode. Furthermore, active materials with complex electrochemical mechanisms can enhance the reactivity of the electrochemical system and, therefore, require optimized interactions between all components of the cell. To explore such an interplay between various cell components, Sb₂O₃ was chosen as a model high capacity active material with conversion and alloy type mechanism.^[83]

5.3.1 Sb₂O₃ characterization

Figure 12a shows the refined X-ray diffraction pattern. All reflexes of the XRD pattern can be assigned to cubic Sb₂O₃ with the space group of $Fd\bar{3}m$ (ICSD: 240206). The obtained Rietveld parameters are: $a = b = c = 11.1571(1)$ Å; R_p : 8.50; R_{wp} : 8.79. Scanning electron micrographs (Figure 12b) reveal that the commercial nanopowder consists of angular as well as spherical particles with a size of 0.05 – 1 µm.

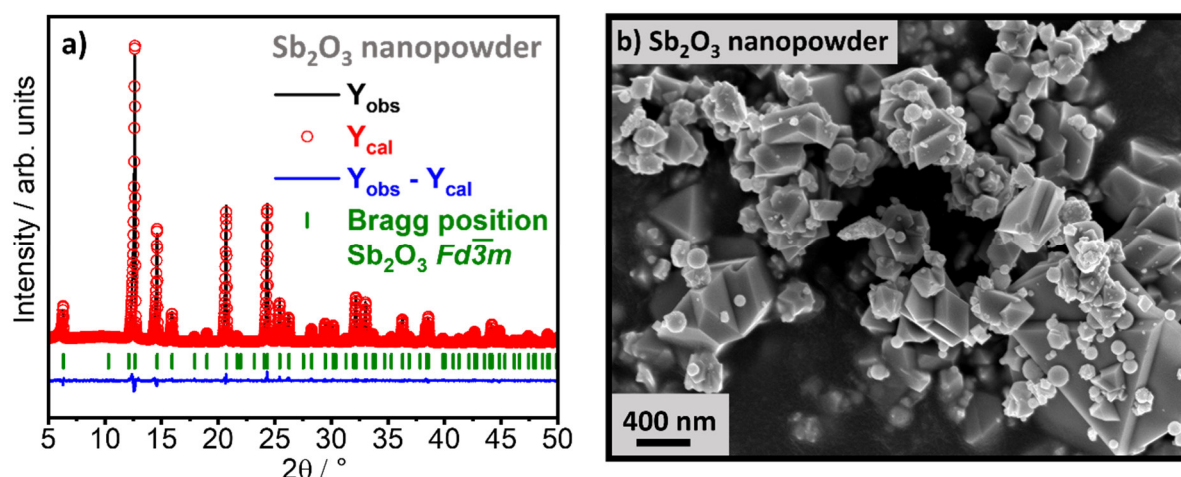


Figure 12. a) Rietveld-refined diffractogram, including peak positions and b) scanning electron micrograph of Sb₂O₃ powder.

5.3.2 Influence of the electrolyte solution on the electrochemical performance

The influence of the different electrolyte solutions on the electrochemical stability is demonstrated in Figure 13a and the corresponding Coulombic efficiency in Figure 13b.

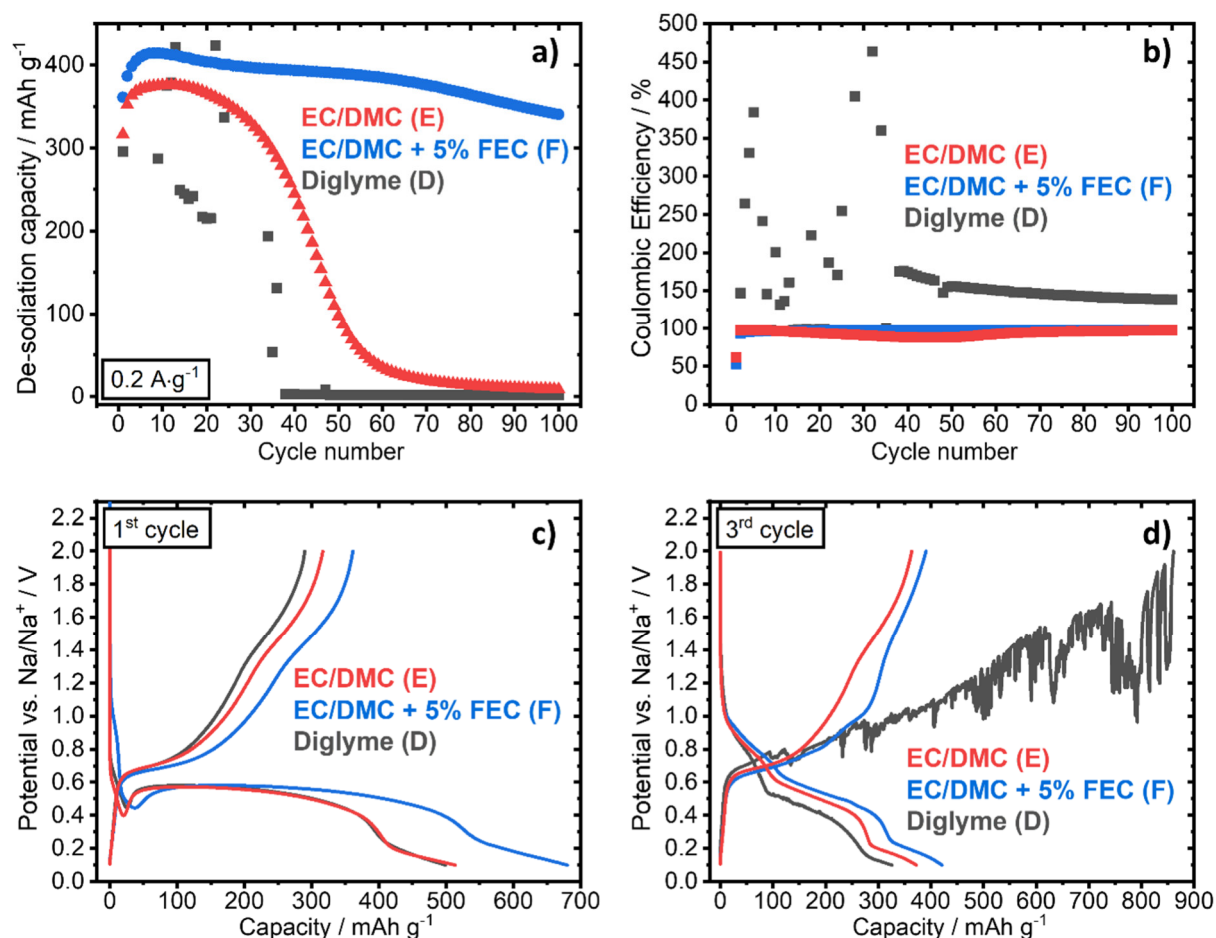


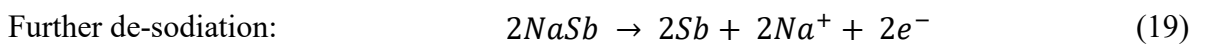
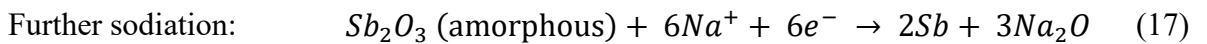
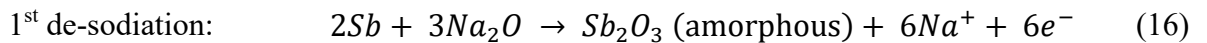
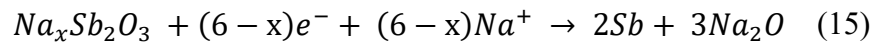
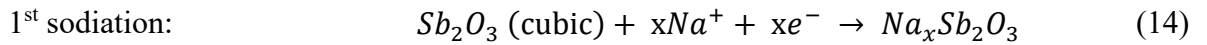
Figure 13. Sb_2O_3 based electrode cycled at 0.2 A g^{-1} in D, E and F solutions: a) electrochemical cycling stability, b) Coulombic efficiency, c) galvanostatic charge/discharge profiles of the 1st cycle, d) galvanostatic charge/discharge profiles of the 3rd cycle.

In order to simplify the discussion, the electrolyte solutions will be referred to as D (1M NaClO_4 in diglyme), E (1M NaClO_4 in EC/DMC) and F (1M NaClO_4 in EC/DMC + 5% FEC). Applying E as an electrolyte solution, the capacity drastically declines from 375 mAh g^{-1} to 75 mAh g^{-1} after 50 cycles. The capacity fading is accompanied by a decrease of the Coulombic efficiency from 97 % to 87 %, indicating an increase of irreversible side reactions. Such behavior is in line with the previous results revealing that sodium metal, which was used as a counter and reference electrode, reacts with carbonate-based electrolyte solutions irreversibly forming problematic byproducts.^[56] As a consequence, fast degradation appears in sodium metal-containing three-electrodes setups.^[56]

A remarkable improvement is observed when FEC is added to the electrolyte solution. This can be attributed to superior the SEI properties of both the working and the counter electrodes.^[93,126]

When FEC is added to carbonate-based electrolyte solutions its reduction takes place on Li, Na and all kinds of reducing Li and Na compounds (including lithiated and sodiated products of conversion reactions). As a consequence, protective surface layers that contain polymeric species and ionic Li or Na compounds are formed. This passivates highly reactive electrodes but allows very good Li⁺ or Na⁺ transport to/from the electrodes.^[40,62,93,172,173] Such effects substantially contribute to the stability of the electrolyte solution, which contains FEC towards the sodium electrodes, as was shown in a previous work.^[59] Additionally, the Coulombic efficiency stabilizes at 98% after 10 cycles, confirming a stabilization of the electrodes towards side reactions. Nevertheless, the processes are not entirely reversible, since, for rechargeable batteries, a Coulombic efficiency around 100% for both anode and cathode in the cells is mandatory. Different from the behavior in the organic carbonates based solutions, an irregular capacity progress occurs for the ether-based electrolyte solution. Irregular de-sodiation capacity values between 50 mAh g⁻¹ and 420 mAh g⁻¹ are paired with a Coulombic efficiency > 100 % during the initial 35 cycles. Thereafter, the cell lost its entire capacity.

For a more detailed examination of this peculiar behavior, galvanostatic sodiation/de-sodiation curves of the first (Figure 13c) and third (Figure 13d) cycles are illustrated. The processes occurring during sodiation and de-sodiation was described by Hu *et al.*^[83]:



The first sodiation step is associated with a pronounced plateau at ~ 0.55 V, similar for all electrolytes. As described in equation (14) and (15), an intermediate compound $\text{Na}_x\text{Sb}_2\text{O}_3$ is formed and further reduced to Sb and Na_2O . $\text{Na}_x\text{Sb}_2\text{O}_3$ is solely present during the first sodiation. The higher capacity of the FEC-containing cell is, most probably, caused by the formation of a polymeric SEI.^[40,62,172] Two processes can be determined at ~ 0.7 V and ~ 1.4 V during subsequent de-sodiation (Figure 13c), which correspond to the reactions described in equation (16) and (17). The galvanostatic profiles of Sb_2O_3 in organic carbonate-based electrolyte solutions do not change when comparing the first and third cycles (Figure 13c and d) following equations (17) – (20). Different from that, the galvanostatic de-sodiation profile of the cells cycled with electrolyte solution denoted as D demonstrates a severely irregular course starting from the second cycle. To further understand the described phenomena, an *ex-situ* characterization of the counter and working electrodes and the electrolyte solution is performed after cycling.

5.3.3 *Ex-situ* characterization of Sb_2O_3 electrodes

Scanning electron micrographs of the pristine electrode and the electrodes cycled 50 times in the respective electrolyte solutions are presented in Figure 14 a – d.

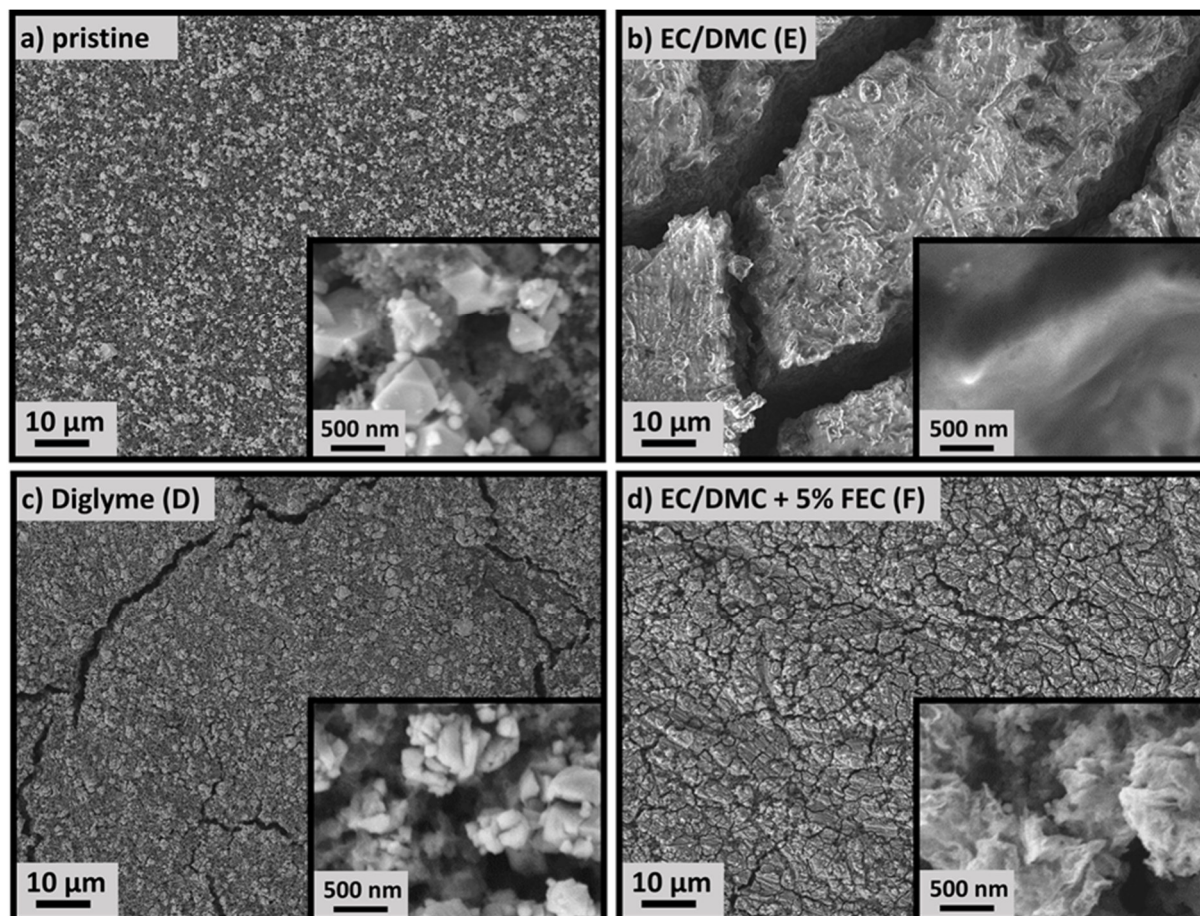


Figure 14. Scanning electron micrographs with high magnification insets of Sb_2O_3 electrodes: a) pristine, b) after 50 cycles in solution E, c) after 50 cycles in solution D, d) after 50 cycles in solution F.

The pristine electrode (Figure 14a) consists of a well-distributed network of Sb_2O_3 particles with irregular polyhedral shape and C65 conductive additive. Massive differences are observed when comparing the pristine electrode with the electrodes cycled in organic carbonate-based solutions (Figure 14b, d). In the case of the electrolyte solution E (Figure 14b), a pronounced cracking of the electrode is observed. Additionally, a surface layer covers the entire electrode. Since no Sb_2O_3 particles are visible, most probably, the thick layer observed on the electrode surface after being cycled in solution E originates from decomposition products formed by side reactions between sodium and the electrolyte solution.^[56] If the surface layer is not flexible enough, it could crack due to volume expansion during the conversion reaction, which in turn leads to new side reactions on the exposed parts of the electrode.^[59] This matches with the poor

performance of the cell cycled in electrolyte solution E (Figure 13a) and with the results obtained in section 5.1.^[56] The electrode cycled in solution F (Figure 14d) is also covered by a surface layer. However, the electrode microstructure is still visible, indicating that the layer formed in electrolyte solution F is thinner than that formed in electrolyte solution E (Figure 14b). Furthermore, electrode cracking is less distinct, most likely as a result of the flexible polymeric nature of the surface layers formed by reduction of FEC.^[79,172] Considering the electrode, which was cycled in electrolyte solution D (Figure 14c), distinct cracks are visible but the inset displays that the distribution and surface morphology are very similar to that of the pristine electrode. No visible surface layer has formed on the electrode during cycling in solution D. Nevertheless, the particles morphology has changed compared to that of the pristine electrode (Figure 14a), which is probably caused by the conversion reaction corresponding to equation (16), (17), and (20).

To thoroughly understand the impact of the electrode's surface layers on their electrochemical behavior, a surface analysis by using energy-dispersive spectroscopy and X-ray photoelectron spectroscopy is conducted. The corresponding results are presented in Figure 15 and Figure 16, respectively.

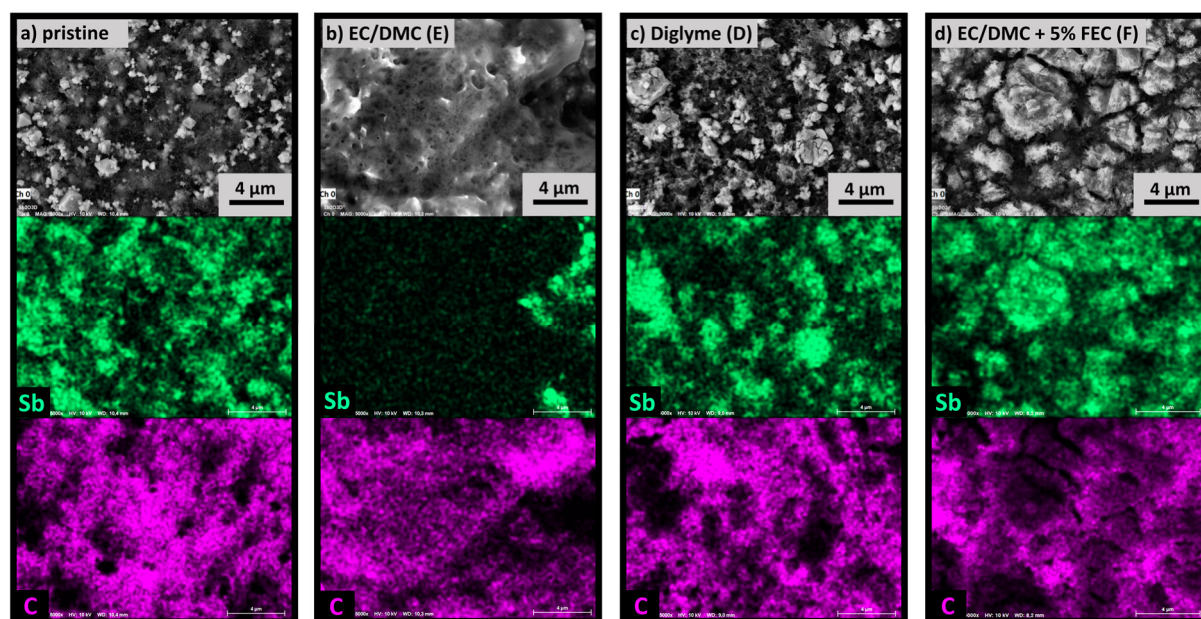


Figure 15. Scanning electron micrographs and EDS maps of Sb_2O_3 electrodes: a) pristine, b) after 50 cycles in solution E, c) after 50 cycles in solution D, d) after 50 cycles in solution F. EDS signals of antimony are highlighted in green and signals of carbon in magenta.

An Sb signal can be detected in the EDS maps for the pristine electrode (Figure 15a) as well as for electrodes cycled in solution D (Figure 15c) and F (Figure 15d). Different from that, the Sb

signal is very weak in most areas of the electrode cycled in solution E (Figure 15b) The imaging depth of EDS is in a range of $\sim 1 \mu\text{m}$ at 10 kV. Hence, the surface layer formed in solution E is relatively thick, exceeding the nanometer range. Such a thick surface layer could form in the presence of decomposition products and lead to a capacity decline throughout the cycling process. Different from that, surface reactions in solutions D and F provide surface layers, which are thinner than $1 \mu\text{m}$. For this reason, XPS spectra were recorded in order to enable comparison among the surface films thicknesses of the respective cycled electrodes.

The presence of an $\text{Sb}^{3+} 3d_{5/2}$ signal in the Sb 3d spectra and a Sb_2O_3 signal in the O 1s spectra indicate that the surface layer is thinner than 10 nm as this is the imaging depth of XPS. These signals are solely present for the pristine electrode (Figure 16b) as well as for electrodes cycled in electrolyte solution D (Figure 16h). Sb signals are neither existing in spectra related to electrodes cycled in solution E (Figure 16d) nor spectra of electrodes cycled in solution F (Figure 16f). Consequently, the surface layers' thicknesses depending on the related electrolyte solution in which the electrodes were cycled are $> 1 \mu\text{m}$ for solution E, between 10 nm and $1 \mu\text{m}$ for solution F and $< 10 \text{ nm}$ for solution D. The presence of FEC helps to form flexible surface layers with an adequate thickness, which can improve the electrochemical performance (Figure 13). In general, the surface layers on the electrodes cycled in all three solutions consist of the same carbon-containing species in different ratios indicated in the C 1s spectra (Figure 16a, c, e, and g). However, understanding the specific influence of these species is beyond the scope of this work. Further evaluation of the electrodes' surface chemistry in solution E is not implemented in the following course of this study, as the influence of parasitic reactions and decomposition products reasonably explains the poor electrochemical performance and these issues were already discussed in section 5.1.2 and elsewhere.^[56,59]

5.3.4 *Ex-situ* characterization of the electrolyte and sodium-metal counter electrode

An *ex-situ* optical analysis of the cycled electrolyte solutions (Figure 17a, d), separators (Figure 17b, e) and counter electrodes (Figure 17c, f) was conducted after cycling in solutions D and F, respectively. The post mortem analyzes of the solutions, electrodes and separators after cell cycling in solutions D and F emphasizes well the difference between a suitable (F) and unsuitable (D) solution.

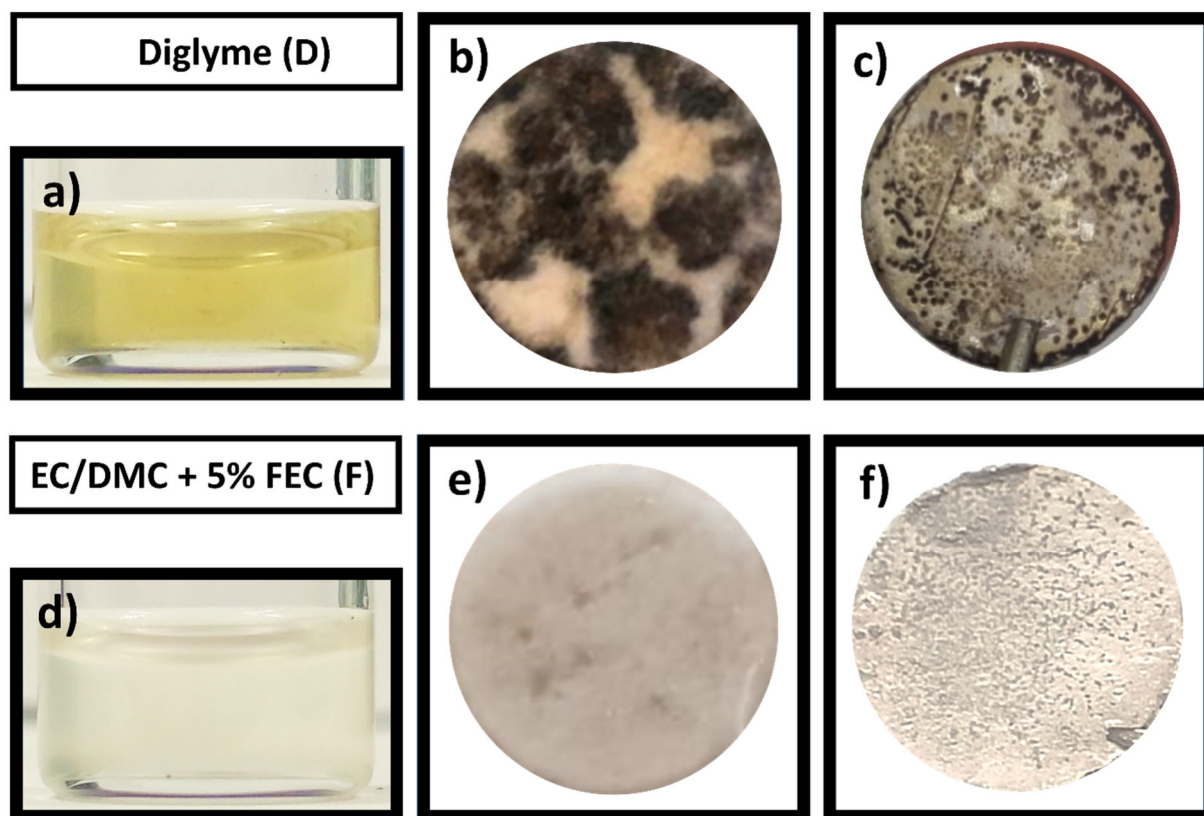


Figure 17. Cell components removed after 50 cycles: a) electrolyte solution D, b) electrolyte solution F, c) separator cycled in solution D, d) separator cycled in solution F, e) sodium-metal counter electrode cycled in solution D, f) sodium-metal counter electrode cycled in solution F.

Previous to the electrochemical cycling, the electrolyte solutions were both clear and colorless. The GF/D separators were plain white and the Na counter electrodes were shiny metallic discs. A strong color change occurred for the solution (Figure 17a), the separator (Figure 17b) and the Na counter electrode for cells cycled with D (Figure 17c). In contrast, a similar analysis of cells cycled with F does not show any pronounced changes. The electrolyte solutions presented in Figure 17a and d were analyzed by inductively coupled plasma mass spectrometry to determine the Sb content. Both pristine electrolyte solutions contained $< 0.022 \text{ mg L}^{-1}$ Sb. After 50 cycles, 12.3 mg L^{-1} Sb was detected in solution D and 0.5 mg L^{-1} Sb was detected in solution F. Consequently, the Sb quantity in cycled solution D is ~ 24 times higher than in cycled solution F.

In order to further examine the behavior of the dissolved Sb species on the counter electrodes, the cycled sodium metal counter electrodes were analyzed by SEM and EDS (Figure 18).

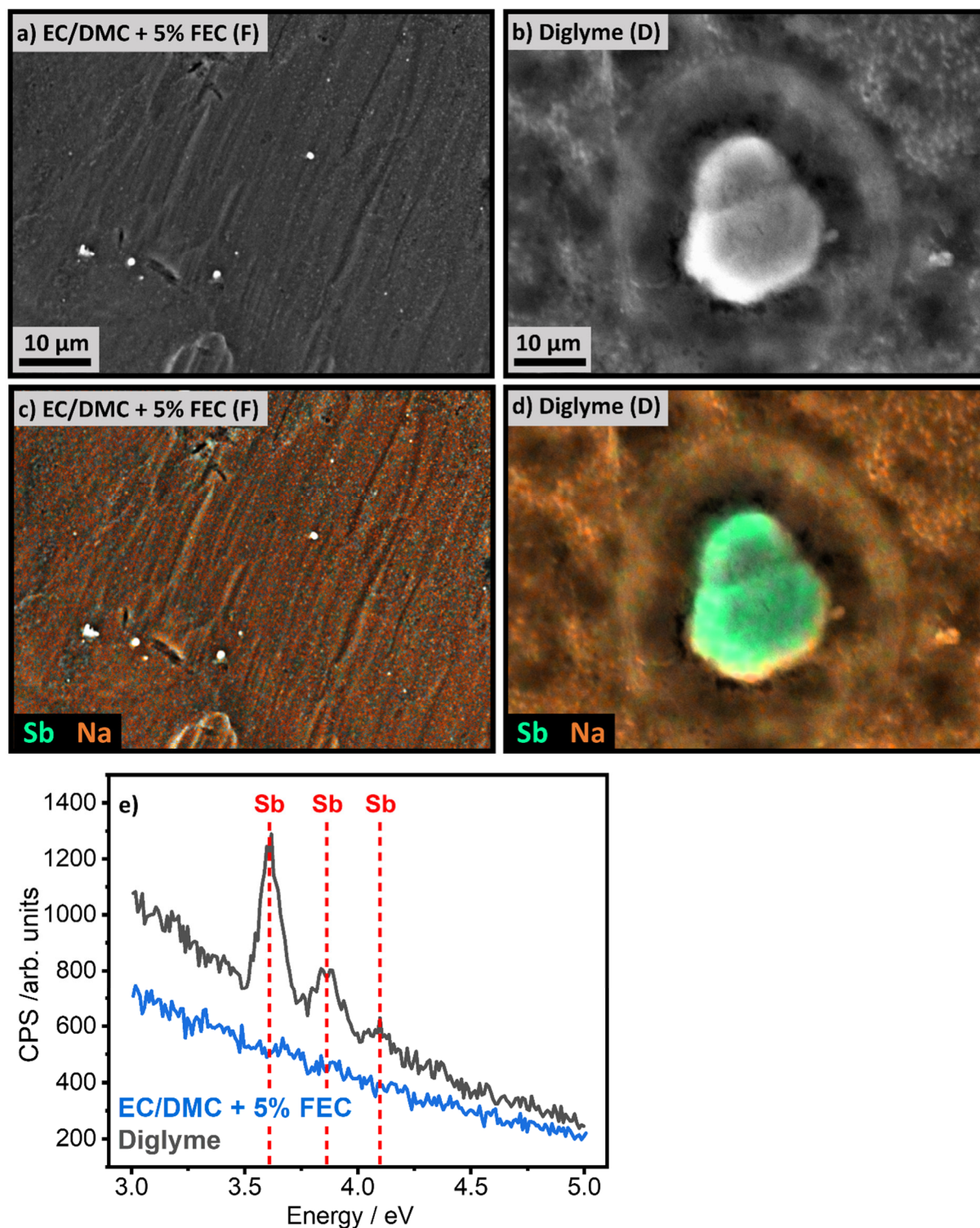


Figure 18. Scanning electron micrographs and the corresponding EDS maps of the sodium counter electrode after 50 cycles in a) + c) electrolyte solution F, b) + d) electrolyte solution D. EDS signals of antimony are highlighted in green and signals of sodium are highlighted in orange. f) Comparison of EDS spectra of the sodium counter electrodes cycled in electrolyte solutions F and D, respectively.

The surfaces of the Na counter electrodes cycled in cells containing solution F have smooth textures and do not show any visible surface films in the SEM images (Figure 18a). In contrast, the surfaces of the Na counter electrodes cycled in cells containing solution D are covered by a porous film (Figure 18b). Additionally, a ~10 μm sized round shaped particle was found embedded in the surface film of the Na electrode cycled in solution D. The associated EDS map is shown in Figure 18c – d. No antimony is found on the counter electrode cycled in cells with solution F (Figure 18c). In contrast, the large round-shaped particles visible on the Na electrodes from cells cycled with solution D can be identified as Sb containing materials (Figure 18d). Moreover, antimony signals were solely present on the surfaces of Na counter electrodes cycled in cells that contained electrolyte solution D (Figure 18e).

5.3.5 A proposed mechanism that explains the behavior of Sb_2O_3 electrodes cycled in diglyme-based electrolyte solutions.

Based on the results provided throughout this study, it is expected that the ether coordinates and dissolves Sb^{3+} , which is formed during de-sodiation (discharge). This hypothesis is supported by the work of Koshima and Onishi.^[174] These authors describe the extraction of Sb^{3+} with crown ethers. It was possible to extract 96 – 94 % Sb^{3+} from a hydrochloric acid solution due to the coordination features of the ethers. Furthermore, Beagley *et al.*^[175] also described ether-based complexes of Sb^{3+} . If Sb^{3+} cations are dissolved in the electrolyte solution due to the ability of diglyme to coordinate to the Sb ions, they can migrate and diffuse to the sodium metal counter electrodes and be reduced therein to metallic antimony. Subsequently, metallic Sb is plated on the sodium metal due to the low redox potential of Na (Figure 18d). These additional side processes interfere with the processes presented in equations (14) – (20) above. Such scenarios induce extremely non-uniform reactions in sodium-ion battery systems, as observed with cells containing diglyme based solutions (denoted as D) (Figure 13d). Of course, an easy dissolution of Sb cations is facilitated by the absence of passivating surface films on the electrodes in diglyme solutions, because of the relatively low intrinsic reactivity of ether solvents (in general) towards active metals such as Li and Na.^[128,148] The de-sodiation is accompanied by constant dissolution of the active material and its simultaneous deposition on the counter electrode. Such additional mechanisms most probably cause an irregular de-sodiation profile and an unexpectedly high de-sodiation capacity. Side processes like a dissolution of the active material can badly affect any formation of protective surface films. The obvious result of this problematic situation is the poor cycling stability of cells containing the ethereal electrolyte solution denoted as D (Figure 13a) and the strange cycling efficiency (Figure 13b). In summary, the

high content of Sb in the cycled diglyme-based electrolyte solution and on the Na counter electrodes taken from cycled cells proves that the active material is indeed dissolved in these cells. Also, minor amounts of Sb were found in cycled FEC containing solutions (denoted as F). However, the Sb quantity in cycled glyme based solutions was ~24 times higher than the trace Sb content found in cycled FEC containing solutions. The yellow shade of the cycled solution D (Figure 17a) further reflects the presence of dissolved Sb ions inside this electrolyte solution. Interestingly, the negative impact of diglyme on conversion anodes comprising antimony oxide, as reported herein, was not observed with conversion anodes including tin compounds.^[31,127] Hence, the unique interactions between Sn cations and diglyme molecules do not exist when changing the central transition metal involved in the electrode's conversion reactions. This example underlines that a re-examination of the interplay between all components is crucial when altering the ingredients in an electrochemical cell.

5.3.6 Conclusive aspects: reactivity of the electrolyte solvent

The impact of different solvents on the electrochemistry in sodium-ion batteries was investigated. A comparison of EC/DMC, EC/DMC + 5 % FEC and diglyme, which are typically used in electrolytes for NIBs was presented. First, the positive effect of FEC when served as an additive in EC/DMC solvent-based electrolyte solutions is highlighted. The presence of FEC in EC/DMC based electrolytes leads to the formation of thin, compact and probably elastic surface films that passivate the Sb_2O_3 electrodes. This valuable additive also helps to protect the sodium counter electrodes from detrimental side reactions with the electrolyte solution.

Considering the diglyme based solutions, their ability to dissolve Sb based active materials during electrochemical cycling is emphasized. It is suggested that possible complexation of Sb cations by diglyme molecules promotes their dissolution and transport to the Na metal counter electrode side. This has a detrimental effect on the cell performance, as the dissolved Sb species are deposited on the sodium counter electrode. The use of such a solvent with high complexation affinity may be problematic for all kinds of electrodes based on conversion reactions, which contain transition-metal elements. This situation emphasizes the importance of a proper adjustment of specific characteristics, upon selecting electrolyte solutions for the individual sodium-ion battery system.

6 Antimony-based electrodes: structure, morphology and percolation

Section 6.1 and 6.2 are extracted from the scientific publication “Choosing the right carbon additive is of vital importance for high-performance Sb-based Na-ion batteries”.^[59] All contributions are listed in section 12.

An appropriate half-cell setup with Na-metal counter and reference electrodes and FEC containing electrolyte for the evaluation of high capacity electrodes was presented in section 5.2 and 5.3. This setup will be employed for further analysis of the alloy-type material antimony. Electrodes based on alloying reactions for metal-ion batteries offer high specific capacity but require bespoke electrode material design to enable high-performance stability. Alloy-type materials like antimony suffer from high volume change ($\sim 300\%$)^[29,35,40] slow reaction kinetics during the Na⁺-ion insertion and extraction process, and the capacity is fading.^[35,150] The addition of carbon can counteract these drawbacks. Hence, the influence of carbon is widely discussed, and several different carbon materials in various concentrations have been proposed in the literature (Table 1).

As discussed in section 3, is often not stated in the literature if the added conductive additive is included in the normalization.^[36,40,152] Furthermore, a variety of electrolytes, carbon types, Sb/C compositions, Sb sizes, and morphologies, etc. lead to an incomparability of Sb-based electrochemical systems and a lack of consistency. The following part of this thesis addresses such normalization inconsistencies and systematically explores the impact of carbon properties on Sb/C composite electrodes for NIBs. A comparison of six different conductive additives is given in this work. Optimum interaction between carbon and Sb is best enabled by OLCs due to their best ability to homogeneously distribute within the Sb matrix.

To evaluate the transferability of the promising features of OLCs, the synthesized Sb powder was replaced by commercially obtained Sb powder. This study demonstrates the essential role of the Sb powder particle size and highlights the necessity of individual adjustment of Sb morphology and particle size, carbon properties and carbon amount to obtain the best possible electrochemical behavior.

6.1 Normalization: significance for carbon-containing negative electrodes

6.1.1 Sb synthesis and characterization

Antimony nanopowder was obtained by a co-precipitation method. Figure 19a-b shows the refined X-ray diffraction pattern and scanning electron micrograph.

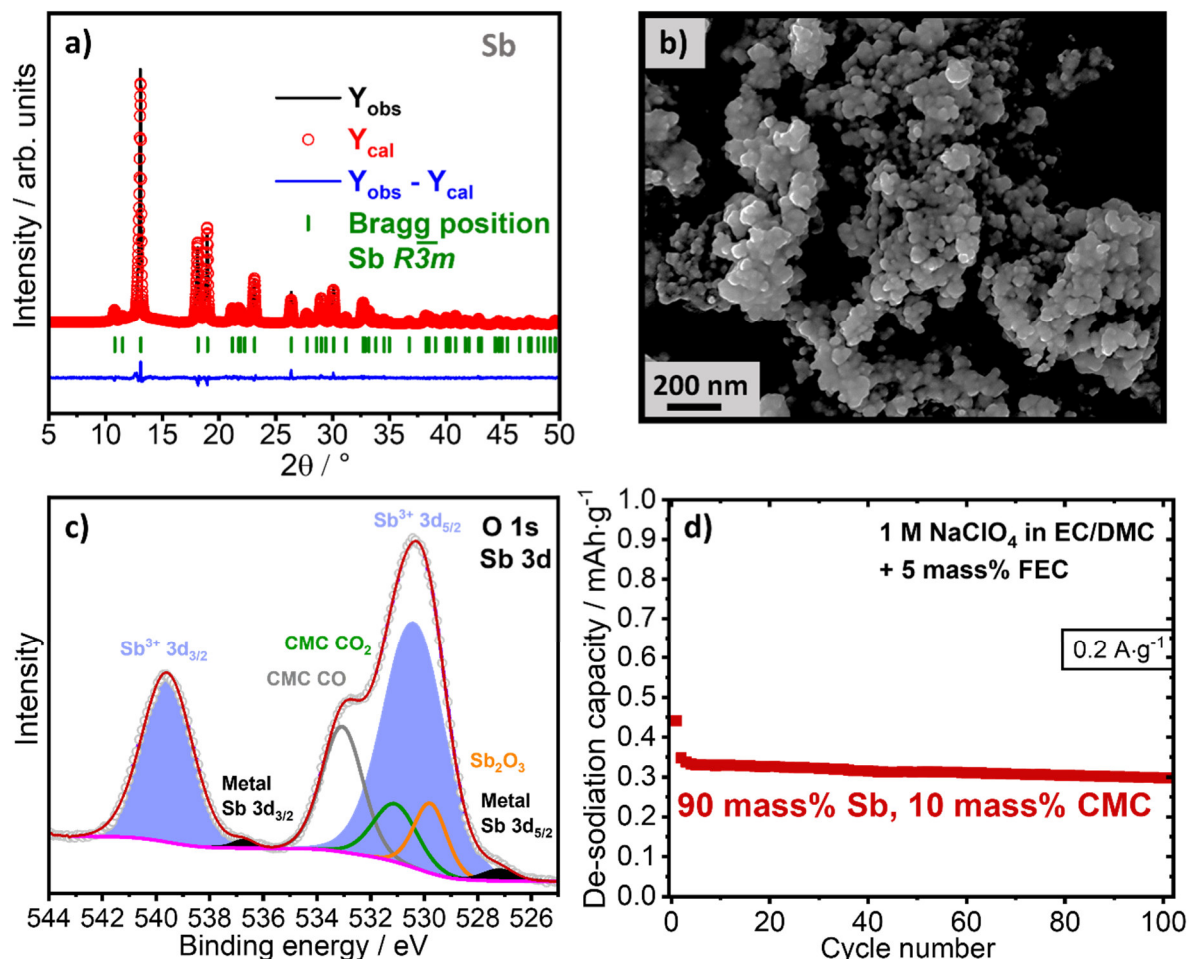


Figure 19. a) Rietveld-refined diffractogram and b) SEM image of the Sb powder; c) O 1s and Sb 3d XPS spectrum of a pristine electrode with 90 % (w/w) synthesized Sb and 10 % (w/w) CMC composition; d) Electrochemical cycling stability of this electrode at $0.2 \text{ A} \cdot \text{g}^{-1}$.

All reflexes of the XRD pattern can be assigned to trigonal Sb with the space group $R\bar{3}m$ (ICSD: 55402) comprised within agglomerated nanoparticles with a size of 10 – 50 nm (Figure 19b). The obtained Rietveld parameters are: $a = b = 4.3009(1) \text{ \AA}$, $c = 11.2835(4) \text{ \AA}$; Rp: 5.11; Rwp: 6.57. The resulting Sb powder was used to prepare an electrode without carbon (90 % (w/w) synthesized Sb and 10 % (w/w) CMC). In the O 1s and Sb 3d X-ray photoelectron spectrum of the pristine electrode (Figure 19c), peaks originating from metallic Sb and Sb^{3+} can be found. This means that the Sb particles are covered by a thin ($< 10 \text{ nm}$) oxide layer. Sb as

pure metal is electronically conductive but the metal oxide layer acts as an insulating layer between the Sb particles. The result is a high resistance of the electrode and a very poor electrochemical performance with a capacity close to zero (Figure 19d). This is why the presence of a conductive additive is of vital importance to enable Sb-based NIB electrodes.

6.1.2 Influence of the carbon amount and normalization

To understand the effect of a carbon additive on the Sb electrode performance, five electrodes with various ratios of Sb and carbon black (C65) were prepared. For all measurements, the amount of 10 % (w/w) CMC was kept constant, and the ratios of Sb/C65 were set to 85/5, 80/10, 75/15, 70/20, and 40/50. The cycling stabilities of the composite electrodes are illustrated in Figure 20a – b with normalization based on either Sb mass or combined Sb/C65 mass.

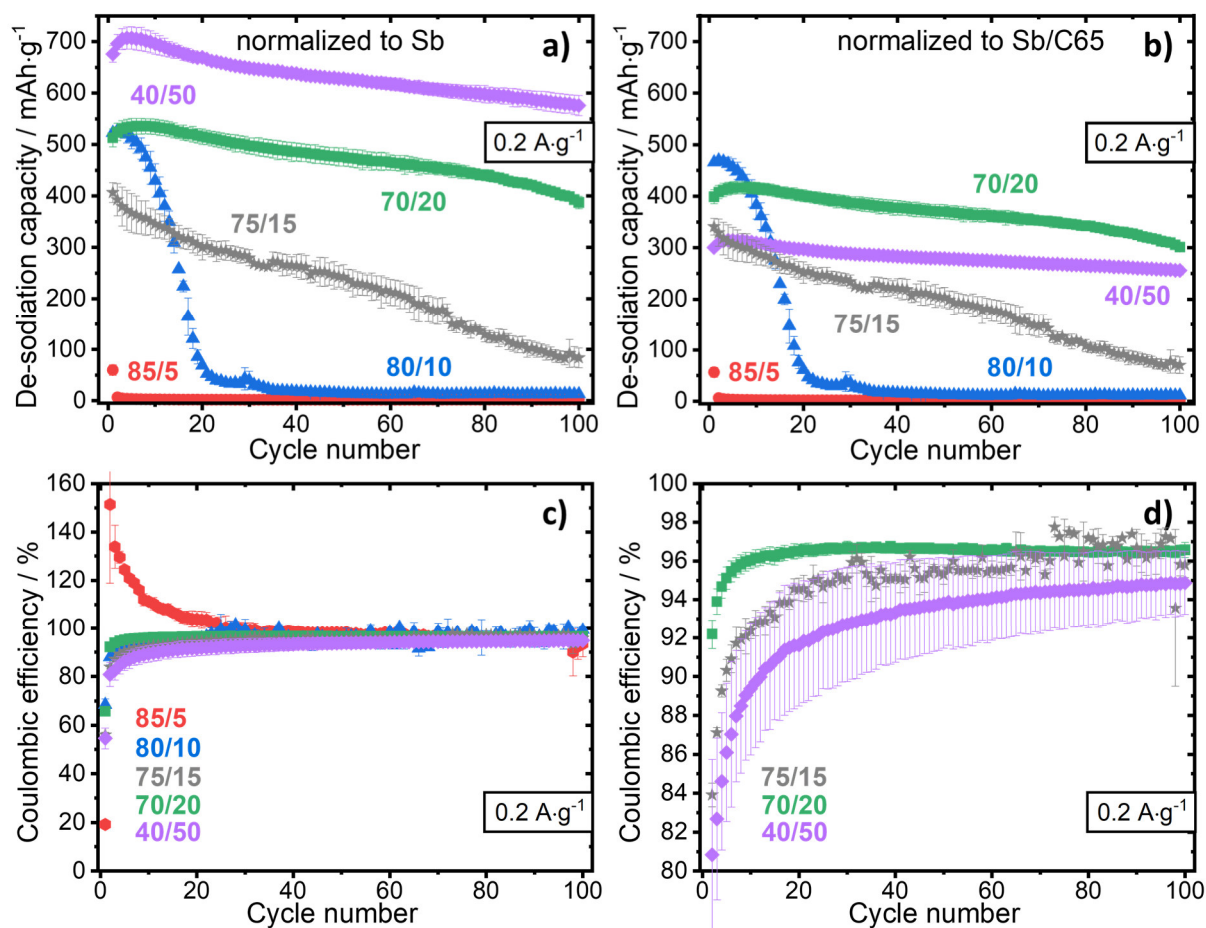


Figure 20. Electrochemical cycling stability at 0.2 A g^{-1} for different Sb/C65 ratios normalized to a) the Sb active mass and b) the Sb/C65 active mass; c) corresponding Coulombic efficiencies of all composites; d) magnification of Coulombic efficiencies for the Sb/C65 ratios of 75/15, 70/20, and 40/50.

As reported by Widmaier *et al.*,^[33] the amount and distribution of carbon can severely influence the electrochemical performance of battery electrodes. Therefore, an optimized electrical percolation of the electrode can significantly counteract side reactions with the electrolyte and enhance the electrochemical kinetics. In accordance, an increase of stability with a higher amount of carbon is also observed in this study. Additionally, the Coulombic efficiency is improved when using a larger amount of carbon (Figure 20d). Stabilization of the CE reaching > 97 % is evident when increasing the amount of carbon from 15 % to 20 %. However, by further addition of carbon, this trend reverses, and the CE values remain under 95 %. CEs higher than 100 % for sample 85/5 and 80/10 appear since almost no charge (~2 mAh g⁻¹ for 85/5 and ~40 mAh g⁻¹ for 80/10 after 20 cycles) was stored, and a high error of CE measurement can be expected. Due to its significant outer surface area (section 10 *Appendix*, Table A1), C65 undergoes detrimental side reactions. As the amount of C65 is increased, we see a decline in the CE. This aligns with the report of Spahr *et al.*^[60] that a percolation threshold is reached by a certain amount of carbon and further addition of carbon does not further improve the electrode resistivity.^[60] Since the cycling performance of the 70/20 electrode does not drastically improve by further C65 addition, it is expected that the percolation threshold is reached. For this reason, a ratio of 70 % (w/w) Sb and 20 % (w/w) C was selected for all follow-up experiments.

In Figure 20a the capacity values are normalized to solely the Sb mass, whereas a normalization to the total Sb+C65 mass is given in Figure 20b. With rising C65 amounts, the distinction between both normalizations becomes more relevant. After 20 cycles, the 40/50 electrode normalized to Sb reaches a capacity of 669 mAh g⁻¹, which even exceeds the theoretical value of 660 mAh g⁻¹. This is probably caused by the capacity contribution of C65 (Figure 23). The corresponding capacity of 297 mAh g⁻¹ for this electrode normalized to Sb/C65 is 44 % lower as compared to normalization to Sb mass only. Similar differences are found in the literature when applying different ways of normalization (Table 1). For example, Cui *et al.*^[36] reached 630 mAh g⁻¹ normalized to the Sb+C mass. According to calculations, the maximum capacity with the electrode composition of Cui *et al.*^[36] (Table 1) is 396 mAh g⁻¹ if Sb would reach its theoretical capacity, and the carbon could deliver 300 mAh g⁻¹ (approximately the maximum value reported in the literature)^[27,73]. Different from that, Qian *et al.*^[93] reported a similar capacity of 610 mAh g⁻¹ by normalizing to solely the Sb mass. The necessity of correct referencing to which mass the normalization is applied but also the inclusion of all active components is highlighted by these examples. Consequently, comparisons to literature need to be considered carefully, and the normalization should be based on Sb and carbon content. Accordingly, all values are normalized to the combined mass of Sb and C in the following part of this work.

6.2 Carbon additives: the vital importance for high-performance Sb-based NIBs

6.2.1 Properties of the conductive carbon materials

We selected six different carbon materials with different characteristics as conductive additives in Sb-based NIB electrodes, namely, two types of carbon blacks (SuperP and C65), graphite (KS6L), carbon nanohorns (Nanostars), and two types of onion-like carbons (OLCs). We selected these specific carbon materials to cover an array of properties, including different size, shape, surface area, degree of ordering (graphitization), and heteroatom concentration (Figure 21).

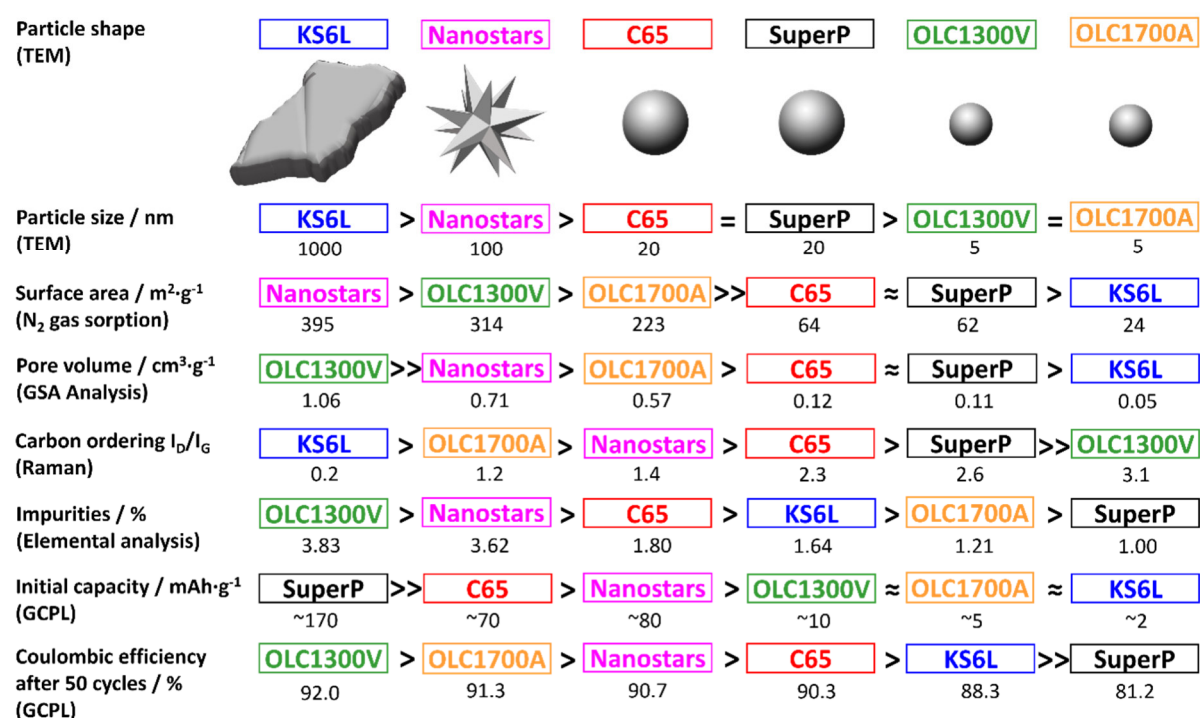


Figure 21. Overview of parameters obtained from GSA, TEM, Raman, and electrochemical analysis (galvanostatic charge/discharge cycling with potential limitation). The carbons are arranged depending on their properties towards the related characteristic with the corresponding value below.

Regarding the applied carbons in this study, information was provided in section 2.2.3. Two types of OLCs were synthesized to evaluate the influence of their different characteristics on the electrochemical performance of the Sb/C electrode. Nanodiamonds were annealed under vacuum at 1300 °C to obtain the OLC1300V sample, whereas the annealing of the OLC1700A sample was done at 1700 °C under argon atmosphere which is known to yield, besides carbon onions, a secondary phase of multi-layer graphene nanoribbons.^[120]

Transmission electron micrographs in Figure 22a – f show the morphology of all six carbon samples.

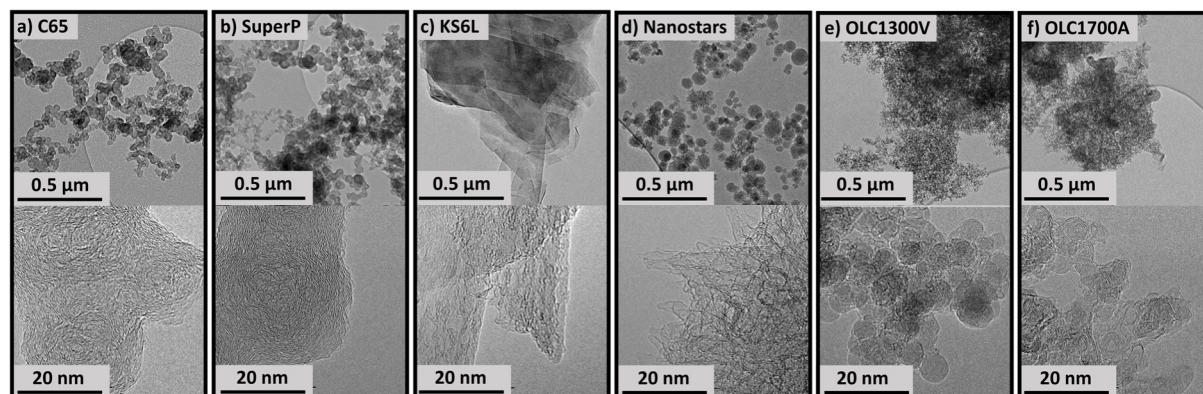


Figure 22. Transmission electron micrographs of a) C65, b) SuperP, c) KS6L, d) Nanostars, e) OLC1300V, and f) OLC1700A.

No morphological difference can be found between C65 and SuperP (Figure 22a – b). Both carbons form chain-like networks of round shaped particles with 20 – 30 nm diameter. Different from that, KS6L is composed of micrometer-sized edge graphite flakes (Figure 22c). In Figure 22d, we see aggregated nanohorns are arranged to 50 – 100 nm Nanostars with sharp tips forming their exterior shape. The conical spikes of the nanohorns can be spotted in the high magnification image of Figure 22d. An agglomerated network of carbon onions is seen for both OLC samples on a sub-micrometer length scale, while the individual OLC particles exhibit a multi-shell fullerene-like architecture with a diameter of 5 – 10 nm (Figure 22e – f). In contrast to OLC1300V, OLC1700A shows nanometer-sized carbon onions alongside few-layer graphene nanoribbons.^[117] The latter originate from carbon redistribution when carrying out the OLC synthesis in an inert atmosphere at ambient pressure and not in vacuum.^[117]

Table 4. Results from elemental analysis of the carbon samples (no H or S detected).

Sample	C / % (w/w)	N / % (w/w)	O / % (w/w)
C65	98.20±1.03	-	0.88±0.14
KS6L	98.36±0.67	0.21±0.01	0.99±0.26
Nanostars	96.38±0.49	0.57±0.06	3.13±1.00
OLC1300V	96.17±1.32	1.55±0.02	1.14±0.31
OLC1700A	98.79±0.78	0.36±0.09	0.83±0.22
SuperP	99.00±0.90	0.35±0.08	0.60±0.04

Elemental analysis (Table 4) reveals that all samples are mainly composed of carbon with small amounts of oxygen- and nitrogen-containing surface functional groups. SuperP carbon has the lowest amount of surface functional groups with 1 % (w/w), whereas OLC1300V contains 3.83 % (w/w).

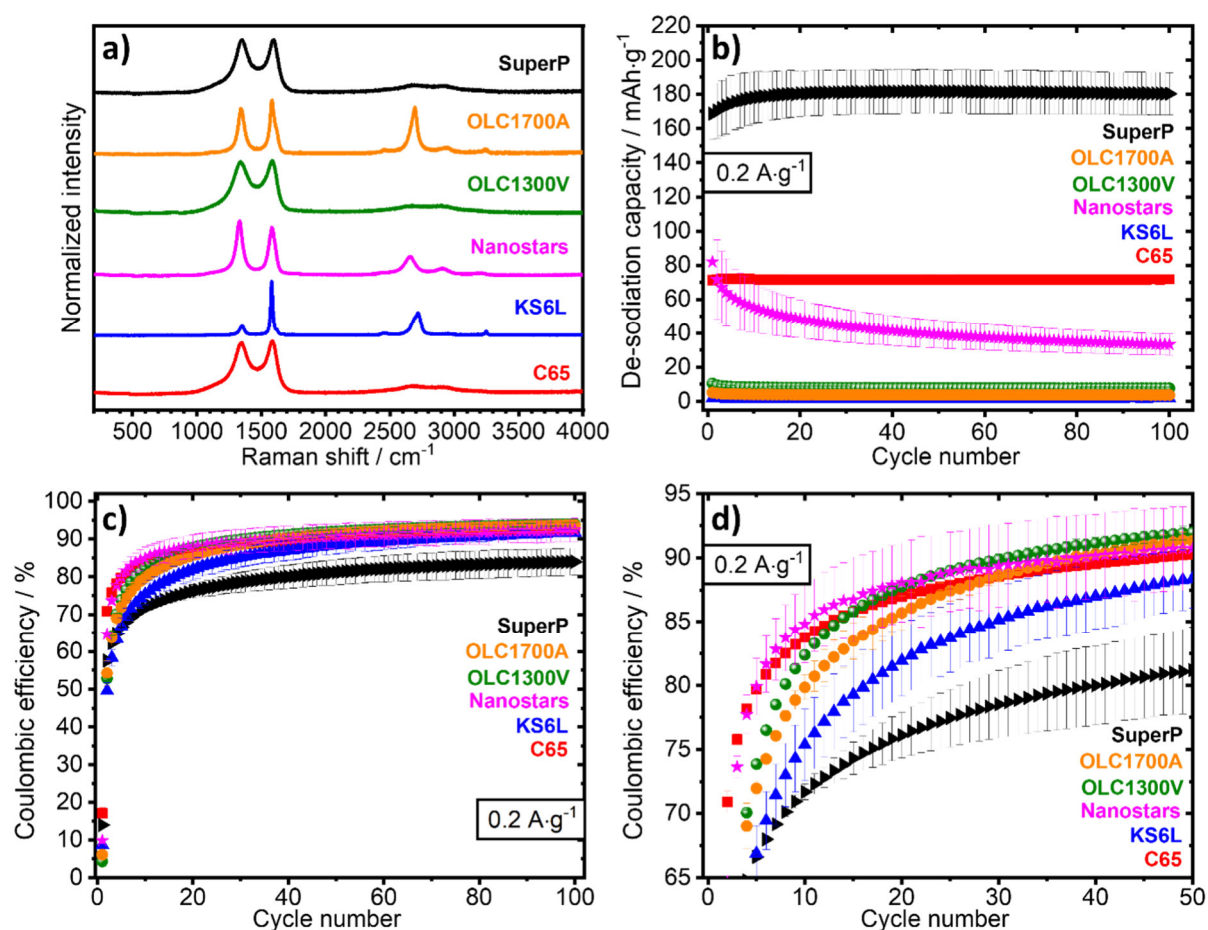


Figure 23. a) Raman spectra of the carbon samples, b) electrochemical cycling stability at 0.2 A g^{-1} for electrodes composed of 90 % (w/w) of the respective carbon and 10 % (w/w) CMC; c) and d) the related Coulombic efficiencies.

Raman spectra of the carbon samples are shown in Figure 23a. The D- and G-modes in the area of $1200 - 1700 \text{ cm}^{-1}$ appear for each sample at different positions and with different intensities depending on their structural features. The degree of carbon ordering (graphitization) can be obtained from the D- and G-mode FWHM (full-width at half-maximum) values and the intensity ratio I_D/I_G .^[176,177] A low I_D/I_G ratio together with low FWHM values indicate a high degree of structural order within the carbon.^[178] A detailed analysis of the D- and G-modes and their intensities is given in section 10 *Appendix*, Figure A3, and Table A2. A high graphitization is found for KS6L and OLC1700A due to low I_D/I_G values of 0.2 and 1.2, respectively. Low D- and G-mode FWHM values of 43 cm^{-1} and 19 cm^{-1} for KS6L and both 60 cm^{-1} for OLC1700A

correspond to that finding. The OLC1300V carbon possesses the lowest degree of graphitization with an I_D/I_G ratio of 3.1 and D- and G-mode FWHM values of 152 cm^{-1} and 80 cm^{-1} , respectively.

The specific surface area, pore-volume, and average pore width (volume-weighted) were determined by nitrogen gas sorption analysis, and the data are found in section 10 *Appendix*, Figure A2, and Table A1. OLC1300V and the Nanostars possess the highest BET surface area ($314\text{ m}^2\text{ g}^{-1}$ and $395\text{ m}^2\text{ g}^{-1}$) as well as the highest total pore volume ($1.06\text{ cm}^3\text{ g}^{-1}$ and $0.71\text{ cm}^3\text{ g}^{-1}$). KS6L shows the lowest porosity with a total pore volume of $0.05\text{ cm}^3\text{ g}^{-1}$ and a BET surface area of $24\text{ m}^2\text{ g}^{-1}$. C65 and SuperP present similar BET surface areas of $64\text{ m}^2\text{ g}^{-1}$ and $62\text{ m}^2\text{ g}^{-1}$ together with similar total pore volumes of $0.12\text{ cm}^3\text{ g}^{-1}$ and $0.11\text{ cm}^3\text{ g}^{-1}$.

Electrodes composed of the respective carbons and 10 % (w/w) CMC were prepared to evaluate the sodium-ion storage capacities. The de-sodiation capacity for each carbon sample over 100 cycles is depicted in Figure 23b. Two groups of carbons do not show any significant intrinsic de-sodiation capacity: graphite and carbon onions. KS6L as a typical graphite is incapable of sodium ion insertion within its structure.^[72] Moreover, OLCs are composed of closed carbon shells that do not offer any possibility for Na-ion insertion. The capacities delivered by both OLC samples as well as KS6L are attributed to physical electrosorption of Na^+ at the outer surface. Accordingly, a higher capacity for the onions ($4 - 8\text{ mAh g}^{-1}$) is obtained compared to KS6L (ca. 2 mAh g^{-1}) considering the higher surface area of the former ($205 - 286\text{ m}^2\text{ g}^{-1}$). All other carbons can insert Na^+ whereby SuperP delivers the highest de-sodiation capacity of 170 mAh g^{-1} . The Na^+ insertion mechanism in SuperP has been studied elsewhere.^[92] Atomic thick interlayer spaces of graphite and voids around defects of graphite can insert sodium-ions. Due to its similarities, we attribute the measured capacity of around 70 mAh g^{-1} provided by the C65 electrode to a similar sodium insertion as described for SuperP. Besides that, the carbon Nanostars can insert Na-ions with a resulting initial capacity of about 80 mAh g^{-1} .

The CEs for all carbons (Figure 23c – d) remain under a value of 90 %, which indicates a high amount of side reactions. For carbons that do not insert sodium-ions but have a large surface area (i.e., both OLCs), the deviation to 100 % CE is mainly attributed to side reactions located at the material surface. Especially SuperP suffers from side reactions. The CE of SuperP after 50 cycles persists at $\sim 80\%$. This irreversibility is attributed to enclosures of metallic sodium in the pores between the particles.^[92] Comparable processes are conceivable for the other carbons which insert Na^+ . For comparability, an overview of all carbon characteristics is displayed in Figure 21. These properties will be correlated to the electrochemical performance of the Sb/C composite electrodes in the following.

6.2.2 Influence of carbon characteristics on Sb/C electrodes

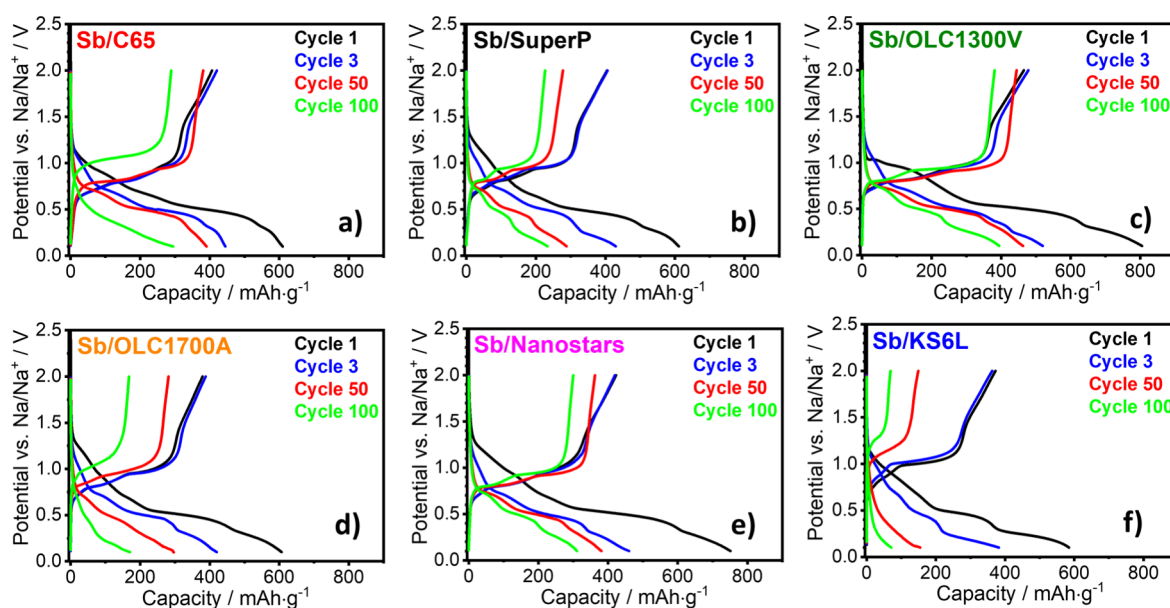


Figure 24. Galvanostatic charge/discharge profiles at 0.2 A g^{-1} for a) Sb/C65, b) Sb/SuperP, c) Sb/OLC1300V, d) Sb/OLC1700A, e) Sb/Nanostars, and f) Sb/KS6L.

The galvanostatic profiles (Figure 24) of the first three cycles are very similar for all cells. It can be confirmed for all electrodes, that the sodiation $\text{Sb} + 3\text{Na}^+ + 3\text{e}^- \rightarrow \text{Na}_3\text{Sb}$ takes place through several steps. Three pronounced plateaus are in-line with previous findings forming amorphous Na_xSb , crystalline NaSb, and crystalline Na_3Sb during sodiation.^[40,151] This indicates that the fundamental electrochemical process is not significantly varied by varying the type of carbon.

Table 5. Resistances of Sb/C electrodes calculated from the IR drop at 4 A g^{-1} . Sb/C electrodes were prepared in a ratio of 70 % (w/w) Sb nanopowder, 20 % (w/w) C of the respective carbon, and 10 % (w/w) CMC (dry mass).

Electrodes	U / V	I / A g ⁻¹	R / Ω cm ²
Sb/C65	0.456	4	0.515
Sb/SuperP	0.464	4	0.524
Sb/KS6L	1.686	4	1.907
Sb/OLC1300V	0.313	4	0.352
Sb/OLC1700A	0.370	4	0.420
Sb/Nanostars	0.505	4	0.569

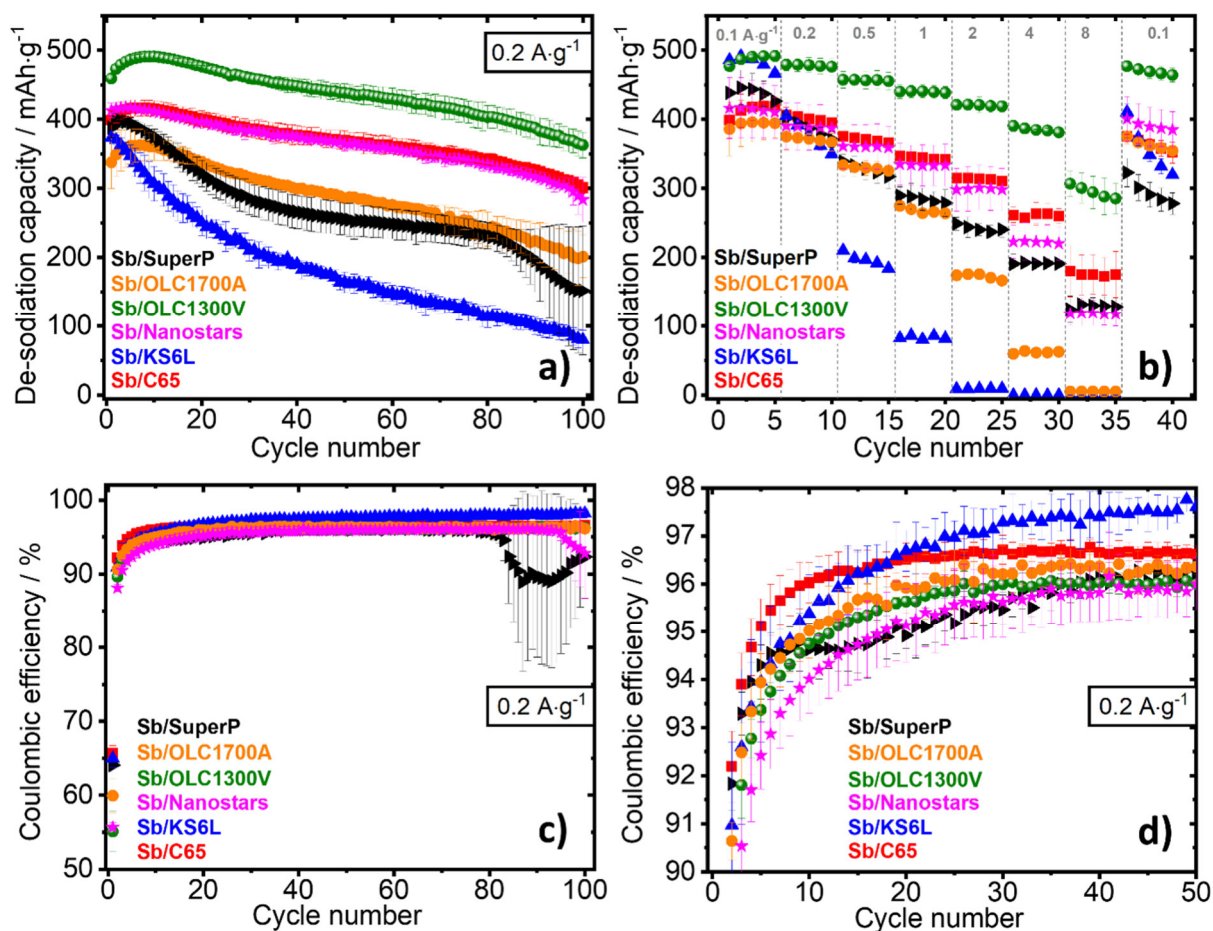


Figure 25. a) Electrochemical stability at 0.2 A g^{-1} and b) rate performance of the respective Sb/C electrodes; c) and d) Coulombic efficiencies.

The Coulombic efficiencies of all electrodes are presented in Figure 25c – d. All Coulombic efficiency values are comparable and do not exceed 98 %.

The lowest electrochemical performance is delivered by the Sb/KS6L electrode, especially at higher specific currents of 0.5 A g^{-1} (Figure 25b). Because of the flaked shape of KS6L and its considerably large carbon particles, the contact resistance between the active material and current collector is high. This hypothesis is confirmed by the highest resistance of $1.907 \Omega \text{ cm}^2$ calculated from the IR drop (Table 5). The large flakes of KS6L lead to inhomogeneous charge and voltage distribution with local degradation spots causing electrolyte decomposition.^[33] Even if the graphite itself does not suffer from volume expansion, with its large and rigid particles, it cannot buffer the volume expansion of Sb. KS6L is not suitable as a conductive additive in NIBs, and this conclusion aligns with the literature.^[179]

C65 and SuperP are the most similar carbons concerning their appearance and physicochemical properties resumed in Figure 21. The main difference is the higher initial de-sodiation capacity of 170 mAh g^{-1} and the lower CE of SuperP with respect to C65 (Figure 23b). These factors cause inferior electrochemical stability of Sb/SuperP as compared to Sb/C65 since high storage

capacity is usually connected to high volume changes. This leads to a rapid contact loss and explains the observed capacity fading for Sb/SuperP electrode (Figure 25a).

Carbon Nanostars are also capable of sodium-insertion and have an intrinsic capacity of about 80 mAh g⁻¹, which is similar to C65 (~70 mAh g⁻¹). Figure 25a – b illustrates that the electrochemical behavior (stability, and de-sodiation capacity) of Sb/C65 and Sb/Nanostars is also similar. Due to its higher resistance of 0.569 Ω cm², the rate capability of Sb/Nanostars is inferior to Sb/C65 (0.515 Ω cm², Table 5). This poorer conductivity is likely attributed to the shape of the carbon nanohorns with cone-like structures extending beyond the surface to create a rough morphology. The latter will reduce the effective contact area between Sb and carbon particles and decrease the electric conductivity.

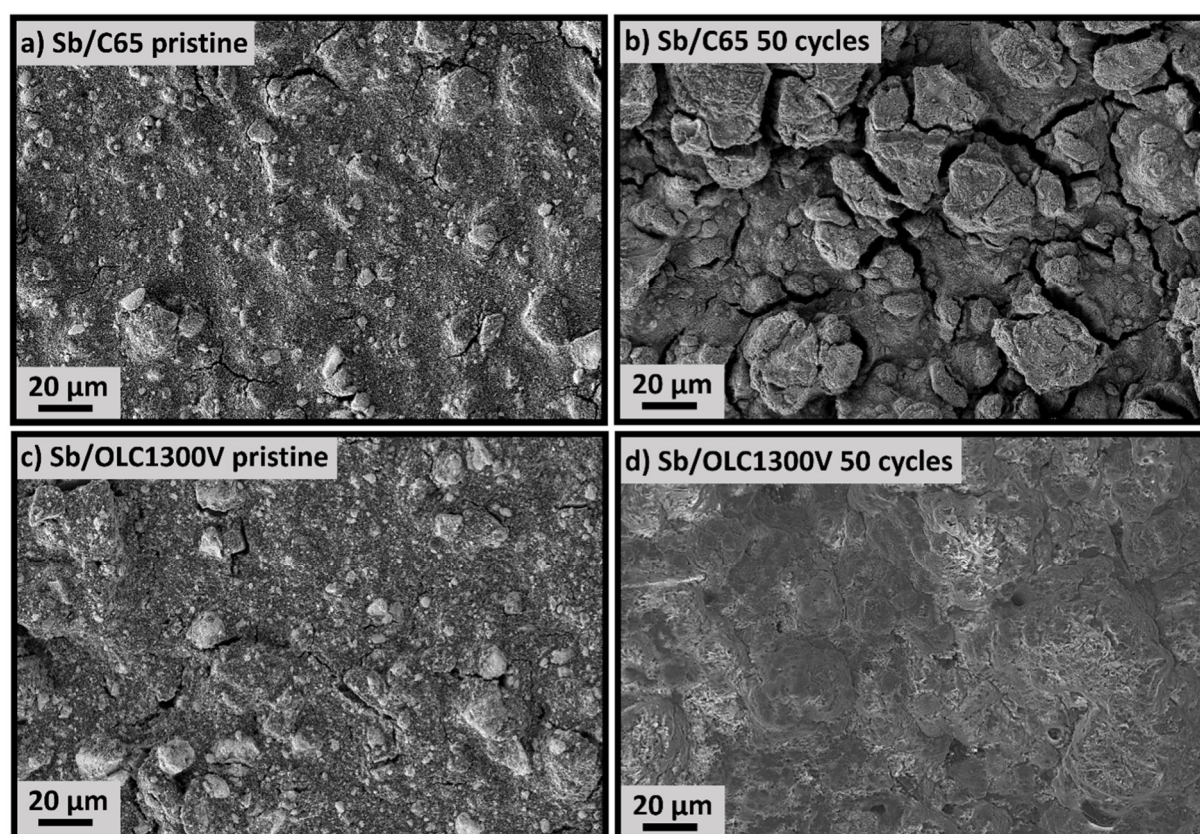


Figure 26. Scanning electron micrographs of a) pristine Sb/C65, b) Sb/C65 after 50 cycles, c) pristine Sb/OLC1300V and d) Sb/OLC1300V after 50 cycles.

An explanation for the exceptionally high and stable performance of Sb/OLC1300V can be deduced by comparing the main differences between OLC1300V and OLC1700A. The OLCs are both 5 – 10 nm sized particles, which are expected to provide excellent contact between carbon and Sb due to their round shape and smooth surface. However, the pristine electrodes differ from each other. Sb/OLC1300V consists of sub-micrometer-sized Sb agglomerates covered by the carbon particles (Figure 26c). Thereby, the Sb particles are well distributed within

a carbon matrix. Contrary, in the case of Sb/OLC1700A, Sb agglomerates are located on top of a carbon/Sb network (section 10 *Appendix*, Figure A4c). We explain the lower performance of the latter by the presence of few-layer graphene nanoribbons physically attached to individual carbon onions and clusters thereof. These OLC1700A carbon particles can form sintered clusters due to a higher pressure and temperature applied during annealing as compared to the synthesis of OLC1300V. This difference reduces the ability of OLC1700A to disperse within the Sb-matrix with the same homogeneity as OLC1300V. Accordingly, the sample with the best distribution of the current around the active material particles results in the highest conductivity (Table 5) and the best rate performance of OLC1300V (Figure 25b). Optimized conductive paths allow a homogenous charge transfer at the surface of the Sb particles. A larger volume of Sb becomes active causing the highest de-sodiation capacity (Figure 25a). The inhomogeneity of Sb/OLC1700A leads to poor buffering performance and electrode cracking (section 10 *Appendix*, Figure A4d). Besides the morphology, OLC1700A is highly graphitic with a lower degree of heteroatoms and defects compared to OLC1300V. Consequently, OLC1700A is presumably more inert towards reactions with the electrolyte or the active material. Disordered parts and impurities could catalyze the chemical reactions leading to an improved SEI, better-buffering effects, and better interaction between the active material and carbon.

All electrodes suffer from cracking after cycling (Figure 26b and section 10 *Appendix*, Figure A4b, d, f and h) caused by the Sb volume expansion. Sb/OLC1300V electrode (Figure 26d) is the only exception and has also the best rate capability, highest conductivity, and highest capacity. For comparison, scanning electron micrographs of Sb/C65 and Sb/OLC1300V before and after cycling are reported in Figure 26. The pristine electrodes (Figure 26a, c) do not differ significantly. Still, the particles are unevenly dispersed, and several cracks are apparent. A massive change of the electrodes after 50 cycles can be observed. Cracking occurs for all electrodes across the entire area (Figure 26b and section 10 *Appendix*, Figure A4b, d, f and h) with the noticeable exception of Sb/OLC1300V (Figure 26d). Crack formation leads to the disruption of conductive pathways. No cracks are apparent for Sb/OLC1300V, and conductive paths were not affected for Sb/OLC1300V during cycling. The Sb/OLC1300V electrode was able to attain 300 mAh g⁻¹ even at 8 A g⁻¹, which is remarkable when considering the slow reaction kinetics usually associated with alloy materials.^[30,35,150]

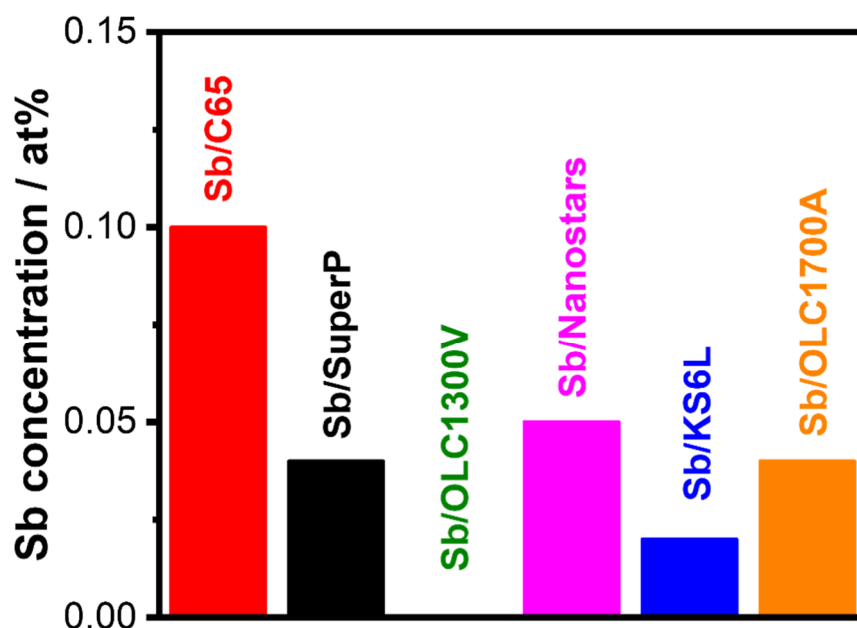


Figure 27. Amounts of metallic Sb in Sb/C electrodes obtained from X-ray photoelectron emission spectroscopy.

We then recorded the X-ray photoelectron emission spectra of the cycled Sb/C composite electrodes for a better understanding of the electrode properties. The XPS data can be seen in Figure 27 and section 10 *Appendix*, Figure A6, and the data are in agreement with the works of Darwiche *et al.*^[62] and Bodenes *et al.*^[79] The SEI layers of all electrodes are composed of the same carbonaceous species in different amounts. C 1s, O 1s, and Sb 3d spectra can be found in section 10 *Appendix*, Figure A6. Figure 27 shows the amount of metallic Sb in the cycled and desodiated electrodes. Metallic Sb is found for each sample except from OLC1300V. XPS is a surface-sensitive technique that only probes about 10 nm of the upper sample layer. Hence, the absence of metallic Sb means that the entire Sb/OLC1300V electrode is covered by a homogeneous SEI during cycling, whereas the other samples exhibit SEI-free parts. Such an observation is in accordance with the SEM illustrations in Figure 26, section 10 *Appendix*, Figure A4 – A5. It is conceivable that the SEI-free parts are in the cracked areas. Most probably, the volume expansion and the resultant electrode cracking leads to bare areas of the electrodes where side reactions take place primarily due to a missing SEI. These effects favor a faster capacity fading of the electrodes.

The presented data demonstrate that the carbon properties are of vital importance for the performance of Sb/C electrodes in a NIB. We also can derive important design guidelines for high-performance Sb/C electrodes. Based on the carbon characteristics (Figure 21), electrochemical studies (Figure 24 – 25), and the subsequent analytics (Figure 26 – 27 and section 10 *Appendix*,

Figure A4 – A5), we were able to elaborate crucial properties of the carbon additives to enable high rate and high stability performance of Sb/C electrodes. The ability to insert sodium counteracts the buffering feature of the carbon, as can be seen for SuperP containing electrodes. The particle morphology should allow good contact between the carbon and the active material. Thus, a round shape as provided by OLCs or SuperP and C65 is preferable to the spikey surface of Nanostars or the large graphite flakes of KS6L. A high pore volume and surface area lead to an enlarged electrode/electrolyte interface. This interface is of high importance as it controls the charge transfer, SEI formation, CE, and stability of the battery.^[180] Further, nanosized carbon can enable high distribution and percolation of the electrode, since it can fill inter-particle voids between the active material particles. We further observe that low graphitization, together with a high amount of impurities is beneficial for improved electrochemical performance. A possible explanation could be that OLC1300V, with its partially disordered structure, can act as a crystallization seed to obtain the special electrode and SEI morphology after cycling (Figure 26d). It is well known that a high number of defects can lead to a homogenous and mechanically more stable SEI.^[63] The Sb/OLC1300V electrode after cycling is covered by a very uniform SEI layer, which supports this hypothesis. Additionally, the absence of cracks indicates that either the volume expansion is effectively buffered or the mechanical stability of the SEI prevents crack formation.

6.3 Influence of morphology and particle size of Sb on the electrochemical performance

6.3.1 Characterization of commercial Sb powder-based samples

The influence of carbon properties on the electrochemical performance was underlined in section 6.2. Nevertheless, the applied Sb nanoparticle synthesis, as well as the production of OLCs, are obstacles for the large scale production. To probe the suitability of commercially available materials, the synthesized Sb powder is replaced by commercial Sb powder (200 mesh) from Alfa Aesar. Additionally, commercial C65 is chosen as a conductive additive in combination with the commercial Sb powder as it has shown the best electrochemical performance in combination with Sb among the other commercial carbons. The commercial Sb powder was applied in the electrodes as obtained, as well as in a ball milled form milled with and without C65.

Commercial antimony powder (Sb-com), ball-milled commercial antimony powder (Sb-com mill) and commercial antimony powder ball milled together with 10 % (w/w) C65 (Sb-com/10C65 mill) were characterized by XRD (Figure 28a – c) and the morphologies are investigated by SEM micrographs in Figure 29a – c. For comparison, XRD patterns and SEM micrographs of the synthesized Sb powder (Sb-syn, section 6.1.1) are illustrated in Figure 28d and Figure 29d.

The reflexes in all refined XRD patterns can be assigned to trigonal Sb with the space group $R\bar{3}m$ (ICSD: 55402) which is the same phase as described for the synthesized Sb powder in section 6.1.1. The Rietveld parameters were obtained for Sb-com: $a = b = 4.3107(9) \text{ \AA}$, $c = 11.2810(5) \text{ \AA}$; $R_p: 11.50$; $R_{wp}: 14.9$, for Sb-com mill: $a = b = 4.3071(9) \text{ \AA}$, $c = 11.2789(6) \text{ \AA}$; $R_p: 8.81$; $R_{wp}: 11.4$ and for Sb-com/10C65 mill: $a = b = 4.2956(3) \text{ \AA}$, $c = 11.2578(7) \text{ \AA}$; $R_p: 5.03$; $R_{wp}: 6.44$. Carbon related signals cannot be detected by XRD due to amorphization during milling. As expected, the broadening of the reflexes indicates that both milled Sb powders exhibit a smaller particle size than the pristine powder. Additionally, if the powder is milled with C65, the particles are even smaller or more amorphous according to the measured reflex width. Nevertheless, this result cannot precisely be confirmed by the SEM images (Figure 29 b – d) due to the high degree of agglomeration.

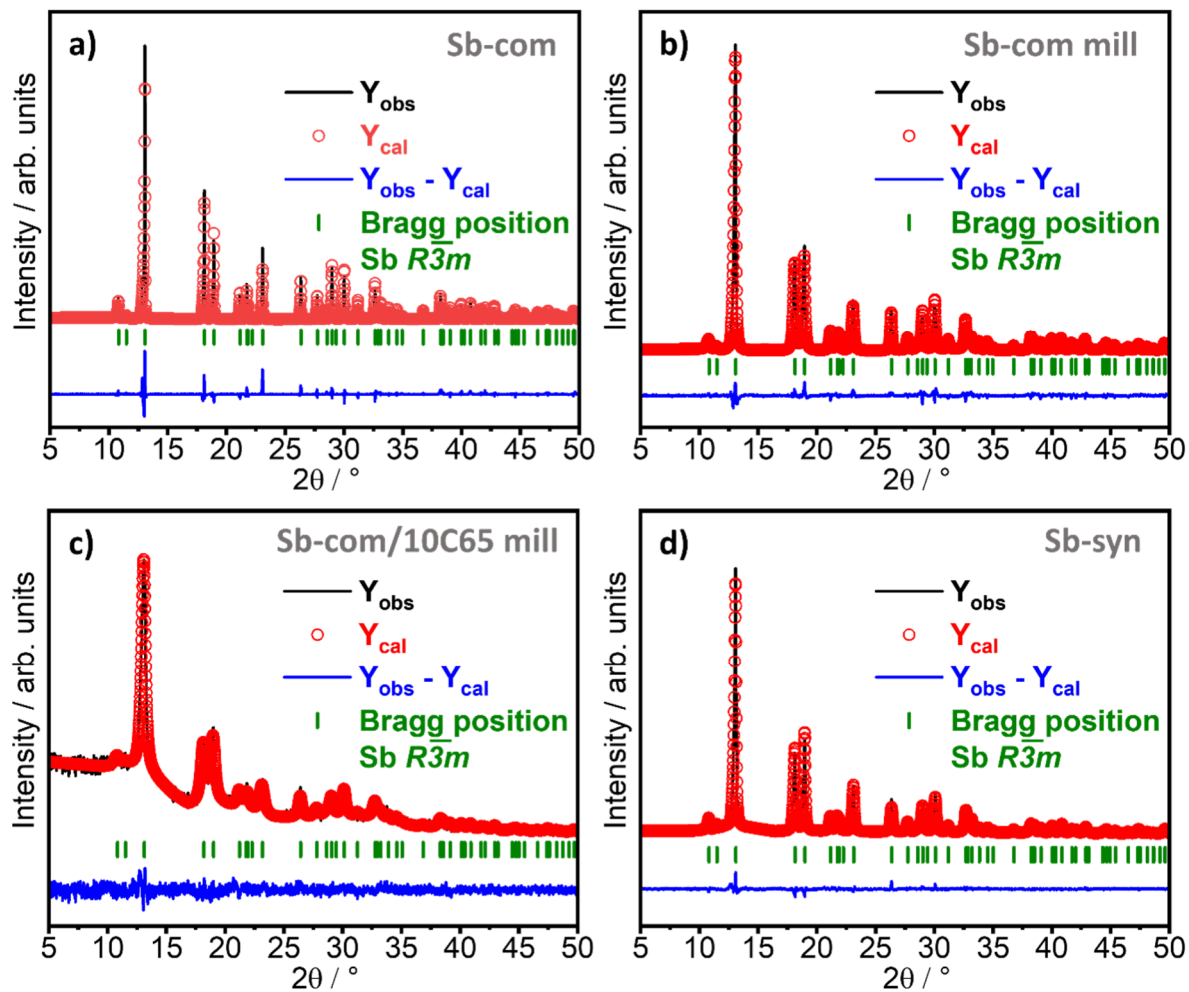


Figure 28. Rietveld-refined diffractograms of a) commercial Sb powder, b) ball milled commercial Sb powder, c) commercial Sb powder milled with 10 % (w/w) C65 and d) synthesized Sb nanopowder.

Yet, the SEM micrographs demonstrate that the commercial Sb powder consists of angular, 10 – 100 μm sized particles (Figure 29a). This morphology transforms into more uniform, round-shaped, 50 – 200 nm sized particles after ball milling (Figure 29b). If C65 is added to Sb before milling, minor carbon nanoparticles are dispersed between the larger (20 – 100 nm-sized) Sb particles (Figure 29c). Despite ball milling of the commercial Sb powder, the synthesized particles appear smaller (10 – 50 nm). The particles of the milled and synthesized powders all exhibit a high degree of agglomeration.

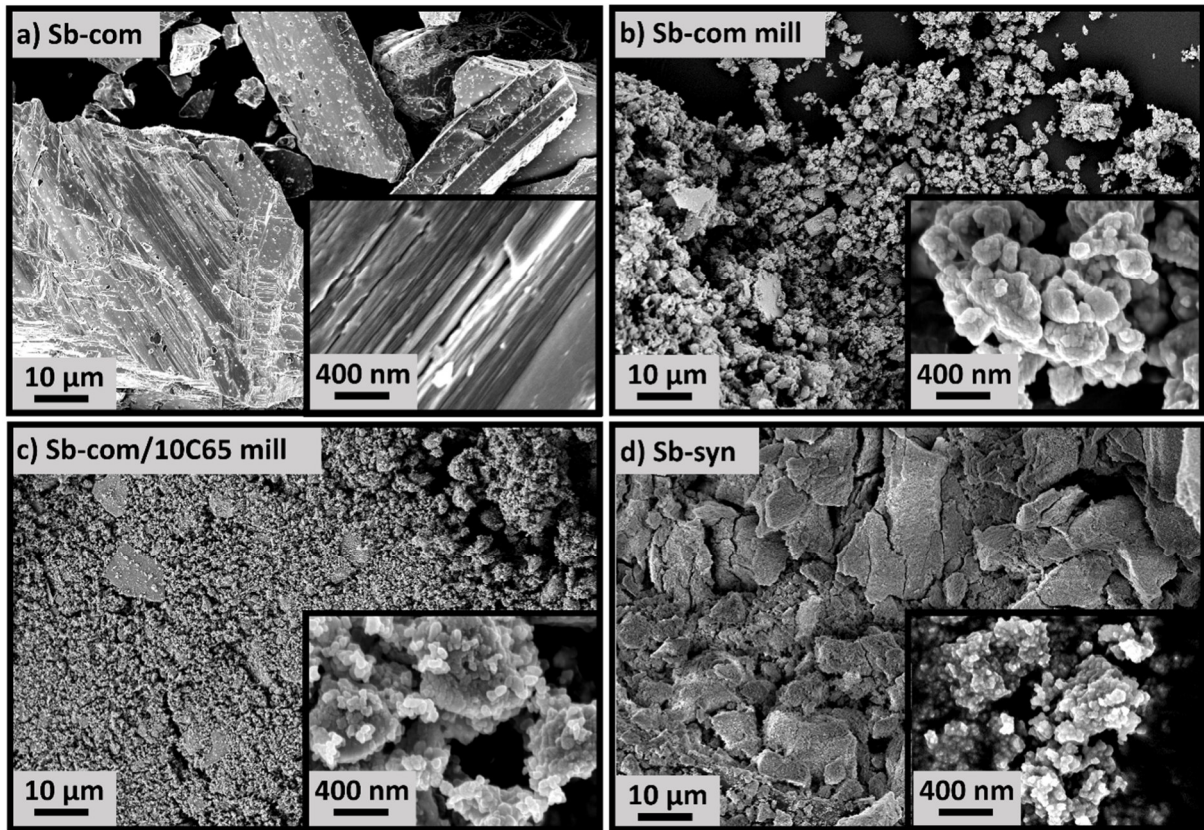


Figure 29. SEM images with high magnification insets of a) commercial Sb powder, b) ball milled commercial Sb powder, c) commercial Sb powder milled with 10 % (w/w) C65 and d) synthesized Sb nanopowder.

6.3.2 Influence of the Sb particle size on Sb/C electrodes based on commercial anti-mony powder

The influence of the carbon amount in Sb based electrodes was investigated in section 6.1.2. 20 % (w/w) C65 in the dry electrode was found to be the optimum quantity. To guarantee comparability with the previous results (section 6.2), the total amount of carbon in this section was adjusted to 20 % of the dry electrode mass for electrochemical measurements. In order to take the carbon content of the Sb-com/10C65 mill powder into account, a ratio of 78% Sb-com/10C65 mill and 12 % C65 was used to produce the respective electrodes. For comparison, the Sb-com/30C65 mill composite was applied in an electrode with a similar Sb/C ratio of 80% Sb-com/30C65 mill, 10 % C65 and 10 % CMC as introduced by Qian *et al.*^[93]. The electrode compositions are listed in Table 3 (section 4.3.1).

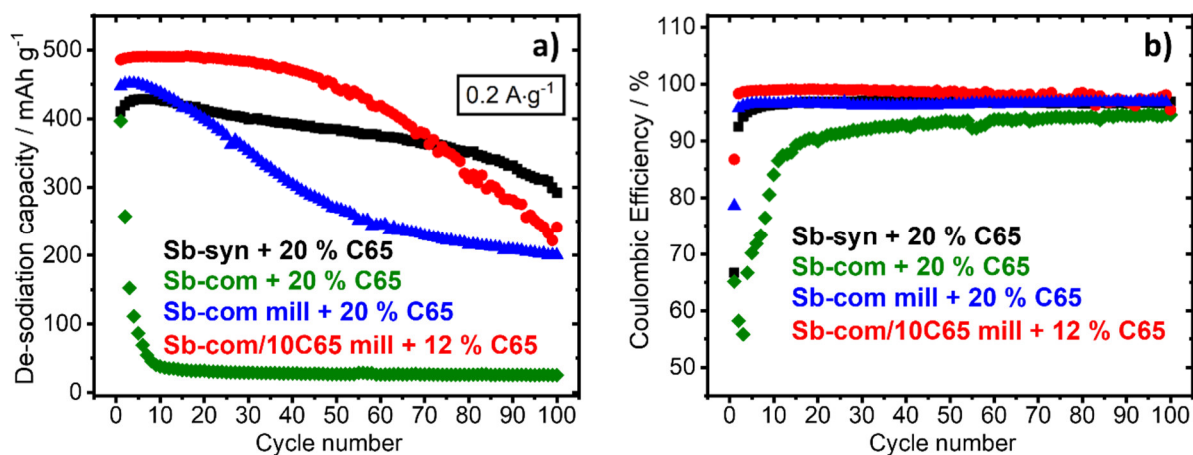


Figure 30. a) Electrochemical cycling stability at 0.2 A g^{-1} and b) Coulombic efficiencies of Sb/C electrodes with different Sb powders and C65.

Figure 30a and b illustrate a comparison of the electrode performance and CE depending on the Sb powder combined with a total amount of 20 % C65 conductive carbon. The corresponding SEM micrographs of the pristine electrodes are given in Figure 31a – d. The electrode fabricated with pristine commercial Sb powder has a capacity retention of only 10 % after 10 cycles. The CE (Figure 30b) remains below 95 %, indicating a high amount of irreversible reactions. This is attributed to the large Sb particle size (Figure 29a) and therefore, a disadvantageous distribution of carbon and Sb, as visualized by the SEM image of the respective pristine electrode (Figure 31b). In this case, the expansion of Sb is most probably insufficiently buffered by the carbon matrix. Therefore, the unmilled Sb bulk powder is not suitable for real application in energy storage systems.

The electrode based on synthesized Sb shows the most stable cycling performance with a capacity retention of 69 % after 100 cycles, whereas the milled commercial Sb based electrode demonstrates a capacity retention of 44 % after 100 cycles. The cycling behavior can be explained by the particle distribution, particle size and the resulting electrode percolation. The synthesized Sb powder and C65 are distributed homogeneously (Figure 31a) and the Sb nanoparticles are relatively homogeneously covered by carbon. The electrode based on milled Sb powder with C65 consists of nanosized and microsized particles embedded in a carbon matrix. Still, a large amount of microsized Sb particles are not covered by carbon. Similar to the unmilled Sb powder, the microsized Sb crystallites are expected to expand to a high degree. The presented C65 matrix would then be incapable to buffer such changes leading to a less stable cycling behavior as compared to the synthesized nanopowder. These detrimental effects are also represented by a decreasing CE.

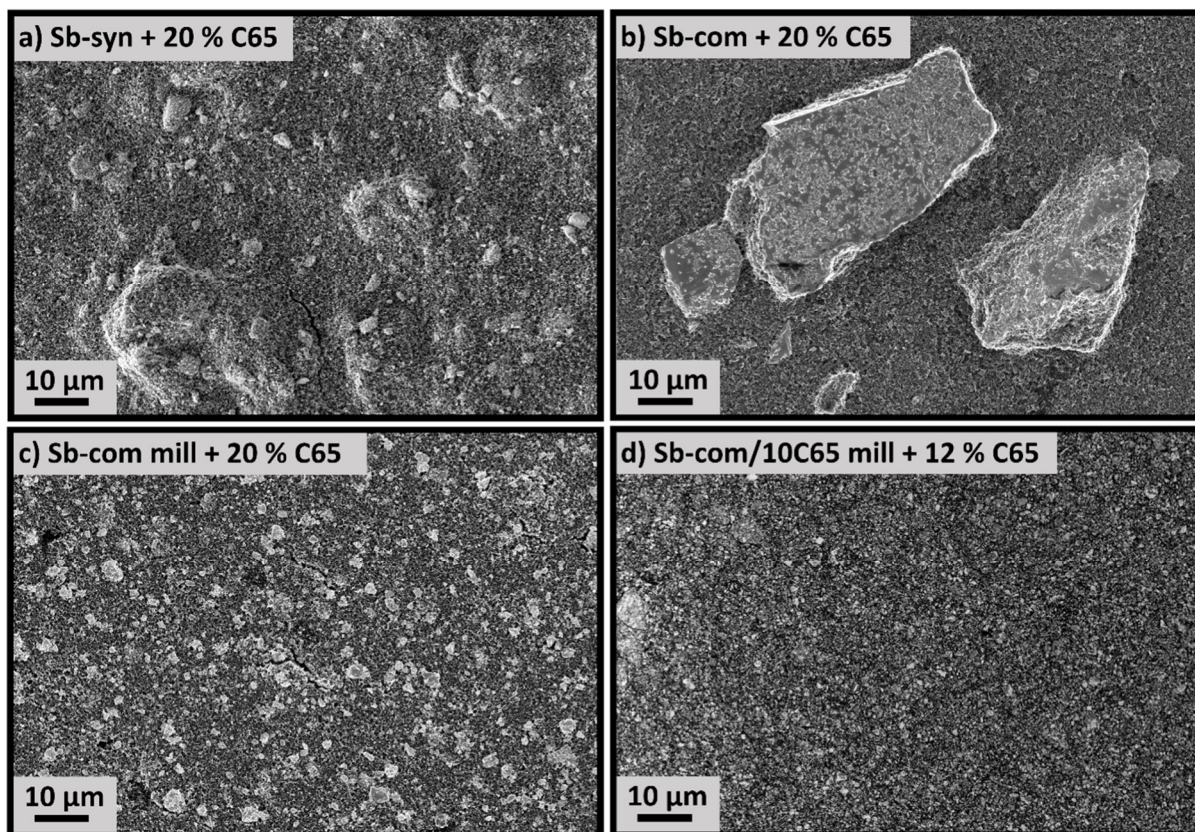


Figure 31. Scanning electron micrographs of pristine electrodes: a) synthesized Sb + 20 % C65, b) commercial Sb + 20 % C65, c) milled commercial Sb + 20 % C65 and d) commercial Sb milled with 10 % C65 and subsequent addition of 12 % C65.

Although the best results were obtained with synthesized Sb powder by simply mixing the ingredients of the electrode, Qian *et al.*^[93] have presented a promising Sb/C composite, which was produced by ball milling of commercial Sb bulk powder and SuperP. To obtain the electrode, the authors added unmilled SuperP to the milled Sb/C composite. The commercial Sb powder applied in this thesis requires a ball milling procedure to enable an acceptable electrochemical activity. The addition of carbon to the ball milling step would thus not complicate the electrode fabrication process. Therefore, Sb/C65 composites in a ratio of 90/10 and 70/30 were prepared by ball milling. An electrode with a total carbon amount of 20 % was prepared with the Sb-com/10C65 mill composite, unmilled C65 and CMC. As discussed before, the cell including the milled commercial Sb powder in combination with unmilled C65 shows a distinct electrochemical activity and decent stability (Figure 30a). Interestingly, the ball milling with C65 with subsequent C65 addition stabilizes the electrode and leads to the highest de-sodiation capacity and best cycling stability among all commercial Sb-based electrodes with 20 % C65. Such an improvement of the electrochemical results can be attributed to the particle distribution and the homogeneity of the electrode (Figure 31d). Similar to the effect described for Sb/OLC1300V (section 6.2.2), the improvement of conductive paths allows a homogenous

charge transfer at the surface of the Sb particles, which can lead to a high de-sodiation capacity. The upgrade in electrode homogeneity is achieved by the addition of C65 prior to the ball-milling process. The corresponding cell delivers the highest CE of 99 % (Figure 30b) and 46 % capacity retention after 100 cycles. The improved stability of the milled Sb/C composite with C65 addition matches the findings of Qian *et al.*^[93] obtained in a similar procedure with SuperP. The slightly lower electrochemical performance of the milled commercial Sb/C composite electrode in this work is related to the amount of applied carbon. While Qian *et al.*^[93] used a ratio of 70/30 for the milled Sb/C composite and a total carbon amount of 34 % (Table 1), a 90/10 ratio and a total carbon amount of 20 % was applied in this work. Therefore, a similar electrode as presented by Qian *et al.*^[93] was fabricated with the milled Sb-com/30C65 mill composite and the cycling performance is shown in Figure A7 (section 10, *Appendix*) for comparison. The stability is improved by 20 % to a capacity retention of 67 % after 100 cycles when enhancing the carbon quantity from 20 % to 34 %. Unfavorably, this stabilization effect is accompanied by a capacity decrease of 28 % due to a lower total Sb amount and a CE decrease of circa 4 % due to the higher amount of carbon. According to Ramireddy *et al.*^[153] and the previous results from section 6.1.2, an enhancement of carbon amount can stabilize the cycling performance of Sb-based electrodes. Furthermore, the smallest nanosized Sb particles have shown the best performance in the study of Ramireddy *et al.*^[153] This is consistent with the overall results of this work, which additionally reveals that different Sb powders need to be combined with different amounts of carbon to obtain comparable cycling stabilities. Therefore, the amount of carbon needs to be individually adjusted for each composite electrode. Moreover, the synthesized Sb nanopowder delivers the highest stability due to the small particle size and its morphology. This offers the best features for a well-distributed system of conductive carbon and Sb particles inside the electrode. Nevertheless, the interplay of commercial carbon and Sb can be improved by mechanical procedures to obtain the smallest possible Sb particles homogeneously blended with carbon. Conclusively, this study exemplifies that commercial materials like bulk Sb and C65 conductive carbon can be applied to obtain Sb/C based electrodes, which deliver a comparable performance to synthesized nanocomposites. Therefore, sophisticated synthesis routes can be avoided, which facilitates the upscaling processes for such electrodes and leads to reduced costs.

6.4 Conclusive aspects: the interplay of antimony and carbon

The focus of this chapter was set on the interactions between Sb and C. It was demonstrated that the carbon mass has to be included in the normalization as carbon additives contribute to the Na⁺ storage. By evaluating different carbonaceous additives, OLC1300V was found to possess the best features to be combined with a synthesized Sb nanopowder leading to a well-distributed system. Additionally, this system involves the benefit of superior SEI layer properties triggered by the OLC1300V characteristics. This leads to outstanding rate performance and a high capacity converging the theoretical value.

Nevertheless, the development of an optimized Sb/C system requires the consideration of both materials. The particle size of Sb plays a crucial role for the homogeneity of the electrode. The smaller the Sb particles, the better the electrochemical stability. Still, it is demonstrated that commercial bulk Sb can be successfully applied as an active material when merged with commercial C65 and finely ground by mechanical mixing. Consequently, individual adjustments of the antimony and carbon components are necessary for high-performance negative electrodes applied in NIBs.

7 Conclusion

The reactivity of sodium metal towards the electrolyte was evaluated by methods for microscopic and macroscopic optical observation. It was shown that a decomposition of the sodium surface and the electrolyte takes place very rapidly even without electrochemical cycling. To analyze the impact of such decomposition effects on the electrochemical performance, the commonly used Na-half-cell set-up was compared to a sodium metal-free half-cell. It was shown that a significant difference in electrochemical stability occurs when comparing sodium-containing half-cells to sodium-free ones. If sodium is used as a counter and reference electrode, a fast decrease of the LTO electrode capacity was determined. A stable behavior of the same working electrode is discovered after replacing sodium electrodes by AC electrodes. Therefore, side reactions drastically impair the stability of sodium-containing half-cells. The occurring instabilities are caused by electrolyte contaminations and their impact on the surface chemistry. Such distortions could lead to wrong conclusions of electrochemical experiments and problems in transferring half-cell results to full cells. Nevertheless, attention should be paid when applying AC electrodes instead of Na. For the evaluation of high-capacity materials, the capacity of AC is too low. Additionally, it is important to have a Na source in the counter electrode to avoid the consumption of Na^+ -ions from the electrolyte. The influence of surface species on AC electrodes can further lead to a shifting potential of the reference electrode. Therefore, an alternative way to maintain Na metal counter and reference electrodes was found in this work. It was demonstrated, that the addition of FEC to organic carbonate-based solvents or the replacement of such solvents by diglyme preserves the Na metal from spontaneous side reactions. Sb_2O_3 was chosen as a model material with a complex charge storage mechanism to evaluate the stability and influence of the electrolyte solvents on all cell components. The electrochemical impact of EC/DMC, EC/DMC + 5 % FEC and diglyme for NIBs was compared. In contrast to FEC additive-free EC/DMC solution, the presence of FEC leads to the formation of thin, compact and probably elastic surface films that passivate the Sb_2O_3 electrodes and avoid their morphological disintegration (e.g., cracking phenomena). Additionally, FEC helps to protect the sodium metal counter and reference electrodes from detrimental side reactions with the electrolyte solution. This leads to > 80 % capacity retention of Sb_2O_3 electrodes after 100 cycles in cells containing Na metal counter electrodes. By contrast, in additive-free electrolyte solutions, the electrodes' capacity is fully lost after 70 cycles and a thick, non-uniform surface layer is formed. This surface layer is composed of degradation products originating from surface reactions of the Na metal electrodes with the electrolyte solution. Considering the diglyme based

solutions, their ability to dissolve Sb based active materials during electrochemical cycling is uncovered. Upon the oxidation of Sb to Sb^{3+} , the ether solvent most probably coordinates and dissolves Sb^{3+} cations. Electrochemical cycling promotes migration and diffusion to the Na metal counter electrode side. This has a detrimental effect on the cell performance, as the dissolved Sb species are deposited on the sodium counter electrode. This situation emphasizes the importance of a proper adjustment of specific characteristics, upon selecting electrolyte solutions for the individual sodium-ion battery system. In this study, the FEC containing electrolyte was found as the best option for further studies on high-capacity electrodes.

Due to the inconsistencies and lacking knowledge of the role of the carbon in composite electrodes with alloy-type materials, a systematic study of six different carbon materials was performed on the basis of the previous findings. The importance of normalization for comparability for carbon-containing composite electrodes was elaborated. All carbonaceous components in an electrode could store sodium-ions. Therefore, the normalization of Sb-based electrodes must include the mass of the entire Sb/C composite.

Further, it is demonstrated that a minimum amount of carbon is necessary to operate Sb-based electrodes. Sb particles are covered by a thin insulating oxide layer, which enhances the electrode resistance and hinders the electrochemical charge storage. Nanosized carbon offers a conductive matrix with embedded Sb particles. For the synthesized Sb nanopowder, it was found that an amount of 20 % (w/w) carbon is sufficient to enable a well-percolated electrode with a stable electrochemical performance. A simple and inexpensive mechanical mixing of the active Sb material, conductive carbon, and the binder solution leads to a comparable electrochemical performance in contrast to complex Sb/C nanocomposite synthesis found elsewhere in the literature.^[38,151,152]

Finally, a basis on which the influence of carbon characteristics was systematically evaluated is provided. By consideration of different carbon morphologies, sizes, amounts of impurities, graphitization, surface areas, pore volumes, and the electrochemical activity of the carbons, an identification of the aspects, which are beneficial and improve the electrochemistry of Sb/C electrodes was possible. If the carbon can insert Na^+ -ions, the connected volume expansion will disrupt the buffering feature and lead to electrode cracking. High purity of the carbon and well-developed graphitization is found to be disadvantageous properties of carbon additives. Disordered carbon areas and heteroatoms were attributed to catalyze the chemical reactions leading to an improved SEI. In addition, nanosized carbon with round-shaped particles is estimated to offer the best percolation of the electrode as it homogeneously covers the agglomerated synthesized Sb nanoparticles. This leads to an improved distribution of the electrical current around

the active material particles, resulting in high conductivity and superior rate performance. Such characteristics were achieved with onion-like carbon synthesized at 1300 °C under vacuum by nanodiamond deposition. Sb/OLC1300V electrodes show virtually no cracks and a very uniform SEI after electrochemical cycling. An Sb/OLC1300V electrode can attain 490 mAh g⁻¹ at 0.1 A g⁻¹ and 300 mAh g⁻¹ at 8 A g⁻¹, which is remarkable when considering the slow reaction kinetics usually associated with alloy materials.^[30,35,150] The optimized conductive paths allow a homogenous charge percolation at the surface of the Sb particle. A large volume of the active particle is sodiated, causing a high de-sodiation capacity and high stability at 0.2 A g⁻¹ over 100 cycles. Compared to the literature given in Table 1 the electrodes in this work exceed most of the literature values if normalized to the Sb mass (630 mAh g⁻¹ at 0.1 A g⁻¹ and 386 mAh g⁻¹ at 8 A g⁻¹). Additionally, a lower amount of carbon (20 %) is used compared to other studies. Therefore, the presented electrodes are able to compete with the results stated in the state-of-the-art-literature, providing simpler processing and fewer carbon amounts in this study.

To further evaluate the influence of the Sb powder characteristics, the synthesized Sb powder was replaced by commercial Sb powder, which was ball milled previous to the electrode preparation. This powder was also tested in combination with C65. As reported by Qian *et al.*^[93] commercial Sb powder shows a stable electrochemical performance when first ball milled with SuperP and subsequently mixed with additional SuperP and the binder component. A similar experiment was conducted with C65 and commercial Sb powder in this work. Most importantly, the role of the Sb particle size is essential: the smaller the particles, the higher the electrochemical stability. This attribute originates from fewer volume changes when considering nanoparticles as well as a better distribution of carbon, which is needed to buffer such volume changes. This study confirms a successful application of commercially available bulk Sb powder and commercial conductive carbon as electrode components for NIBs. However, the bulk powder needs to be ground as fine as possible, which can be realized, for example, by mechanical ball milling. It is also highly important to adjust the interaction of the active material and the carbon in the best possible composition to reach an excellent percolation and electrochemical performance. These findings should serve as important guidelines for the design of high-performance electrodes.

8 Outlook

An important aspect, which was not considered in this work so far, is the different behavior of electrodes in full cell setups compared to their half-cell performance. Numerous studies characterize sodium ion half-cells but the full-cell application, which is a key part of battery research, is commonly not presented. First steps were taken to establish a full-cell setup based on alloy-type Sb to uncover the technological gaps, which need to be closed for a widespread NIB utilization. Commercial Sb milled with C65 was applied as the active material with an Sb/C ratio of 70/30. $\text{Na}_{2/3}\text{Fe}_{1/3}\text{Mn}_{2/3}\text{O}_2$ (NFMO) was proposed as sustainable and promising positive electrode material^[11,181,182] and was therefore synthesized following a route presented in the literature^[11] whereby a pure phase was obtained. A negative electrode with the composition of 80 % Sb-com/30C65 mill, 10 % C65 and 10 % CMC was applied versus a positive electrode consisting of 80 % NFMO, 10 % C65 and 10 % PVdF in a dry electrode mass ratio of $m_{\text{negative electrode}}/m_{\text{positive electrode}} = 0.19$. This balancing was calculated based on irreversible capacities of the electrodes that are not compensated in a 1:1 capacity ratio. The full-cell was cycled in a voltage range of 1.5 V – 4.0 V at different current rates and the related Ragone plot is displayed in Figure 32a. Continuous cycling was performed at 100 mA g^{-1} related to the negative electrode mass (Figure 32b). All values are normalized to the active material mass of both electrodes (binder mass excluded).

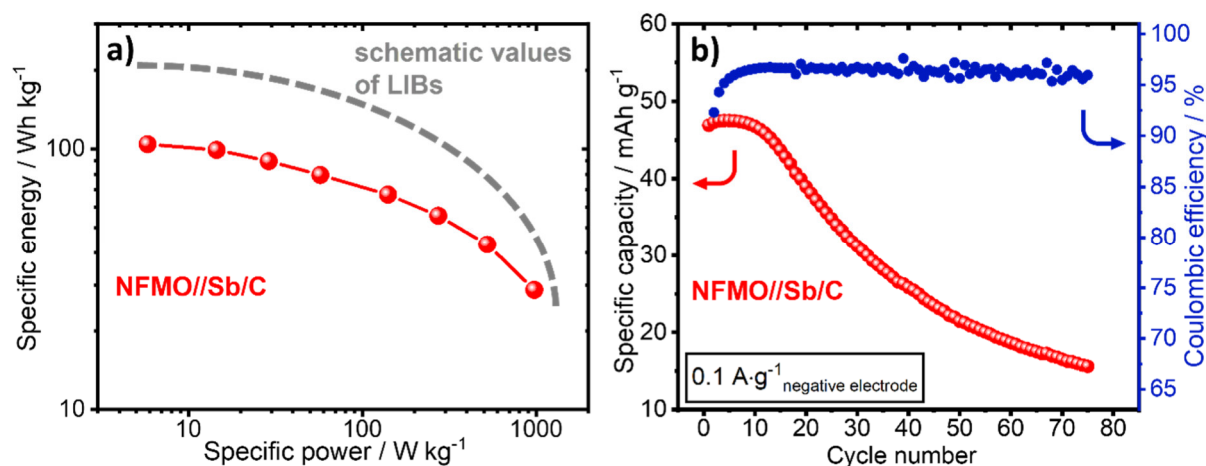


Figure 32. a) Ragone diagram and b) cycling performance of an NFMO//Sb-com/C65 mill + 10 %C65 full-cell cycled between 1.5 V and 4 V. The cell in b) was cycled at a specific current of 0.1 A, which is referred to the negative electrode mass (binder mass excluded). Schematic values of LIBs are adapted from Ref. [183] and indicated by the grey dashed line in a).

The cells were able to deliver a maximum specific energy of 104 Wh kg⁻¹ and a maximum specific power of 976 W kg⁻¹ (Figure 32a). A lower energy density is achieved with this system

when compared to state-of-the-art LIBs, which are schematically indicated by the grey dashed line.^[183] This drawback stems from the higher potential of Na/Na⁺, the higher mass of the ions as compared to Li/Li⁺ and the application of different active materials. Therefore, NIB systems are most suitable for stationary applications where the size of the battery does not play a critical role. The main concern arises from the cycling stability measurement (Figure 32b). The results presented in Figure 32b show that these cells can deliver an initial discharge capacity of 47 mAh g⁻¹ and an initial CE of 66 % with a capacity retention of 44 % after 50 cycles, and a CE of only 95.6 % after 50 cycles. Compared to LIBs with CE's up to 99.99 %^[161] the obtained values in this work are significantly inferior and explain the moderate cycle life when compared to LIBs. The irreversible processes of the alloy material based negative electrode, which are represented by a low CE of < 96 % (Figure A7, section 10 *Appendix*), also affect the positive electrode potential (Figure A8, section 10 *Appendix*). If Na⁺ is constantly consumed by the negative electrode, fewer Na⁺ will be re-inserted into the positive electrode. This leads to distortions of the adjusted balancing during cycling and to a shifting of the positive and negative electrode potential towards higher values (Figure A8, section 10 *Appendix*), which results in low CE values and fast cell degradation. Therefore, especially the first cycle capacity loss of alloy-type materials is an issue which needs to be addressed in future studies.

Additionally, irreversible phase transitions and pulverization during cycling need to be suppressed by further adjustment of the carbon/active material interplay. For this reason, special attention needs to be paid on the electrode design when applying alloy-type materials in NIBs. This should not only be attained by complex active material/carbon hybridization techniques but also by an optimization of the electrode preparation process. At the current state, the use of high capacity materials for NIBs is associated with numerous problems. Nevertheless, the LIB provides a pioneering basis with silicon/graphite composites,^[184–186] which can be adapted in NIB research with the respective materials combinations. For example, hard carbon composites with Sb or Sn can be expected to deliver enhanced capacities in NIBs, similarly to silicon/graphite composites in LIBs.^[184–186] Additionally, the influence of the binder should be studied carefully to design elastic and flexible electrodes appropriate for materials with high volume expansion. Finally, battery researchers should further address the most powerful argument: environmental friendliness. Although NIBs are considered as a sustainable alternative to LIBs, the replacement of lithium by sodium is only a small step towards sustainable batteries. The future focus needs to be placed on the design and simple manufacturability of appropriate non-toxic low-cost electrolytes and materials, economically efficient processes and recyclability to pave the way to sustainable sodium-ion batteries.

9 References

- [1] J.-Y. Hwang, S.-T. Myung, Y.-K. Sun, *Chemical Society Reviews* **2017**, *46*, 3529.
- [2] K. OZAWA, *Solid State Ionics* **1994**, *69*, 212.
- [3] H. Pan, Y.-S. Hu, L. Chen, *Energy Environ. Sci.* **2013**, *6*, 2338.
- [4] D. Larcher, J.-M. Tarascon, *Nature Chemistry* **2015**, *7*, 19.
- [5] J.-M. Tarascon, *Nature Chemistry* **2010**, *2*, 510.
- [6] S. Komaba, W. Murata, T. Ishikawa, N. Yabuuchi, T. Ozeki, T. Nakayama, A. Ogata, K. Gotoh, K. Fujiwara, *Adv. Funct. Mater.* **2011**, *21*, 3859.
- [7] A. Ebensperger, P. Maxwell, C. Moscoso, *Resources Policy* **2005**, *30*, 218.
- [8] D. Kundu, E. Talaie, V. Duffort, L. F. Nazar, *Angewandte Chemie* **2015**, *54*, 3431.
- [9] P. Adelhelm, P. Hartmann, C. L. Bender, M. Busche, C. Eufinger, J. Janek, *Beilstein Journal of Nanotechnology* **2015**, *6*, 1016.
- [10] E. Lee, D. E. Brown, E. E. Alp, Y. Ren, J. Lu, J.-J. Woo, C. S. Johnson, *Chem. Mater.* **2015**, *27*, 6755.
- [11] J. Zhao, J. Xu, D. H. Lee, N. Dimov, Y. S. Meng, S. Okada, *Journal of Power Sources* **2014**, *264*, 235.
- [12] Z. Jian, W. Han, X. Lu, H. Yang, Y.-S. Hu, J. Zhou, Z. Zhou, J. Li, W. Chen, D. Chen, L. Chen, *Adv. Energy Mater.* **2013**, *3*, 156.
- [13] Y. Lu, L. Wang, J. Cheng, J. B. Goodenough, *Chemical Communications* **2012**, *48*, 6544.
- [14] S.-W. Kim, D.-H. Seo, X. Ma, G. Ceder, K. Kang, *Adv. Energy Mater.* **2012**, *2*, 710.
- [15] A. Ponrouch, E. Marchante, M. Courty, J.-M. Tarascon, M. R. Palacín, *Energy Environ. Sci.* **2012**, *5*, 8572.
- [16] M. Dahbi, N. Yabuuchi, K. Kubota, K. Tokiwa, S. Komaba, *Physical Chemistry Chemical Physics PCCP* **2014**, *16*, 15007.

- [17] C. Bommier, X. Ji, *Small* **2018**, *14*, 1703576 (1-20).
- [18] S. Fleischmann, M. Widmaier, A. Schreiber, H. Shim, F. M. Stiemke, T. J.S. Schubert, V. Presser, *Energy Storage Materials* **2019**, *16*, 391.
- [19] J. Ajuria, E. Redondo, M. Arnaiz, R. Mysyk, T. Rojo, E. Goikolea, *Journal of Power Sources* **2017**, *359*, 17.
- [20] G. Hasegawa, K. Kanamori, T. Kiyomura, H. Kurata, K. Nakanishi, T. Abe, *Adv. Energy Mater.* **2015**, *5*, 1400730.
- [21] W. Sun, X. Rui, J. Zhu, L. Yu, Y. Zhang, Z. Xu, S. Madhavi, Q. Yan, *Journal of Power Sources* **2015**, *274*, 755.
- [22] D. I. Iermakova, R. Dugas, M. R. Palacín, A. Ponrouch, *J. Electrochem. Soc.* **2015**, *162*, A7060.
- [23] R. Yazami, P. Touzain, *International Meeting on Lithium Batteries, Roma* **1982**, Abstract No. 23.
- [24] R. Yazami, P. Touzain, *Journal of Power Sources* **1983**, *9*, 365.
- [25] P. K. Nayak, L. Yang, W. Brehm, P. Adelhelm, *Angew. Chem. Int. Ed.* **2018**, *57*, 102.
- [26] DiVincenzo, Mele, *Physical review. B, Condensed matter* **1985**, *32*, 2538.
- [27] E. Irisarri, A. Ponrouch, M. R. Palacin, *J. Electrochem. Soc.* **2015**, *162*, A2476.
- [28] M.-S. Balogun, Y. Luo, W. Qiu, P. Liu, Y. Tong, *Carbon* **2016**, *98*, 162.
- [29] E. Edison, S. Sreejith, C. T. Lim, S. Madhavi, *Sustainable Energy Fuels* **2018**, *2*, 2567.
- [30] M. Lao, Y. Zhang, W. Luo, Q. Yan, W. Sun, S. X. Dou, *Advanced Materials* **2017**, *29*, 1700622.
- [31] W. Brehm, J. R. Buchheim, P. Adelhelm, *Energy Technol.* **2019**, *7*, 1900389.
- [32] V. L. Chevrier, G. Ceder, *J. Electrochem. Soc.* **2011**, *158*, A1011.
- [33] M. Widmaier, N. Jäckel, M. Zeiger, M. Abuzarli, C. Engel, L. Bommer, V. Presser, *Electrochimica Acta* **2017**, *247*, 1006.
- [34] M. Widmaier, K. Pfeifer, L. Bommer, V. Presser, *Batteries & Supercaps* **2018**, *1*, 11.

- [35] H. Hou, M. Jing, Y. Yang, Y. Zhang, W. Song, X. Yang, J. Chen, Q. Chen, X. Ji, *Journal of Power Sources* **2015**, *284*, 227.
- [36] C. Cui, J. Xu, Y. Zhang, Z. Wei, M. Mao, X. Lian, S. Wang, C. Yang, X. Fan, J. Ma, C. Wang, *Nano letters* **2019**, *19*, 538.
- [37] L. Wu, X. Hu, J. Qian, F. Pei, F. Wu, R. Mao, X. Ai, H. Yang, Y. Cao, *Energy Environ. Sci.* **2014**, *7*, 323.
- [38] Y. Zhu, X. Han, Y. Xu, Y. Liu, S. Zheng, K. Xu, L. Hu, C. Wang, *ACS nano* **2013**, *7*, 6378.
- [39] C. Li, A. Sarapulova, K. Pfeifer, S. Dsoke, *ChemSusChem* **2020**, *13*, 986.
- [40] A. Darwiche, C. Marino, M. T. Sougrati, B. Fraisse, L. Stievano, L. Monconduit, *Journal of the American Chemical Society* **2012**, *134*, 20805.
- [41] N. Eliaz, E. Gileadi, *Physical electrochemistry: Fundamentals, Techniques and Applications*, Wiley-VCH, Weinheim **2019**, *2nd ed.*, p 5.
- [42] M. Widmaier, B. Krüner, N. Jäckel, M. Aslan, S. Fleischmann, C. Engel, V. Presser, *J. Electrochem. Soc.* **2016**, *163*, A2956.
- [43] A. J. Bard, L. R. Faulkner, *Electrochemical Methods: Fundamentals and Applications*, John Wiley & Sons, Inc, Hoboken, NJ **2001**, *2nd ed.*, p 53.
- [44] D. Weingarth, A. Foelske-Schmitz, A. Wokaun, R. Kötz, *Electrochemistry Communications* **2012**, *18*, 116.
- [45] T. B. Reddy, D. Linden (Eds.), *Linden's handbook of batteries*, McGraw-Hill, New York, NY **2011**, *4th ed.*, p B1.
- [46] M. Faraday, *Phil. Trans. R. Soc.* **1834**, *124*, 77.
- [47] V. S. Bagockii, A. S. Skundin, Y. V. Volkovich, *Electrochemical Power Sources: Batteries, Fuel Cells, and Supercapacitors*, Wiley, Hoboken, New Jersey **2015**, *1st ed.*, p 32.
- [48] J. Lee, P. Srimuk, S. Fleischmann, X. Su, T. A. Hatton, V. Presser, *Progress in Materials Science* **2019**, *101*, 46.

- [49] M. Sillanpää, M. Shestakova, X. Alameda-Pineda, *Electrochemical Water Treatment Methods: Fundamentals, Methods and Full Scale Applications*, Elsevier Science & Technology, Oxford **2017**, 1st ed., p 95.
- [50] N. Omar, M. Daowd, P. van den Bossche, O. Hegazy, J. Smekens, T. Coosemans, J. van Mierlo, *Energies* **2012**, 5, 2952.
- [51] M. R. Palacín, *Chemical Society Reviews* **2009**, 38, 2565.
- [52] B. Scrosati, *J. Electrochem. Soc.* **1992**, 139, 2776.
- [53] P. Kurzweil, O. K. Dietlmeier, *Elektrochemische Speicher: Superkondensatoren, Batterien, Elektrolyse-Wasserstoff, Rechtliche Grundlagen*, Springer Fachmedien Wiesbaden, Wiesbaden **2015**, 1st ed., p 157.
- [54] P. Simon, Y. Gogotsi, B. Dunn, *Science* **2014**, 343, 1210.
- [55] M. D. Slater, D. Kim, E. Lee, C. S. Johnson, *Adv. Funct. Mater.* **2013**, 23, 947.
- [56] K. Pfeifer, S. Arnold, J. Becherer, C. Das, J. Maibach, H. Ehrenberg, S. Dsoke, *ChemSusChem* **2019**, 12, 3312.
- [57] X. Yu, H. Yang, H. Meng, Y. Sun, J. Zheng, D. Ma, X. Xu, *ACS Applied Materials & Interfaces* **2015**, 7, 15961.
- [58] H. Zheng, R. Yang, G. Liu, X. Song, V. S. Battaglia, *J. Phys. Chem. C* **2012**, 116, 4875.
- [59] K. Pfeifer, S. Arnold, Ö. Budak, X. Luo, V. Presser, H. Ehrenberg, S. Dsoke, *J. Mater. Chem. A* **2020**, 8, 6092.
- [60] M. E. Spahr, D. Goers, A. Leone, S. Stallone, E. Grivei, *Journal of Power Sources* **2011**, 196, 3404.
- [61] E. Peled, *J. Electrochem. Soc.* **1979**, 126, 2047.
- [62] A. Darwiche, L. Bodenes, L. Madec, L. Monconduit, H. Martinez, *Electrochimica Acta* **2016**, 207, 284.
- [63] P. Verma, P. Maire, P. Novák, *Electrochimica Acta* **2010**, 55, 6332.
- [64] L. Bodenes, A. Darwiche, L. Monconduit, H. Martinez, *Journal of Power Sources* **2015**, 273, 14.

- [65] M. Winter, J. O. Besenhard, M. E. Spahr, P. Novák, *Adv. Mater.* **1998**, *10*, 725.
- [66] C. Fang, Y. Huang, W. Zhang, J. Han, Z. Deng, Y. Cao, H. Yang, *Adv. Energy Mater.* **2016**, *6*, 1501727.
- [67] F. Klein, B. Jache, A. Bhide, P. Adelhelm, *Physical Chemistry Chemical Physics PCCP* **2013**, *15*, 15876.
- [68] K. Chayambuka, G. Mulder, D. L. Danilov, P. H. L. Notten, *Adv. Energy Mater.* **2018**, *8*, 1800079.
- [69] P. Senguttuvan, G. Rouse, V. Seznec, J.-M. Tarascon, M.R. Palacín, *Chem. Mater.* **2011**, *23*, 4109.
- [70] Y. Sun, L. Zhao, H. Pan, X. Lu, L. Gu, Y.-S. Hu, H. Li, M. Armand, Y. Ikuhara, L. Chen, X. Huang, *Nature Communications* **2013**, *4*, 1870.
- [71] B. L. Ellis, L. F. Nazar, *Current Opinion in Solid State and Materials Science* **2012**, *16*, 168.
- [72] D. A. Stevens, J. R. Dahn, *J. Electrochem. Soc.* **2001**, *148*, A803.
- [73] D. A. Stevens, J. R. Dahn, *J. Electrochem. Soc.* **2000**, *147*, 1271.
- [74] R. E. Franklin, *Proc. R. Soc. Lond. A* **1951**, *209*, 196.
- [75] J. R. Dahn, W. Xing, Y. Gao, *Carbon* **1997**, *35*, 825.
- [76] P.-c. Tsai, S.-C. Chung, S.-k. Lin, A. Yamada, *J. Mater. Chem. A* **2015**, *3*, 9763.
- [77] H. Gao, T. Zhou, Y. Zheng, Y. Liu, J. Chen, H. Liu, Z. Guo, *Adv. Energy Mater.* **2016**, *6*, 1601037.
- [78] J. A. Young, *J. Chem. Educ.* **2004**, *81*, 945.
- [79] L. Bodenes, A. Darwiche, L. Monconduit, H. Martinez, *Journal of Power Sources* **2015**, *273*, 14.
- [80] L. Ji, M. Gu, Y. Shao, X. Li, M. H. Engelhard, B. W. Arey, W. Wang, Z. Nie, J. Xiao, C. Wang, J.-G. Zhang, J. Liu, *Advanced Materials* **2014**, *26*, 2901.

- [81] S. Komaba, T. Ishikawa, N. Yabuuchi, W. Murata, A. Ito, Y. Ohsawa, *ACS Applied Materials & Interfaces* **2011**, *3*, 4165.
- [82] V. Winkler, G. Kilibarda, S. Schlabach, D. V. Szabó, T. Hanemann, M. Bruns, *J. Phys. Chem. C* **2016**, *120*, 24706.
- [83] M. Hu, Y. Jiang, W. Sun, H. Wang, C. Jin, M. Yan, *ACS Applied Materials & Interfaces* **2014**, *6*, 19449.
- [84] D. Su, H.-J. Ahn, G. Wang, *Chemical Communications* **2013**, *49*, 3131.
- [85] R. Malini, U. Uma, T. Sheela, M. Ganesan, N. G. Renganathan, *Ionics* **2009**, *15*, 301.
- [86] O. Delmer, P. Balaya, L. Kienle, J. Maier, *Adv. Mater.* **2008**, *20*, 501.
- [87] Z. Lyu, L. Yang, D. Xu, J. Zhao, H. Lai, Y. Jiang, Q. Wu, Y. Li, X. Wang, Z. Hu, *Nano Res.* **2015**, *8*, 3535.
- [88] Y. Liu, X. Cai, W. Shi, *Materials Letters* **2016**, *172*, 72.
- [89] K. Wang, Z. Li, Y. Wang, H. Liu, J. Chen, J. Holmes, H. Zhou, *J. Mater. Chem.* **2010**, *20*, 9748.
- [90] J. Qian, X. Wu, Y. Cao, X. Ai, H. Yang, *Angew. Chem.* **2013**, *125*, 4731.
- [91] W. Chen, D. Deng, *ACS Sustainable Chem. Eng.* **2015**, *3*, 63.
- [92] C. Wu, P. I. Pan, Y. Cheng, C. Liu, C. Chang, M. Avdeev, S. Lin, *Journal of Power Sources* **2017**, *340*, 14.
- [93] J. Qian, Y. Chen, L. Wu, Y. Cao, X. Ai, H. Yang, *Chemical Communications* **2012**, *48*, 7070.
- [94] J. Syzdek, M. Marcinek, R. KostECKI, *Journal of Power Sources* **2014**, *245*, 739.
- [95] A. Rezqita, R. Hamid, S. Schwarz, H. Kronberger, A. Trifonova, *ECS Transactions* **2015**, *66*, 17.
- [96] J. Xiao, W. Xu, D. Wang, D. Choi, W. Wang, X. Li, G. L. Graff, J. Liu, J. G. Zhang, *J. Electrochem. Soc.* **2010**, *157*, A1047.

- [97] M. Nádherná, J. Reiter, J. Moškón, R. Dominko, *Journal of Power Sources* **2011**, *196*, 7700.
- [98] S. Rothermel, P. Meister, G. Schmuelling, O. Fromm, H.-W. Meyer, S. Nowak, M. Winter, T. Placke, *Energy Environ. Sci.* **2014**, *7*, 3412.
- [99] M. Indrikova, S. Grunwald, F. Golks, A. Netz, B. Westphal, *J. Electrochem. Soc.* **2015**, *162*, A2021.
- [100] D. D. L. Chung, *J Mater Sci* **2002**, *37*, 1475.
- [101] J. D. Bernal, *Proc. R. Soc. Lond. A* **1924**, *106*, 749.
- [102] A. Yoshino, *Angewandte Chemie* **2012**, *51*, 5798.
- [103] Y. Nishi, *Interface Magazine* **2016**, *25*, 71.
- [104] D. Weingarth, D. Cericola, F.C.F. Mornaghini, T. Hucke, R. Kötz, *Journal of Power Sources* **2014**, *266*, 475.
- [105] W. Wu, J. Yan, A. Wise, A. Rutt, J. F. Whitacre, *J. Electrochem. Soc.* **2014**, *161*, A561.
- [106] M. Li, R. Carter, L. Oakes, A. Douglas, N. Muralidharan, C. L. Pint, *J. Mater. Chem. A* **2017**, *5*, 5266.
- [107] T. Murakami, K. Ajima, J. Miyawaki, M. Yudasaka, S. Iijima, K. Shiba, *Mol. Pharmaceutics* **2004**, *1*, 399.
- [108] C.-M. Yang, H. Noguchi, K. Murata, M. Yudasaka, A. Hashimoto, S. Iijima, K. Kaneko, *Adv. Mater.* **2005**, *17*, 866.
- [109] S. Utsumi, J. Miyawaki, H. Tanaka, Y. Hattori, T. Itoi, N. Ichikuni, H. Kanoh, M. Yudasaka, S. Iijima, K. Kaneko, *The Journal of Physical Chemistry. B* **2005**, *109*, 14319.
- [110] R. Yuge, T. Ichihashi, Y. Shimakawa, Y. Kubo, M. Yudasaka, S. Iijima, *Adv. Mater.* **2004**, *16*, 1420.
- [111] H. Lai, J. Li, Z. Chen, Z. Huang, *ACS Applied Materials & Interfaces* **2012**, *4*, 2325.
- [112] W. Xu, Z. Wang, Z. Guo, Y. Liu, N. Zhou, B. Niu, Z. Shi, H. Zhang, *Journal of Power Sources* **2013**, *232*, 193.

- [113] C.-M. Yang, Y.-J. Kim, M. Endo, H. Kanoh, M. Yudasaka, S. Iijima, K. Kaneko, *Journal of the American Chemical Society* **2007**, *129*, 20.
- [114] R. Yuge, N. Tamura, T. Manako, K. Nakano, K. Nakahara, *Journal of Power Sources* **2014**, *266*, 471.
- [115] Y. Zhao, J. Li, Y. Ding, L. Guan, *RSC Adv.* **2011**, *1*, 852.
- [116] Y. Zhao, J. Li, Y. Ding, L. Guan, *Chemical Communications* **2011**, *47*, 7416.
- [117] M. Zeiger, N. Jäckel, V. N. Mochalin, V. Presser, *J. Mater. Chem. A* **2016**, *4*, 3172.
- [118] V. L. Kuznetsov, A. L. Chuvilin, Y. V. Butenko, I. Y. Malkov, V. M. Titov, *Chemical Physics Letters* **1994**.
- [119] J. K. McDonough, Y. Gogotsi, *J. Electrochem. Soc., Interface* **2013**, *22*, 61.
- [120] M. Zeiger, N. Jäckel, D. Weingarth, V. Presser, *Carbon* **2015**, *94*, 507.
- [121] N. Jäckel, D. Weingarth, M. Zeiger, M. Aslan, I. Grobelsek, V. Presser, *Journal of Power Sources* **2014**, *272*, 1122.
- [122] D. Pech, M. Brunet, H. Durou, P. Huang, V. Mochalin, Y. Gogotsi, P.-L. Taberna, P. Simon, *Nature nanotechnology* **2010**, *5*, 651.
- [123] Z. Zheng, Q. Su, Q. Zhang, H. Ye, Z. Wang, *J Mater Sci* **2018**, *53*, 12421.
- [124] A. Ponrouch, R. Dedryvère, D. Monti, A. E. Demet, J. M. Ateba Mba, L. Croguennec, C. Masquelier, P. Johansson, M. R. Palacín, *Energy Environ. Sci.* **2013**, *6*, 2361.
- [125] S. Komaba, Y. Matsuura, T. Ishikawa, N. Yabuuchi, W. Murata, S. Kuze, *Electrochemistry Communications* **2012**, *21*, 65.
- [126] H. Lu, L. Wu, L. Xiao, X. Ai, H. Yang, Y. Cao, *Electrochimica Acta* **2016**, *190*, 402.
- [127] K. Li, J. Zhang, D. Lin, D.-W. Wang, B. Li, W. Lv, S. Sun, Y.-B. He, F. Kang, Q.-H. Yang, L. Zhou, T.-Y. Zhang, *Nature Communications* **2019**, *10*, 725.
- [128] K. Westman, R. Dugas, P. Jankowski, W. Wiecek, G. Gachot, M. Morcrette, E. Irisarri, A. Ponrouch, M. R. Palacín, J.-M. Tarascon, P. Johansson, *ACS Appl. Energy Mater.* **2018**, *1*, 2671.

- [129] X. Liu, B. Qin, H. Zhang, A. Moretti, S. Passerini, *ACS Appl. Energy Mater.* **2019**, *2*, 2786.
- [130] R. Alcántara, P. Lavela, G. F. Ortiz, J. L. Tirado, *Electrochem. Solid-State Lett.* **2005**, *8*, A222.
- [131] D. Hamani, M. Ati, J.-M. Tarascon, P. Rozier, *Electrochemistry Communications* **2011**, *13*, 938.
- [132] P. Vassilaras, X. Ma, X. Li, G. Ceder, *J. Electrochem. Soc.* **2013**, *160*, A207-A211.
- [133] N. Yabuuchi, K. Kubota, M. Dahbi, S. Komaba, *Chemical Reviews* **2014**, *114*, 11636.
- [134] V. Palomares, P. Serras, I. Villaluenga, K. B. Hueso, J. Carretero-González, T. Rojo, *Energy Environ. Sci.* **2012**, *5*, 5884.
- [135] J. Barker, M. Y. Saidi, J. L. Swoyer, *Electrochem. Solid-State Lett.* **2003**, *6*, A53.
- [136] M. Zarrabeitia, M. Muñoz-Márquez, F. Nobili, T. Rojo, M. Casas-Cabanas, *Batteries* **2017**, *3*, 16.
- [137] J. Conder, C. Villevieille, *Chemical Communications* **2019**, *55*, 1275.
- [138] P. W. Ruch, D. Cericola, M. Hahn, R. Kötz, A. Wokaun, *Journal of Electroanalytical Chemistry* **2009**, *636*, 128.
- [139] M. Arnaiz, J. L. Gómez-Cámer, J. Ajuria, F. Bonilla, B. Acebedo, M. Jáuregui, E. Goikolea, M. Galceran, T. Rojo, *Chem. Mater.* **2018**, *30*, 8155.
- [140] J. Lee, N. Jäckel, D. Kim, M. Widmaier, S. Sathyamoorthi, P. Srimuk, C. Kim, S. Fleischmann, M. Zeiger, V. Presser, *Electrochimica Acta* **2016**, *222*, 1800.
- [141] S. Fleischmann, K. Pfeifer, M. Widmaier, H. Shim, Ö. Budak, V. Presser, *ACS Appl. Energy Mater.* **2019**, *2*, 3633.
- [142] N. Mozhzhukhina, E. J. Calvo, *J. Electrochem. Soc.* **2017**, *164*, A2295.
- [143] D. Stępień, Z. Zhao, S. Dsoke, *J. Electrochem. Soc.* **2018**, *165*, A2807.
- [144] Ding Z., Trouillet V., Dsoke S., *J. Electrochem. Soc.* **2019**, *166*, A1004.

- [145] A. González, E. Goikolea, J. A. Barrena, R. Mysyk, *Renewable and Sustainable Energy Reviews* **2016**, *58*, 1189.
- [146] G. Wang, L. Zhang, J. Zhang, *Chemical Society Reviews* **2012**, *41*, 797.
- [147] X. Yu, H. Pan, W. Wan, C. Ma, J. Bai, Q. Meng, S. N. Ehrlich, Y.-S. Hu, X.-Q. Yang, *Nano Letters* **2013**, *13*, 4721.
- [148] M. Han, C. Zhu, T. Ma, Z. Pan, Z. Tao, J. Chen, *Chemical Communications* **2018**, *54*, 2381.
- [149] K. Kubota, S. Komaba, *J. Electrochem. Soc.* **2015**, *162*, A2538.
- [150] L. Wu, H. Lu, L. Xiao, X. Ai, H. Yang, Y. Cao, *J. Mater. Chem. A* **2015**, *3*, 5708.
- [151] X. Zhou, Z. Dai, J. Bao, Y.-G. Guo, *J. Mater. Chem. A* **2013**, *1*, 13727.
- [152] H. Hou, Y. Yang, Y. Zhu, M. Jing, C. Pan, L. Fang, W. Song, X. Yang, X. Ji, *Electrochimica Acta* **2014**, *146*, 328.
- [153] T. Ramireddy, N. Sharma, T. Xing, Y. Chen, J. Leforestier, A. M. Glushenkov, *ACS Applied Materials & Interfaces* **2016**, *8*, 30152.
- [154] D. Weingarth, M. Zeiger, N. Jäckel, M. Aslan, G. Feng, V. Presser, *Adv. Energy Mater.* **2014**, *4*, 1400316.
- [155] K. L. Parry, A. G. Shard, R. D. Short, R. G. White, J. D. Whittle, A. Wright, *Surf. Interface Anal.* **2006**, *38*, 1497.
- [156] C. M. A. Brett, A. M. O. Brett, *Electrochemistry: Principles, Methods, And Applications*, Oxford University Press **1993**, *1*, p 224.
- [157] S. Klink, E. Madej, E. Ventosa, A. Lindner, W. Schuhmann, F. La Mantia, *Electrochemistry Communications* **2012**, *22*, 120.
- [158] J. Song, *Journal of Power Sources* **2002**, *111*, 255.
- [159] F. Zhao, P. Xue, H. Ge, L. Li, B. Wang, *J. Electrochem. Soc.* **2016**, *163*, A690.
- [160] L. Y. Yang, H. Z. Li, J. Liu, S. S. Tang, Y. K. Lu, S. T. Li, J. Min, N. Yan, M. Lei, *J. Mater. Chem. A* **2015**, *3*, 24446.

- [161] A. J. Smith, J. C. Burns, S. Trussler, J. R. Dahn, *J. Electrochem. Soc.* **2010**, *157*, A196.
- [162] B. Gyenes, D. A. Stevens, V. L. Chevrier, J. R. Dahn, *J. Electrochem. Soc.* **2015**, *162*, A278.
- [163] S. Komaba, T. Ishikawa, N. Yabuuchi, W. Murata, A. Ito, Y. Ohsawa, *ACS Applied Materials & Interfaces* **2011**, *3*, 4165.
- [164] J. Wang, Y. Bai, M. Wu, J. Yin, W. F. Zhang, *Journal of Power Sources* **2009**, *191*, 614.
- [165] W. Shen, Z. Li, Y. Liu, *CHENG* **2008**, *1*, 27.
- [166] Y. Zhang, X. Li, J. Huang, W. Xing, Z. Yan, *Nanoscale research letters* **2016**, *11*, 163.
- [167] S. Ghosh, S. Mitra, P. Barpanda, *Electrochimica Acta* **2016**, *222*, 898.
- [168] B. Philippe, M. Valvo, F. Lindgren, H. Rensmo, K. Edström, *Chem. Mater.* **2014**, *26*, 5028.
- [169] T. Sultana, G. L. Georgiev, G. Auner, G. Newaz, H. J. Herfurth, R. Patwa, *Applied Surface Science* **2008**, *255*, 2569.
- [170] M. Dahbi, T. Nakano, N. Yabuuchi, T. Ishikawa, K. Kubota, M. Fukunishi, S. Shibahara, J.-Y. Son, Y.-T. Cui, H. Oji, S. Komaba, *Electrochemistry Communications* **2014**, *44*, 66.
- [171] K. Pfeifer, M. F. Greenstein, D. Aurbach, X. Luo, H. Ehrenberg, S. Dsoke, *ChemElectroChem* **2020**, *7*, 3487.
- [172] R. Dugas, A. Ponrouch, G. Gachot, R. David, M. R. Palacin, J. M. Tarascon, *J. Electrochem. Soc.* **2016**, *163*, A2333.
- [173] S. S. Zhang, *Journal of Power Sources* **2006**, *162*, 1379.
- [174] Hideko Koshima, Hiroshi Onishi, *Analyst* **1986**, *111*, 1261.
- [175] Brian Beagley, Monica Endregard, David G. Nicholson, *Acta Chemica Scandinavica* **1991**, *45*, 349.

- [176] A. C. Ferrari, *Solid State Communications* **2007**, *143*, 47.
- [177] A. C. Ferrari, J. Robertson, *Physical Review B* **2000**, *61*, 14095.
- [178] L. Borchardt, M. Oschatz, M. Lohe, V. Presser, Y. Gogotsi, S. Kaskel, *Carbon* **2012**, *50*, 3987.
- [179] C. W. Wang, K. A. Cook, A. M. Sastry, *J. Electrochem. Soc.* **2003**, *150*, A385.
- [180] M. Gauthier, T. J. Carney, A. Grimaud, L. Giordano, N. Pour, H.-H. Chang, D. P. Fenning, S. F. Lux, O. Paschos, C. Bauer, F. Maglia, S. Lupart, P. Lamp, Y. Shao-Horn, *The Journal of Physical Chemistry Letters* **2015**, *6*, 4653.
- [181] T.-Y. Chen, B. Han, C.-W. Hu, Y.-F. Su, Y.-X. Zhou, H.-Y. Chen, P.-I. Pan, C.-M. Wu, A. Hu, J.-J. Kai, Y.-D. Juang, C.-C. Chang, *J. Phys. Chem. C* **2018**, *122*, 12623.
- [182] M. J. Aragón, P. Lavela, G. Ortiz, R. Alcántara, J. L. Tirado, *Journal of Alloys and Compounds* **2017**, *724*, 465.
- [183] B. D. McCloskey, *The Journal of Physical Chemistry Letters* **2015**, *6*, 3592.
- [184] N. Dimov, S. Kugino, M. Yoshio, *Journal of Power Sources* **2004**, *136*, 108.
- [185] B. Fuchsbichler, C. Stangl, H. Kren, F. Uhlig, S. Koller, *Journal of Power Sources* **2011**, *196*, 2889.
- [186] M. Yoshio, T. Tsumura, N. Dimov, *Journal of Power Sources* **2006**, *163*, 215.

10 Appendix

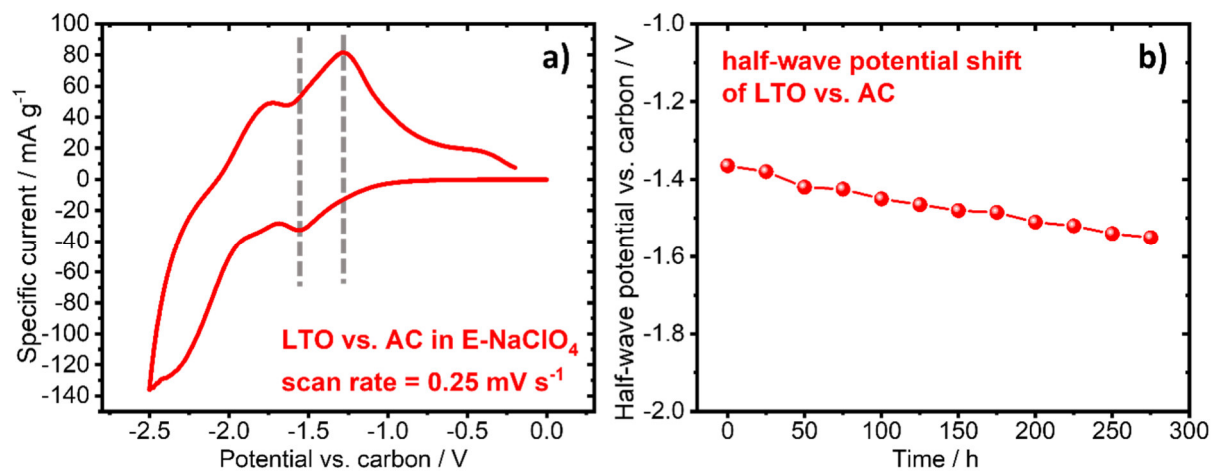


Figure A1. a) Cyclic voltammogram recorded at a scan rate of 0.25 mV s⁻¹ with the redox couple chosen for the determination of the half-wave potential (indicated by the dashed grey line), and b) shifted potential of the AC-QRE in E-NaClO₄.

Table A1. Values obtained from gas sorption analysis of the different carbon samples (corresponding graphs are shown in Figure A2).

Sample	QSDFT surface area / m ² g ⁻¹	BET surface area / m ² g ⁻¹	Total pore vol- ume / cm ³ g ⁻¹	Micropore volume / cm ³ g ⁻¹	Average pore width / nm
C65	54	64	0.12	0.01	9.7
KS6L	21	24	0.05	0.01	10.1
Nanostars	293	395	0.71	0.12	15.3
OLC1300V	286	314	1.06	0.05	12.9
OLC1700A	205	223	0.57	0.04	11.1
SuperP	55	62	0.11	0.01	9.9

Table A2. Values obtained from Raman analysis of the different carbons (corresponding graphs are given in Figure A3).

Sample	D-mode position / cm^{-1}	D-mode FWHM / cm^{-1}	G-mode position / cm^{-1}	G-mode FWHM / cm^{-1}	I_D/I_G ratio
C65	1347±2	128±5	1593±3	80±4	2.3±0.4
KS6L	1353±1	43±2	1581±1	19±1	0.2±0.1
Nanostars	1333±2	58±3	1586±3	58±3	1.4±0.2
OLC1300V	1342±1	152±11	1590±1	80±4	3.1±0.8
OLC1700A	1344±1	60±2	1589±1	60±4	1.2±0.1
SuperP	1352±2	123±5	1603±2	76±4	2.6±0.4

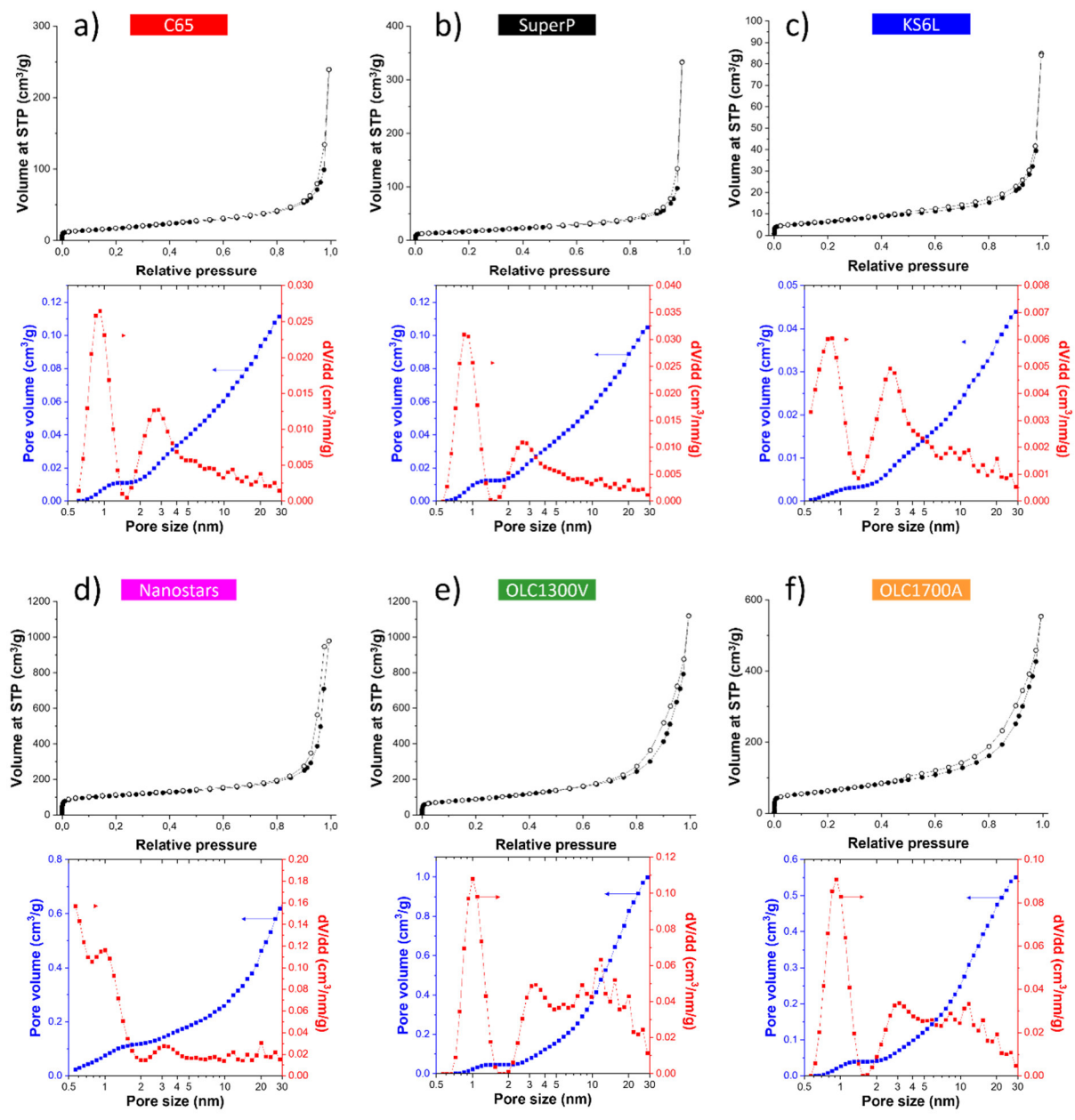


Figure A2. Gas sorption isotherms and pore volume distributions of a) C65, b) SuperP, c) KS6L, d) Nanostars, e) OLC1300V, and f) OLC1700A.

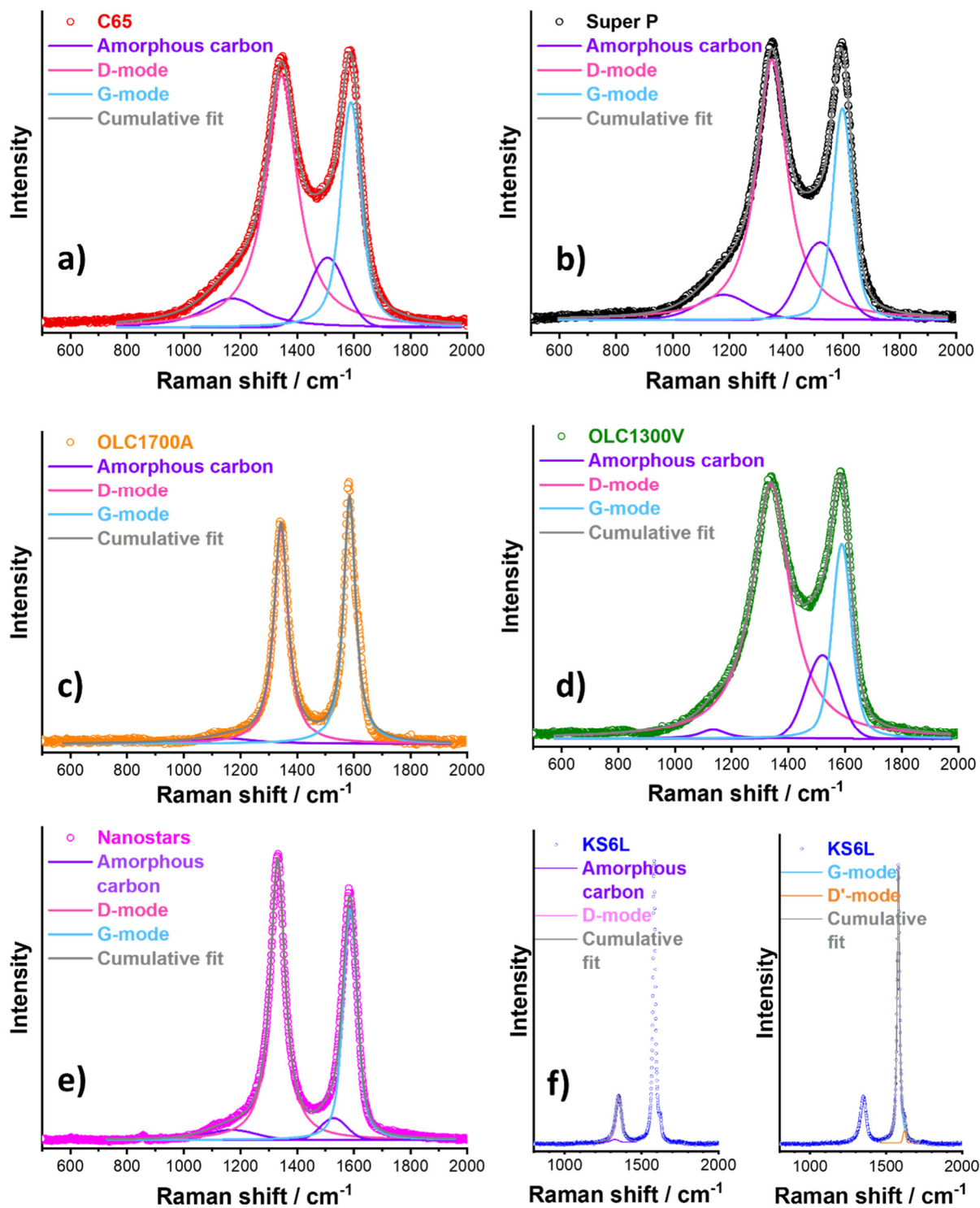


Figure A3. Measured and fitted Raman spectra of a) C65, b) SuperP, c) OLC1700A, d) OLC1300V, e) Nanostars, and f) KS6L.

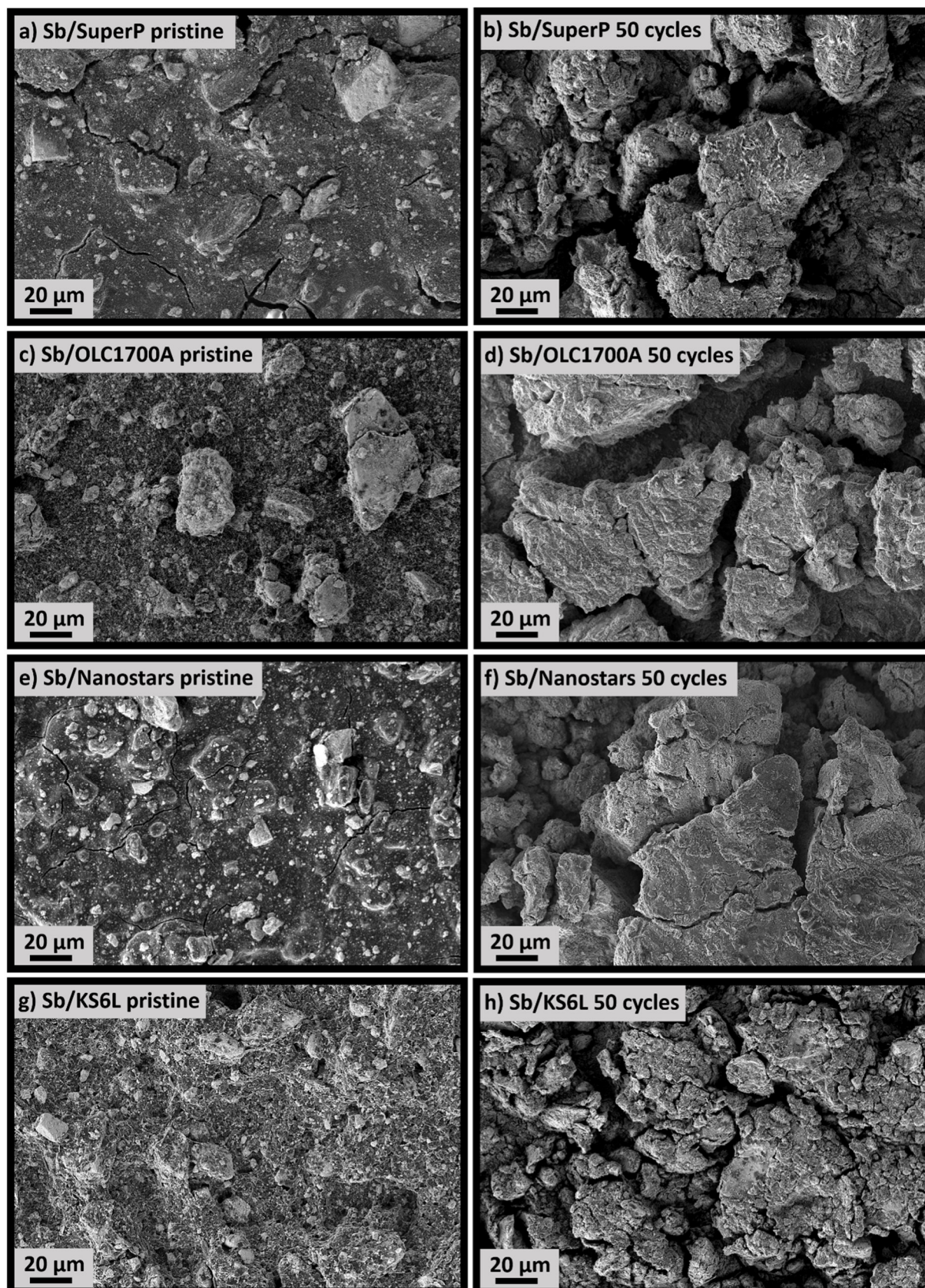


Figure A4. Scanning electron micrographs of a) pristine Sb/SuperP, b) Sb/SuperP after 50 cycles, c) pristine Sb/OLC1700A, d) Sb/OLC1700A after 50 cycles, e) pristine Sb/Nanostars, f) Sb/Nanostars after 50 cycles, g) pristine Sb/KS6L, and h) Sb/KS6L after 50 cycles.

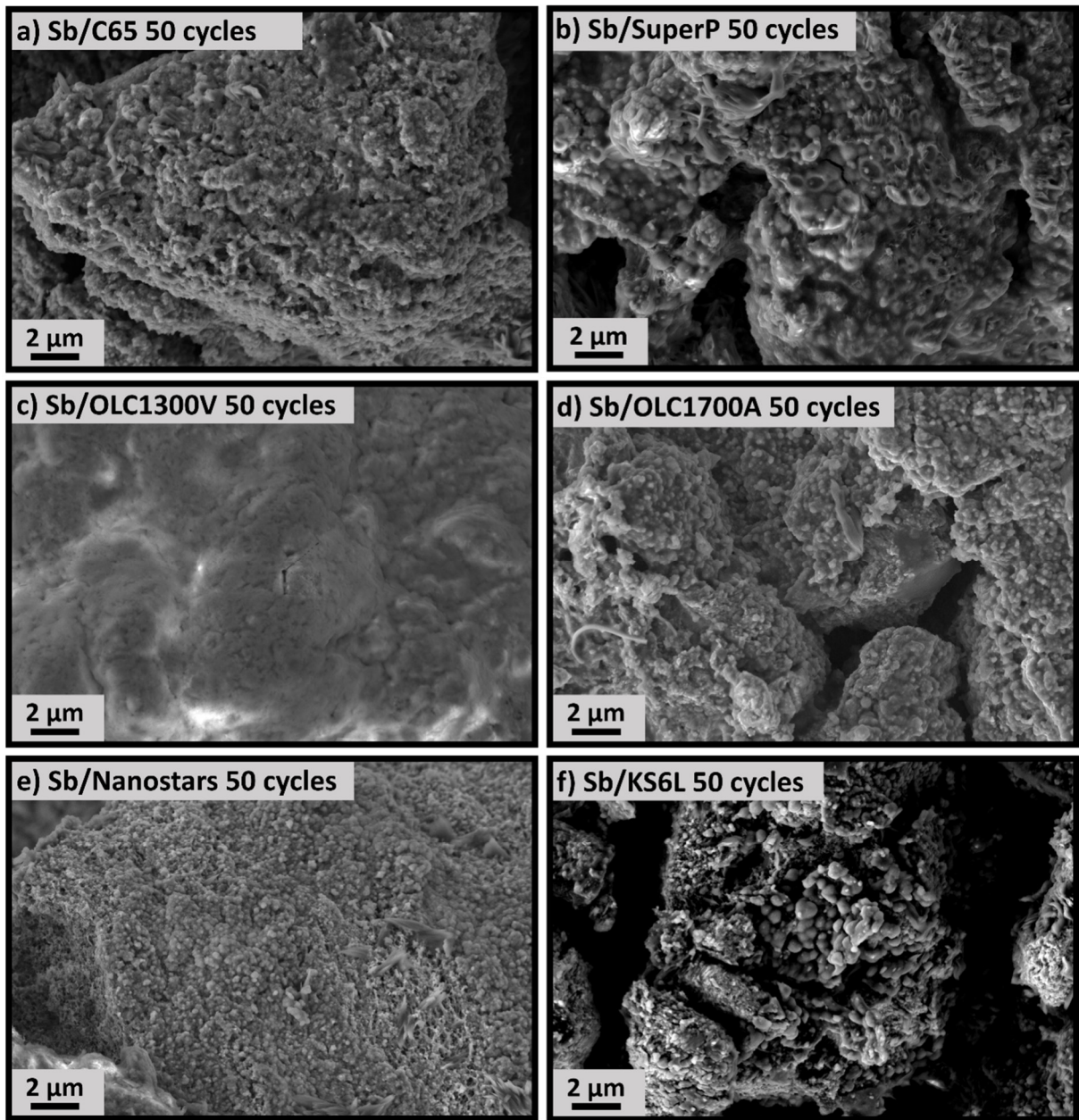


Figure A5. Scanning electron micrographs of a) Sb/C65, b) Sb/SuperP, c) Sb/OLC1300V, d) Sb/OLC1700A, e) Sb/Nanostars, and f) Sb/KS6L after 50 cycles.

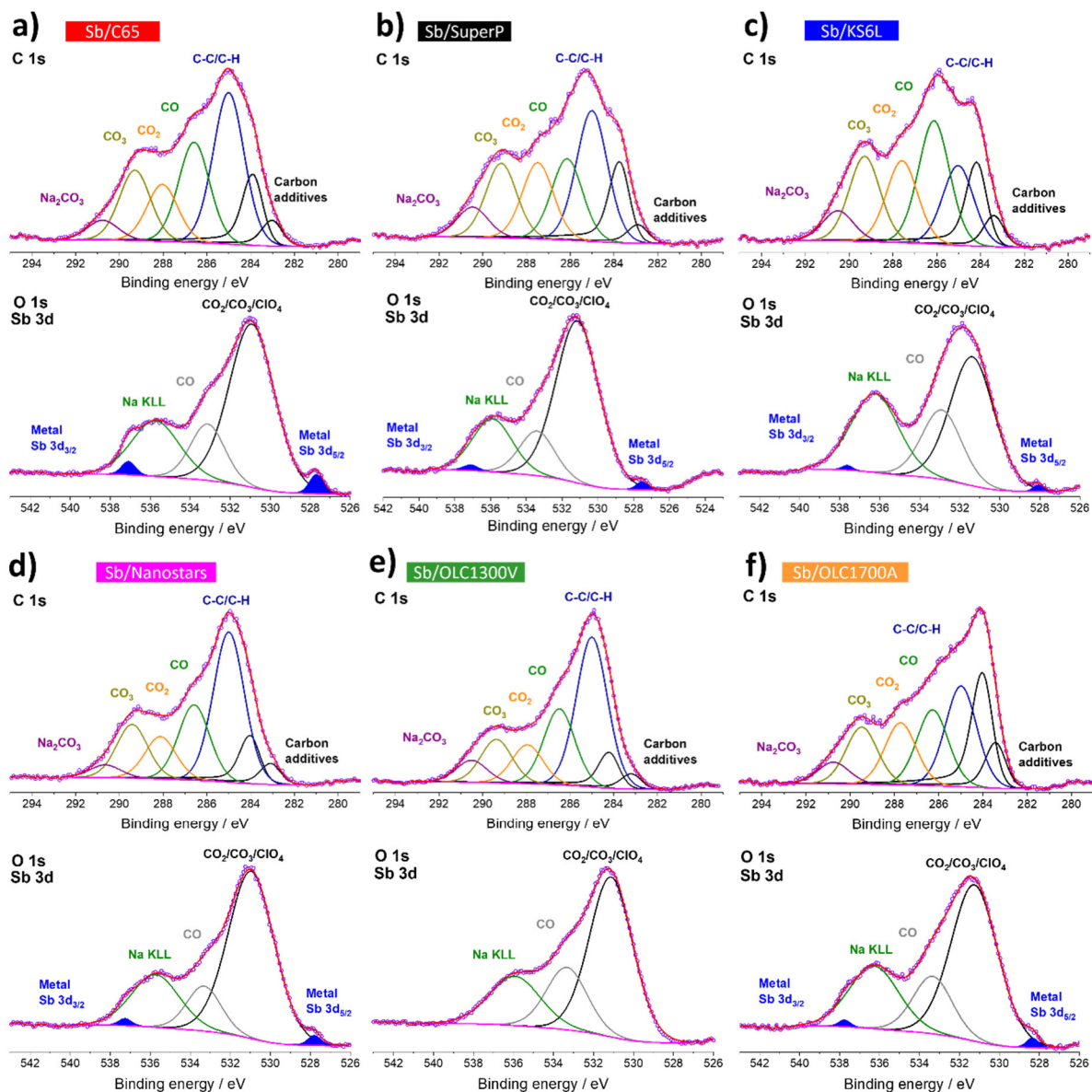


Figure A6. C 1s, O 1s and Sb 3d XPS spectra of a) Sb/C65, b) Sb/SuperP, c) Sb/KS6L, d) Sb/Nanostars, e) Sb/OLC1300V, and f) Sb/OLC1700A after 50 cycles.

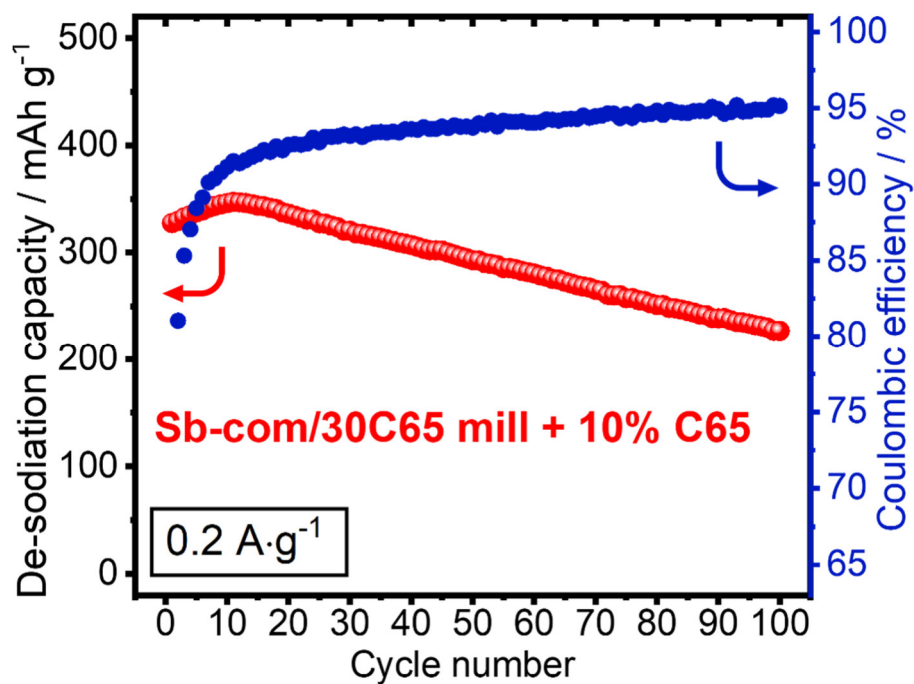


Figure A7. Electrochemical cycling stability at 0.2 A g⁻¹ and corresponding Coulombic efficiency of Sb-com/30C65 mill + 10 % C65.

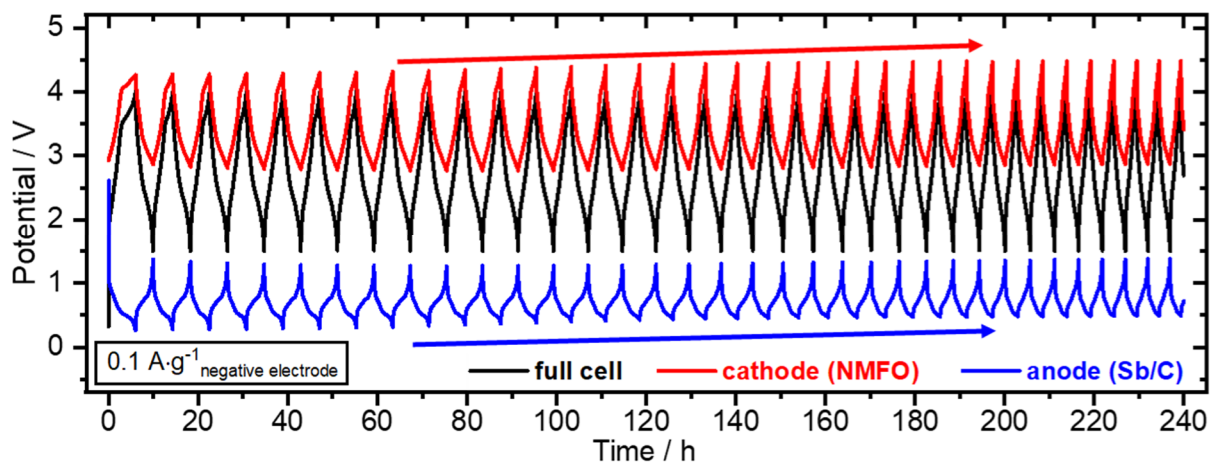


Figure A8. Potential curve of the NMFO//Sb/C full cell and the respective measured profiles of the anode and cathode over time. The arrow indicates the potential-shift of the electrodes.

11 Scientific contributions

11.1 Publications

2020:

1. K. Pfeifer, M. F. Greenstein, D. Aurbach, X. Luo, H. Ehrenberg, S. Dsoke, Interaction between Electrolytes and Sb_2O_3 -Based Electrodes in Sodium Batteries: Uncovering the Detrimental Effects of Diglyme, *ChemElectroChem*, **2020**, 7, 3487 – 3495.
2. K. Pfeifer, S. Arnold, Ö. Budak, X. Luo, V. Presser, H. Ehrenberg, S. Dsoke, Choosing the Right Carbon Additive is of Vital Importance for High-Performance Sb-Based Na-Ion Batteries, *Journal of Materials Chemistry A*, **2020**, 8, 6092 – 6104.
3. C. Li, A. Sarapulova, K. Pfeifer, S. Dsoke, Effect of Continuous Capacity Rising Performed by FeS/Fe₃C/C Composite Electrodes for Lithium-Ion Batteries, *ChemSusChem*, **2020**, 13, 986 – 995.

2019:

1. K. Pfeifer, S. Arnold, J. Becherer, C. Das, J. Maibach, H. Ehrenberg, S. Dsoke, Can Metallic Sodium Electrodes Affect the Electrochemistry of Sodium-Ion Batteries? Reactivity Issues and Perspectives, *ChemSusChem*, **2019**, 12, 3312 – 3319.
2. S. Fleischmann, K. Pfeifer, M. Widmaier, H. Shim, Ö. Budak, V. Presser, Understanding Interlayer Deprotonation of Hydrogen Titanium Oxide for High-Power Electrochemical Energy Storage, *ACS Applied Energy Materials*, **2019**, 2, 3633 – 3641.

2018:

1. M. Widmaier, K. Pfeifer, L. Bommer, V. Presser, Valence-Tuned Lithium Titanate Nanopowder for High - Rate Electrochemical Energy Storage, *Batteries & Supercaps*, **2018**, 1, 11 – 26.

11.2 Conference contributions

1. K. Pfeifer, S. Arnold, J. Becherer, C. Das, J. Maibach, H. Ehrenberg, S. Dsoke, The Detrimental Impact of Sodium Metal Electrodes on Electrochemical Experiments, *International Conference, Durban (South Africa) – International Society of Electrochemistry (ISE)*, **2019**, Poster Presentation.
2. K. Pfeifer, S. Arnold, J. Becherer, C. Das, J. Maibach, H. Ehrenberg, S. Dsoke, Choosing the Right Carbon Additive is of Vital Importance for High-Performance Sb-Based Na-Ion Batteries, *International Online-Conference, Belgrade (Serbia) – International Society of Electrochemistry (ISE)*, **2020**, Poster Presentation.

12 Contributions of co-authors and other researchers

Section 5.1 is extracted from the scientific publication “Can Metallic Sodium Electrodes Affect the Electrochemistry of Sodium - Ion Batteries? Reactivity Issues and Perspectives” .^[56]

The planning, organization and conception of the presented work and all included experiments were done by Kristina Pfeifer and supervised by Helmut Ehrenberg and Sonia Dsoke. Furthermore, Kristina Pfeifer has written the manuscript. Electrode preparation and cell assembly were conducted by Kristina Pfeifer and supported by Stefanie Arnold. Kristina Pfeifer further conducted electrochemical testing and analyzed the obtained data. Optical characterization and ex-situ XRD were also performed and analyzed by Kristina Pfeifer. Julian Becherer carried out optical microscopy measurements and Chittaranjan Das performed XPS measurements and analyzed the data with the support of Julia Maibach. These experiments were planned, coordinated and interpreted by Kristina Pfeifer in discussion with the corresponding operators. All results were discussed with Sonia Dsoke and Helmut Ehrenberg, who helped to finalize the manuscript.

Section 5.3 is extracted from the scientific publication “The Interaction Between Electrolytes and Sb₂O₃-based Electrodes in Sodium Batteries: Uncovering Detrimental Effects of Diglyme”.^[171]

The planning, organization and conception of the presented work and all included experiments were done by Kristina Pfeifer and supervised by Doron Aurbach and Miryam Fayena Greenstein at the Bar-Ilan University in Ramat Gan (Israel) and by Helmut Ehrenberg and Sonia Dsoke at the KIT in Karlsruhe. Furthermore, Kristina Pfeifer has written the manuscript. Electrode preparation and cell assembly were conducted by Kristina Pfeifer as well as the electrochemical testing and analysis of the obtained data. XRD, SEM, Ex-situ SEM and EDS were performed and analyzed by Kristina Pfeifer. Angelina Sarapulova helped to refine the XRD data. Xianlin Luo carried out XPS measurements and analyzed the data. These XPS experiments were planned, coordinated and interpreted by Kristina Pfeifer in discussion with the corresponding operator. ICP-MS analysis was done by Thomas Bergfeldt. All results were discussed with Miryam Fayena Greenstein, Doron Aurbach, Sonia Dsoke and Helmut Ehrenberg, who helped to finalize the manuscript.

Section 6.1 and 6.2 are extracted from the scientific publication “Choosing the right carbon additive is of vital importance for high-performance Sb-based Na-ion batteries”.[59]

The planning, organization and conception of the presented work and all included experiments were done by Kristina Pfeifer and supervised by Volker Presser at the INM in Saarbrücken and by Helmut Ehrenberg and Sonia Dsoke at the KIT in Karlsruhe. Furthermore, Kristina Pfeifer has written the manuscript. The synthesis of Sb, electrode preparation, cell assembly and electrochemical testing were conducted by Kristina Pfeifer and Stefanie Arnold. XRD and SEM of the Sb nanopowder were carried out by Kristina Pfeifer and the XRD data was refined by Helmut Ehrenberg. Ex-situ SEM and EDS were performed and analyzed by Kristina Pfeifer. Xianlin Luo carried out XPS measurements and analyzed the data. These XPS experiments were planned, coordinated and interpreted by Kristina Pfeifer in discussion with the corresponding operator. Raman, GSA, TEM and elemental analysis of the carbons were performed by Öznil Budak. The data analysis was done by Öznil Budak, Kristina Pfeifer and Volker Presser. All results were discussed with Volker Presser, Sonia Dsoke and Helmut Ehrenberg, who helped to finalize the manuscript.

